
Electronic Thesis and Dissertation Repository

4-17-2019 9:30 AM

Development of a Force-Based Ream Vector Measurement System For Glenoid Reaming Simulation

David Axford
The University of Western Ontario

Supervisor
Ferreira, Louis
The University of Western Ontario Co-Supervisor
Johnson, Jim
The University of Western Ontario

Graduate Program in Biomedical Engineering
A thesis submitted in partial fulfillment of the requirements for the degree in Master of Engineering Science
© David Axford 2019

Follow this and additional works at: <https://ir.lib.uwo.ca/etd>



Part of the [Biomedical Devices and Instrumentation Commons](#)

Recommended Citation

Axford, David, "Development of a Force-Based Ream Vector Measurement System For Glenoid Reaming Simulation" (2019). *Electronic Thesis and Dissertation Repository*. 6106.
<https://ir.lib.uwo.ca/etd/6106>

This Dissertation/Thesis is brought to you for free and open access by Scholarship@Western. It has been accepted for inclusion in Electronic Thesis and Dissertation Repository by an authorized administrator of Scholarship@Western. For more information, please contact wlsadmin@uwo.ca.

Abstract

Glenoid reaming is a technically challenging step during total shoulder arthroplasty surgery that may be improved through frequent practice and exposure to simulation training. At our institution, a vibration haptic glenoid reaming simulator is being developed that simulates the vibrations felt during glenoid reaming. This thesis presents the development of a force-based reamer vector measurement system that allows the simulator to measure the user's net applied force and reamer angle of approach. This capability allows for the simulation of eccentric reaming maneuvers commonly used to adjust the glenoid orientation. The system error was characterized and evaluated using a robot to operate a surgical reaming tool. Finally, a study was performed that assessed the ability of surgeons to correct glenoid retroversion while using the haptic vibration simulator. Overall, the surgeons were able to correct glenoid orientation within 1 degree of the target orientation, according to the simulator's reaming vector measurement system.

Keywords

Total Shoulder Arthroplasty, Surgical Simulation, Glenoid Reaming, Glenoid Retroversion Correction, Haptic Vibration Simulation

Co-Authorship

- Chapter 1: David Axford – sole author
- Chapter 2: David Axford – study design, data collection, wrote manuscript
Louis Ferreira – study design, reviewed manuscript
Jim Johnson – reviewed manuscript
- Chapter 3: David Axford – study design, data collection, statistical analyses, wrote manuscript
Louis Ferreira – study design, reviewed manuscript
Jim Johnson – reviewed manuscript
- Chapter 4: David Axford – study design, data collection, wrote manuscript
Louis Ferreira – study design, reviewed manuscript
Jim Johnson – reviewed manuscript
- Chapter 5: David Axford – sole author

Acknowledgments

Firstly, I would like to thank my supervisors, Dr. Louis Ferreira and Dr. Jim Johnson. Dr. Ferreira, I would like to thank you for your guidance and support on this project. Thank you for your mentorship and for the time and energy you have given to help me succeed; your expertise and insight have been invaluable. Dr. Johnson, I would like to thank you as well for mentorship and for all your efforts to see me succeed. Thank you for introducing me to HULC lab and for getting me involved in number of projects that allowed me to collaborate with some amazing people. To both of you, thank you for the incredible opportunities you have given me. You have taught me so much and it has been a pleasure working for you.

I would like to thank Dr. Marie-Eve LeBel for her help with rounding up test subjects and being there to help with the clinical direction of my project. Your input was appreciated, and I am grateful to have been able to work so closely with the clinical staff at the hospital.

To my lab mates in the Bioengineering and Surgical Mechatronics labs, thank you for making my time here so enjoyable. You have been incredible to work with and I wish you all the best in whatever you pursue next. I want to give a special thanks to Mayank Sharma who let me benefit from all his hard work programming the robot. Your help definitely improved my project.

Lastly, I would like to thank my family for their unconditional love and support. Without you I would not be where I am today. I am so thankful to be a part of a tight-knit family and I love you all very much.

Table of Contents

Abstract.....	i
Co-Authorship.....	ii
Acknowledgments	iii
Table of Contents	iv
List of Tables.....	viii
List of Figures	xi
Nomenclature	xvi
Chapter 1 - Introduction	1
1.1 Shoulder Anatomy.....	1
1.2 Glenohumeral Arthritis	3
1.3 Total Shoulder Arthroplasty.....	4
1.4 Glenoid Reaming.....	5
1.5 Surgical Training.....	5
1.6 Surgical Simulation	6
1.7 Simulation in Orthopaedics.....	8
1.7.1 Simbionix ARTHRO Mentor.....	8
1.7.2 Sim-Ortho	9
1.7.3 VirtaMed ArthroS.....	10
1.7.4 TraumaVision.....	11
1.7.5 ArthroVision	12
1.7.6 Precision OS.....	13
1.7.7 Osso VR.....	14
1.8 Glenoid Reaming Simulator.....	15
1.9 Tracking Systems	18

1.9.1	Encoded Linkage	18
1.9.2	Electromagnetic Tracking	19
1.9.3	Optical Tracking	19
1.10	Force Measurement Systems	20
1.11	Rationale	22
1.12	Objectives and Hypotheses	23
1.13	Thesis Overview	24
Chapter 2 - Development of a Force-based Reaming Vector Measurement System		25
2.1	Anatomical and Simulator Coordinate System Definition	25
2.1.1	Defining a Glenoid Coordinate System and Desired Measurands	25
2.1.2	Defining a Glenoid Reaming Simulator Coordinate System	28
2.2	System Design for Force Triangulation	29
2.2.1	System Hardware Design	29
2.2.2	Force Data Acquisition System	30
2.3	Cantilever Load Cell Calibration	32
2.4	Force-based Measurement System Calibration	36
2.4.1	Measurand Calibration	39
2.4.2	Error Compensation	47
2.5	Final Calibration Performance Assessment	61
2.6	Summary	67
Chapter 3 - Reamer Vector Measurement System Error Characterization		68
3.1	Experimental Setup	68
3.1.1	Force Application System	68
3.1.2	Force Recording Systems	70
3.1.3	Reamer Angle of Approach Tracking System	70
3.1.4	Optical Tracking Data Acquisition System	71

3.1.5	Optical Tracking Coordinate Systems	72
3.2	Loading Protocol	75
3.3	Force-Control Loading Repeatability	77
3.4	Reamer Vector Measurement System Accuracy with Force-Control Loading ...	78
3.4.1	Coordinate System Alignment	78
3.4.2	Version Angle of Approach Accuracy	80
3.4.3	Inclination Angle of Approach Accuracy	87
3.4.4	Net Force Magnitude Accuracy	93
3.5	Summary	95
Chapter 4 - Haptic Glenoid Reaming Simulator for Shoulder Arthroplasty: Early Experience with Expert Surgeons		96
4.1	Generating Simulated Computed Tomography DICOM Images for Pre-Operative Templating	96
4.2	Modular Shoulder Model Design	104
4.3	Study Protocol	107
4.4	Results	110
4.4.1	Pre-Operative Templating Results	110
4.4.2	Reaming Performance Results	112
4.5	Summary	118
Chapter 5 - Discussion and Conclusions		120
5.1	Summary	120
5.2	Strengths	123
5.3	Limitations	124
5.4	Future Work	124
References		126
Appendix A: Repeatability of Reamer Vector Measurement System Error Presented in Chapter 2		131

Appendix B: Reamer Vector Measurement System Error Data Averaged Over Five Trials for Results Presented in Chapter 2.....	147
Appendix C: LabVIEW Calibration and Error Compensation VIs	151
Appendix D: Simulated CT Generation MATLAB Code	160
Appendix E: KUKA Light Weight Robot Force-Control Repeatability Data Presented in Chapter 3	164
Appendix F: Custom Load Cell Mount Critical Dimensions	172
Curriculum Vitae.....	173

List of Tables

Table 2.1: Measurement System Sweep Error Summary	45
Table 2.2: Measurand Naming Convention and Calibration Summary	48
Table 2.3: Force Measurement System Error Summary	63
Table 3.1: Force Control Loading Repeatability Intraclass Correlation Coefficients	77
Table 3.2: Version Angle of Approach Overall Error – Reamer Vector Measurement System vs. Certus Optotrak.....	80
Table 3.3: Version Angle of Approach Overall Error – ATI Nano25 Load Cell vs. Certus Optotrak	82
Table 3.4: Version Angle of Approach Overall Error – Reamer Vector Force Measurement System vs. Certus Optotrak minus Load Cell Errors	84
Table 3.5: Inclination Angle of Approach Overall Error – Reamer Vector Measurement System vs. Certus Optotrak.....	87
Table 3.6: Inclination Angle of Approach Overall Error – ATI Nano25 Load Cell vs. Certus Optotrak	89
Table 3.7: Inclination Angle of Approach Overall Error – Reamer Vector Force Measurement System vs. Certus Optotrak with Load Cell Errors Subtracted.....	91
Table 3.8: Net Force Magnitude Overall Error – Reamer Vector Measurement System vs. ATI Nano25 Load Cell	93
Table 4.1: Glenoid Retroversion Measurements from the Generated CT Images	111
Table 4.2: Intended Angle of Retroversion Correction	112
Table 4.3: Ideal Post-Operative Glenoid Orientation.....	112
Table 4.4: Difference Between Intended and Actual Retroversion Correction Angle	113

Table 4.5: Difference Between Intended and Final Glenoid Version Orientation.....	114
Table 4.6: Final Glenoid Inclination Angle Summary	117
Table 4.7: Net Force Magnitude Performance Summary	118
Table A.1: Average Version Angle of Approach Error (°) - Trial 1	132
Table A.2: Average Version Angle of Approach Error (°) - Trial 2	133
Table A.3: Average Version Angle of Approach Error (°) - Trial 3	134
Table A.4: Average Version Angle of Approach Error (°) - Trial 4	135
Table A.5: Average Version Angle of Approach Error (°) - Trial 5	136
Table A.6: Average Inclination Angle of Approach Error (°) - Trial 1.....	137
Table A.7: Average Inclination Angle of Approach Error (°) - Trial 2.....	138
Table A.8: Average Inclination Angle of Approach Error (°) - Trial 3.....	139
Table A.9: Average Inclination Angle of Approach Error (°) - Trial 4.....	140
Table A.10: Average Inclination Angle of Approach Error (°) - Trial 5.....	141
Table A.11: Average Net Force Magnitude Error (N) - Trial 1	142
Table A.12: Average Net Force Magnitude Error (N) - Trial 2.....	143
Table A.13: Average Net Force Magnitude Error (N) - Trial 3.....	144
Table A.14: Net Force Magnitude Error (N) - Trial 4.....	145
Table A.15: Net Force Magnitude Error (N) - Trial 5.....	146
Table B.1: Average Version Angle of Approach Error (°) – All Trials	148
Table B.2: Average Inclination Angle of Approach Error (°) – All Trials.....	149

Table B.3: Average Net Force Magnitude Error (N) – All Trials	150
Table E.1: Version Angle of Approach Measurements from Optotrak Certus for Repeatability Analysis	164
Table E.2: Version Angle of Approach Measurements from the ATI Nano25 Load Cell for Repeatability Analysis	165
Table E.3: Version Angle of Approach Measurements from the Reamer Vector Measurement System for Repeatability Analysis	166
Table E.4: Inclination Angle of Approach Measurements from Optotrak Certus for Repeatability Analysis	167
Table E.5: Inclination Angle of Approach Measurements from the ATI Nano25 Load Cell for Repeatability Analysis	168
Table E.6: Inclination Angle of Approach Measurements from the Reamer Vector Measurement System for Repeatability Analysis	169
Table E.7: Net Force Magnitude Measurements from the ATI Nano25 Load Cell for Repeatability Analysis	170
Table E.8: Net Force Magnitude Measurements from the Reamer Vector Measurement System for Repeatability Analysis	171

List of Figures

Figure 1.1: Glenohumeral Joint Anatomy	1
Figure 1.2: Glenoid Erosion Morphologies (classified by Walch et al.)	3
Figure 1.3: Total Shoulder Arthroplasty Glenoid Component	4
Figure 1.4: Symbionix ARTHRO Mentor	9
Figure 1.5: OSSimTech Sim-Ortho™	10
Figure 1.6: VirtaMed ArthroS.....	11
Figure 1.7: Swemac TraumaVision.....	12
Figure 1.8: Swemac ArthroVision.....	13
Figure 1.9: Precision OS - VR headset and controllers (left), VR simulation (right)	14
Figure 1.10: Glenoid Reaming Simulator [61]	17
Figure 1.11: Touch 3D Systems Serial Linkage Haptic Device	18
Figure 1.12: Strain Gauge Schematic	20
Figure 1.13: Wheatstone Bridge Circuit	21
Figure 2.1: Glenoid-Centered Coordinate System Definition	26
Figure 2.2: Angle of Approach Definition.....	27
Figure 2.3: Simulator Coordinate System Definition.....	28
Figure 2.4: Force-based Measurement System Design and Instrumentation	31
Figure 2.5: Data acquisition system	32
Figure 2.6: Cantilever Load Cell Calibration Setup.....	33

Figure 2.7: Cantilever A Calibration Curve.....	34
Figure 2.8: Cantilever B Calibration Curve	35
Figure 2.9: Cantilever C Calibration Curve	36
Figure 2.10: Commercial Load Cell Setup for Force-based Measurement System Calibration	37
Figure 2.11: KUKA 7 Axes Light Weight Robot and Reamer Mount.....	38
Figure 2.12: Calibration Curve for Version Angle Calculation	40
Figure 2.13: Calibration Curve for Inclination Angle Calculation	42
Figure 2.14: Sample Reamer Angle of Approach Output from Force-based Measurement System Calibration	47
Figure 2.15: Version Angle Error Compensation Stage 1 Calibration Curve	49
Figure 2.16: Version Angle Error Compensation Stage 2 Surface Fit	50
Figure 2.17: Version Angle Error Compensation Stage 3 Calibration Curve	52
Figure 2.18: Inclination Angle Error Compensation Stage 1 Calibration Curve	53
Figure 2.19: Inclination Angle Error Compensation Stage 2 Surface Fit.....	55
Figure 2.20: Force on ML Axis Error Compensation Stage 1 Calibration Curve	56
Figure 2.21: Force on ML Axis Error Compensation Stage 2 Calibration Curve	57
Figure 2.22: Force on ML Axis Error Compensation Stage 2 Calibration Curve	58
Figure 2.23: Net Force Error Compensation Stage 2 Calibration Curve.....	60
Figure 2.24: Net Force Error Compensation Stage 3 Calibration Curve.....	61
Figure 2.25: Version Angle Error After Calibration and Error Prediction.....	64

Figure 2.26: Inclination Angle Error After Calibration and Error Prediction	65
Figure 2.27: Net Force Error After Calibration and Error Prediction	66
Figure 3.1: Reamer Tool-Tip Coordinate System.....	69
Figure 3.2: Optical Tracker Placement.....	71
Figure 3.3: Optical Tracking Data Acquisition Setup	72
Figure 3.4: Robot and Load Cell Alignment.....	73
Figure 3.5: Digitization for Optical Tracker Coordinate System Construction	74
Figure 3.6: Reamer Angle of Approach Defined by a Polar Coordinate System	76
Figure 3.7: Certus Optotrak and ATI Nano25 Load Cell Coordinate System Alignment	79
Figure 3.8: Version Angle of Approach Surface Plots – Reamer Vector Measurement System vs. Certus Optotrak.....	81
Figure 3.9: Version Angle of Approach Surface Plots – ATI Nano25 Load Cell vs. Certus Optotrak	83
Figure 3.10: Version Angle of Approach Surface Plots – Reamer Vector Force Measurement System vs. Certus Optotrak minus Load Cell Errors	86
Figure 3.11: Inclination Angle of Approach Surface Plots – Reamer Vector Measurement System vs. Certus Optotrak.....	88
Figure 3.12: Inclination Angle of Approach Surface Plots – ATI Nano25 Load Cell vs. Certus Optotrak	90
Figure 3.13: Inclination Angle of Approach Surface Plots – Reamer Vector Force Measurement System vs. Certus Optotrak with Load Cell Errors Subtracted.....	92
Figure 3.14: Net Force Magnitude Surface Plots – Reamer Vector Force Measurement System vs. ATI Nano25 Load Cell.....	94

Figure 4.1: CT Scapula Segmentation and 3D Model Generation	97
Figure 4.2: Sectioning the Glenoid From the 3D Scapula Model	98
Figure 4.3: Glenoid Version Alteration	99
Figure 4.4: Altered Scapular Mask Overlaid onto CT Slices	100
Figure 4.5: DICOM Native Scapula Removal	101
Figure 4.6: DICOM Soft Tissue Fill.....	102
Figure 4.7: DICOM Trabecular Bone Segmentation	103
Figure 4.8: Final Altered DICOM Image	104
Figure 4.9: Shoulder Model Scapular Component	105
Figure 4.10: Shoulder Model Glenoid Component	106
Figure 4.11: Shoulder Model 3D Printed Component Assembly	106
Figure 4.12: Reaming Simulator 3D Printed Glenoid and Soft Shoulder Model	107
Figure 4.13: Familiarization Stage Graphical Indicator	108
Figure 4.14: Glenoid Reaming Assessment Stage Graphical Indicator	110
Figure C.1: Data Acquisition Block Diagram.....	151
Figure C.2: Calibration and Error Compensation Block Diagram.....	152
Figure C.3: Cantilever A Calibration Block Diagram.....	153
Figure C.4: Cantilever B Calibration Block Diagram	153
Figure C.5: Cantilever C Calibration Block Diagram	153
Figure C.6: Version Load Ratio Block Diagram.....	154

Figure C.7: Version Angle Calibration Block Diagram	154
Figure C.8: Version Angle Error Compensation Stage 1 Block Diagram.....	154
Figure C.9: Version Angle Error Compensation Stage 2 Block Diagram.....	155
Figure C.10: Version Angle Error Compensation Stage 3 Block Diagram.....	155
Figure C.11: Inclination Load Ratio Block Diagram	156
Figure C.12: Inclination Angle Calibration Block Diagram.....	156
Figure C.13: Inclination Angle Error Compensation Stage 1 Block Diagram	156
Figure C.14: Inclination Angle Error Compensation Stage 2 Block Diagram	157
Figure C.15: F_{ML} Calibration Block Diagram.....	157
Figure C.16: F_{ML} Error Compensation Stage 1 Block Diagram	158
Figure C.17: F_{ML} Error Compensation Stage 2 Block Diagram	158
Figure C.18: F_{ML} Error Compensation Stage 3 Block Diagram	158
Figure C.19: F_{net} Error Compensation Stage 1 Block Diagram	159
Figure C.20: F_{net} Error Compensation Stage 2 Block Diagram	159
Figure C.21: F_{net} Error Compensation Stage 3 Block Diagram	159
Figure F.1: Custom Load Cell Mount Critical Dimensions.....	172

Nomenclature

Nomenclature is listed in order of appearance

TSA	Total Shoulder Arthroplasty
VR	Virtual Reality
GRS	Glenoid Reaming Simulator
EM	Electromagnetic
DOF	Degree-of-freedom
GC	Glenoid Center
AI	Inferior Scapular Angle Point
TS	Trigonum Spinae
SI	Superior – Inferior
AP	Anterior – Posterior
ML	Medial – Lateral
VLR	Version Cantilever Load Ratio
ILR	Inclination Cantilever Load Ratio
F_{net}	Net Force Magnitude
F_{SI}, F_{AP}, F_{ML}	Force magnitude acting along the SI, AP, and ML axes, respectively
$incAngle, verAngle$	Inclination angle and version angle, respectively

$F_{cantA}, F_{cantB}, F_{cantC}$	Force acting on cantilever A, B and C, respectively
VerC, VerC1, VerC2, VerC3	Calibrated version angle and calibrated version angle with 1, 2 and 3 stages of error compensation, respectively
IncC, IncC1, IncC2	Calibrated inclination angle and calibrated inclination angle with 1 and 2 stages of error compensation, respectively
$F_{MLC}, F_{MLC1}, F_{MLC2}, F_{MLC3}$	Calibrated force, F_{ML} , and calibrated force, F_{ML} , with 1, 2 and 3 stages of error compensation, respectively
$F_{netC}, F_{netC1}, F_{netC2}, F_{netC3}$	Calibrated force, F_{net} , and calibrated force, F_{net} , with 1, 2 and 3 stages of error compensation, respectively
ICC	Intraclass Correlation Coefficient
$X_{ream}, Y_{ream}, Z_{ream}$	Tool-tip coordinate system axes
γ	Net angle between the neutral axis and the reamer shaft
θ	Angle between the positive AP axis and the reamer shaft on a sagittal plane
CT	Computed Tomography
STL	Stereolithography

Chapter 1

1 Introduction

Overview: This chapter discusses relevant background information and the motivation for this research. Relevant anatomy is discussed and surgical training and simulation are introduced. Current orthopaedic simulator technologies are reviewed and the current state of development of a surgical simulator from our institution is presented. The rationale and the specific objectives for this research are also described.

1.1 Shoulder Anatomy

The glenohumeral joint is a ball-and-socket joint commonly referred to as the shoulder (Figure 1.1). The shoulder is formed by the articulation between the proximal head of the humerus and the shallow cavity of the scapula called the glenoid fossa [1]. For this research, the focus will be on the glenoid fossa of the scapula.

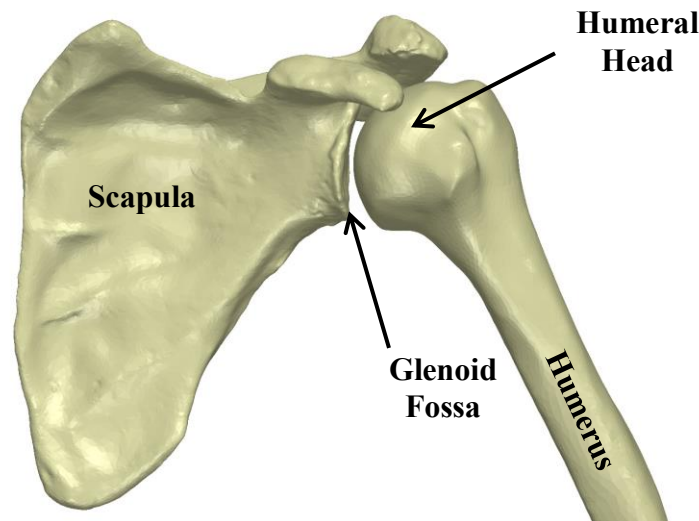


Figure 1.1: Glenohumeral Joint Anatomy

The major components of the glenohumeral joint are shown and include the proximal head of the humerus and the glenoid fossa of the scapula.

The glenoid fossa, commonly called the glenoid, is a shallow cup-like structure that allows for large relative motion between the humerus and the scapula giving the shoulder the largest range of motion of any joint in the human body. The glenoid articular surface is composed of cartilage and covers a layer of dense cortical bone called subchondral bone. Beyond the subchondral bone is cancellous bone, also known as trabecular bone.

Since the glenoid structure allows for a large range of motion, numerous muscular and ligamentous structures are required to maintain joint stability [2]–[4]. However, the shoulder is susceptible to instability, injury and pathology that may require surgical intervention [5], [6].

1.2 Glenohumeral Arthritis

Osteoarthritis is characterized by the loss of cartilage in synovial joints and is associated with bone osteophyte formation, hardening of the subchondral bone and thickening of the joint capsule [7]. The prevalence of osteoarthritis increases with age [7] and is the most common cause of disability among adults [8]. It has been estimated to affect 27 million adults in the United States in 2005 [9]. When arthritis occurs in the shoulder it can cause significant pain and, in some cases, results in posterior erosion of the glenoid and posterior subluxation of the humeral head as illustrated in Figure 1.2 [10]. In the occurrence of severe glenohumeral osteoarthritis, surgical intervention may be required to reduce pain and improve patient quality of life.

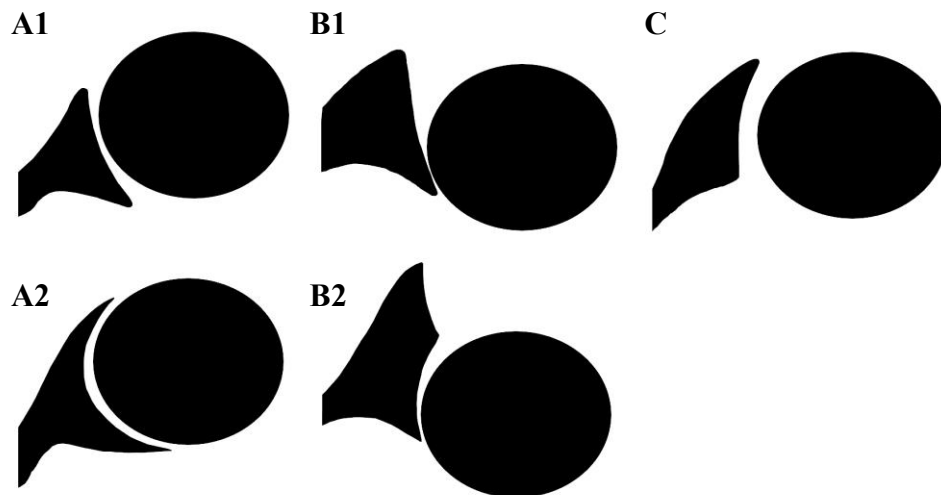


Figure 1.2: Glenoid Erosion Morphologies (classified by Walch et al.)

Walch et al. classified glenoid erosion morphology. Type A is characterized by even wear of the glenoid and type B is classified by posterior subluxation of the humeral head that can result in posterior wear of the glenoid (B2). Type C is characterized by glenoid retroversion of more than 25 degrees

1.3 Total Shoulder Arthroplasty

Total shoulder arthroplasty (TSA) is a commonly performed procedure that is increasing in prevalence for the treatment of severe glenohumeral osteoarthritis [11]–[13]. TSA involves replacing the proximal head of the humerus with a metal ball-and-stem implant and resurfacing the glenoid with a polyethylene implant [14] (Figure 1.3). Overall, TSA has shown to have a 90 percent success rate [15] with complications occurring in 10-15 percent of cases [16]–[18]. Of these complications, the largest contributor is loosening of the glenoid component which accounts for 32-38 percent of complications and occurs in 4-5 percent of all TSA cases [16], [17], [19]. When glenoid component loosening occurs, a revision surgery is often required to reduce patient pain and discomfort. The process of preparing the glenoid to receive the polyethylene implant is the focus of this research.

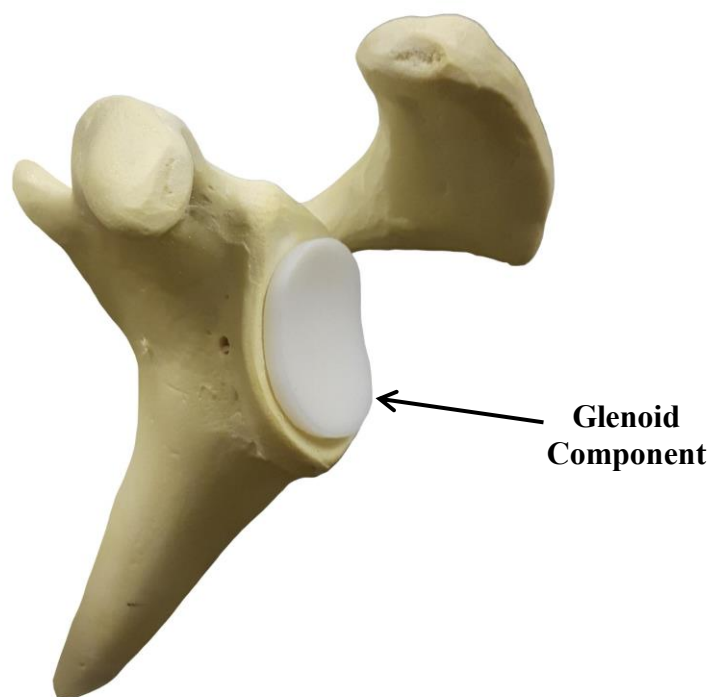


Figure 1.3: Total Shoulder Arthroplasty Glenoid Component

In total shoulder arthroplasty, the glenoid is resurfaced with a polyethylene prosthesis.

1.4 Glenoid Reaming

To prepare the glenoid surface for the implant, a surgeon often uses a surface reamer to remove the cartilage layer and expose the subchondral bone. This procedure is technically challenging and is critical to the success of the implant [20], [21]. When a patient has even wear of the glenoid, the surgeon will likely ream perpendicular to the glenoid to prepare the surface; this is called concentric reaming. However, if there is posterior wear of the glenoid, the surgeon may ream at a non-perpendicular angle to correct glenoid retroversion; this is called eccentric reaming. By reaming eccentrically, the surgeon can remove bone material from the anterior edge of the glenoid and correct the glenoid orientation [22]. If glenoid retroversion is not corrected then the glenoid component is more susceptible to loosening [19], [23], [24]; however, studies have also shown that high degrees of version correction should be avoided to ensure that there is sufficient bone stock to achieve proper implant fixation [25], [26]. This battle to preserve bone stock but correct glenoid orientation is a large motivation for the use of augmented implants [27], but these implants often require more sophisticated tooling to prepare the glenoid surface. There are many factors that a surgeon must consider when performing glenoid reaming to achieve proper implant fixation which makes this procedure technically challenging. Importantly, technical surgical tasks such as glenoid reaming can be difficult for trainees to learn [28].

1.5 Surgical Training

Historically, surgical training programs have operated with the mantra, “see one, do one, teach one” [29]. This training structure is a time and volume-based training program where surgical residents work many hours and are exposed to many procedures. However, the introduction of resident duty hour limits and an emphasis on patient safety [30] has begun to shift training programs from emphasizing time and volume-based training to competency-based training [29]. Although the duty hour restrictions are an attempt to prevent medical errors due to sleep deprivation and improve resident quality of life [31], some believe that the reduced hours will negatively impact clinical exposure for residents [30]. This is a legitimate concern knowing that the development of complex psychomotor skills in surgery requires frequent exposure and practice [32]. Studies have

shown that technical errors in surgery can cause patient disability and even death [33]–[36], and some of these errors have been linked to the inexperience of trainees [37]. With the reduction in resident work hours and a focus on patient care, more structured training programs with surgical assessments that objectively track resident proficiency are needed [38].

1.6 Surgical Simulation

A simulator is a device that recreates an aspect of a real-world system and allows the user to interact with that system [39]. Simulation is a tool that has been implemented in training program curriculums in industries such as aviation [40]. In the field of medicine, surgical simulators recreate surgical situations for trainees to practice specific skills related to surgery [41]. This method of training is advantageous because it can provide objective measures of trainee performance [38] while distancing the trainee from the patient until the necessary skills are acquired [33]. Simulation has shown to be a successful training modality in surgery as skills developed through simulation have been shown to translate to the operating room [42]–[44].

There are two main classes of simulators; low- and high- fidelity systems. Low-fidelity simulators allow for the practice of a single skill such as knot tying while high-fidelity simulators replicate an entire operative procedure.[41] Within each of these classes there are several types of simulators; live animals, cadavers, bench-top and laparoscopic box simulators, virtual-reality (VR) simulators, augmented reality (AR) simulators, and robot assisted laparoscopic surgery (RAS) simulators [41], [45].

Animal Models

Animal models are high-fidelity simulators and share many of the features of human surgery. They allow residents to work as a team and practice communication skills during a procedure which trains residents on skills beyond the required technical and motor skills. Animal models have also been shown to improve technical skills of trainees [46]. However, because of the anatomical differences between animals and humans and the associated ethical concerns, this method of simulation is not always preferred.

Cadaver Models

Cadaver models are considered the gold standard in surgical simulation for some disciplines [47] because they allow trainees to train with high-fidelity simulation with accurate representation of anatomy. Although cadaver models use dead tissue, in some instances the cadaveric tissues can be perfused with blood adding to the realism of the simulation [47]. The drawbacks to cadaver models include high cost and limited availability.

Bench-top Simulators

Bench-top simulators are commonly used for training in laparoscopic surgery and the skills acquired through this simulation method have shown to be correlated with performance in the operating room [45]. These trainers are commonly low-fidelity and simulate simple tasks like cutting, suturing and transferring of objects [48]. However, high-fidelity bench-top simulators exist that incorporate synthetic and animal tissues [41]. The downsides to these simulators are that they are expensive and there is a limit to the degree of realism possible when using synthetic materials.

VR Simulator

VR simulators allow trainees to manipulate and interact with a virtual surgical environment. Some of the advantages of VR simulation are the high accuracy of anatomical details, simulator reusability and simulator versatility. Unlike cadaver models or live animal models, the simulator can be used to repeat a procedure multiple times until a trainee is comfortable with the procedure. Secondly, a single simulator can be used to simulate several surgical procedures. VR simulators are able to provide objective measures to score the proficiency of trainees [49] and can provide feedback to the trainee which may remove the need for supervision [41]. The downsides of VR simulation are the high cost, lack of high-fidelity haptic feedback, and limited realism when compared to live animal and cadaver models.

AR Simulator

AR simulators are similar to VR simulation however they combine the virtual environment with the physical environment by using real physical materials, instruments and feedback to produce higher fidelity haptic feedback [50]. Like VR simulation, AR simulation is limited by its high cost.

RAS Simulation

RAS simulation is a relatively new development that incorporates VR simulation into training on a surgical robot such as the da Vinci system. There are multiple simulators that are used for the da Vinci system and are generally low-fidelity systems that train basic motor and hand-eye coordination skills [41]. These systems are still in their infancy and require further validation studies. A major drawback to these systems is the highly specialized application and high cost.

1.7 Simulation in Orthopaedics

1.7.1 Simbionix ARTHRO Mentor

Simbionix ARTHRO Mentor (3D Systems, Littleton, USA) was the first available arthroscopy training simulator (Figure 1.4). It is a virtual reality simulator for training orthopaedic residents on knee, hip and shoulder arthroscopic diagnostic procedures. It is equipped with anatomical models, surgical instruments and a haptic device to apply resistance to user motion according to user input. The simulator can simulate a variety of procedures and provide performance metrics for training assessment. The onboard screen shows the virtual environment where the procedure is being performed. The system has been validated for its effectiveness as a training tool [51], [52].



Figure 1.4: Simbionix ARTHRO Mentor¹

Simbionix ARTHRO Mentor (3D Systems, Littleton, USA) virtual reality arthroscopy training simulator.

1.7.2 Sim-Ortho

OSSimTech Sim-OrthoTM (OSSimTech, Montreal, Canada) is a virtual reality simulator that provides a complete training curriculum for a number of knee, spine and trauma open surgery procedures (Figure 1.5). Among the available procedures is partial and total knee replacement with hip arthroplasty planned to be added in 2019. The system is equipped with a haptic device for force feedback and a 3D anatomy viewer [53].

¹ Modified from Simbionix ARTHRO Mentor [Internet]. 3D Systems., Littleton, USA; cited [March 14, 2019]. Available from <https://www.3dsystems.com/medical-simulators/simbionix-arthro-mentor>



Figure 1.5: OSSimTech Sim-Ortho™²

OSSimTech Sim-Ortho™ (OSSimTech, Montreal, Canada) virtual reality simulator for training on a number of knee, spine and trauma open surgery procedures.

1.7.3 VirtaMed ArthroS

VirtaMed ArthroS™ (VirtaMed, Zurich, Switzerland) is a virtual reality arthroscopy surgical simulator (Figure 1.6). With this simulator, trainees use original operating room instruments equipped with magnetic sensors to interact with the system's anatomical models. There is no active force feedback provided by the simulator, but passive feedback is provided as the surgical tool interacts with the tissue model. Various training modules can be accessed with the simulator. This system has been validated for its effectiveness as a training tool [54].

² Modified from Medical EXPO [Internet]. cited [March 14, 2019]. Available from <http://www.medicaexpo.com/prod/ossimtech/product-119826-829001.html>

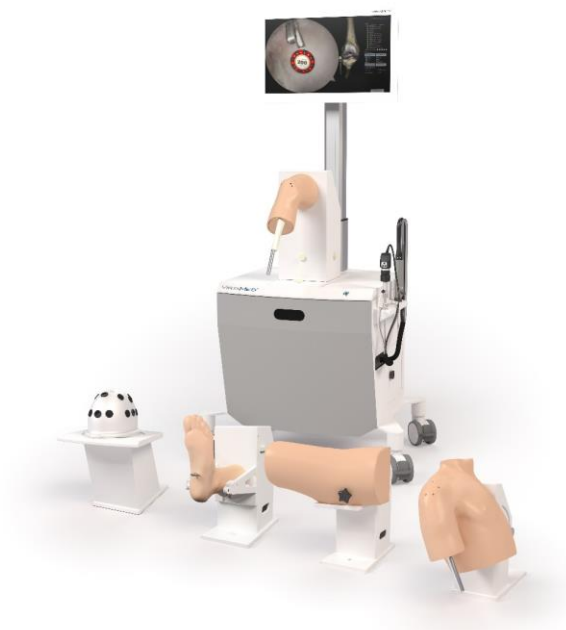


Figure 1.6: VirtaMed ArthroS³

VirtaMed ArthroSTM (VirtaMed, Zurich, Switzerland) virtual reality arthroscopy surgical simulator.

1.7.4 TraumaVision

TraumaVision (Swemac, Linköping, Sweden) is a virtual reality simulator designed to simulate orthopedic trauma surgeries such as hip fracture repair (Figure 1.7). The system includes two screens that show simulated views of the patient and fluoroscopy imaging. Haptic feedback is provided through the simulators instruments as the trainee interacts with different tissues and drills through different bone layers. TraumaVision is equipped with training modules and provides performance metrics so that trainees can learn based on their performance scores [55], [56].

³ Modified from OSET 2018, Las Vegas [Internet]. VirtaMed AG., Zurich, Switzerland. cited [March 14, 2019]. Available from <https://w3.virtamed.com/oset2018>



Figure 1.7: Swemac TraumaVision⁴

TraumaVision (Swemac, Linköping, Sweden) virtual reality orthopedic trauma simulator.

1.7.5 ArthroVision

ArthroVision (Swemac, Linköping, Sweden) is a virtual reality box-trainer simulator designed to teach basic arthroscopy skills (Figure 1.8). Unlike some lower fidelity box-trainer simulators, the ArthroVision includes haptics and force feedback to make the training experience more realistic; however, the virtual environment does not simulate anatomical structures but only simulates an empty box. The simulator has training modules for simple tasks like tracking a moving object and steady camera motion [57].

⁴ Modified from TraumaVision [Internet]. Swemac Innovation AB, Linköping, Sweden. cited [March 14, 2019]. Available from <http://www.swemac.com/simulators/traumavision>



Figure 1.8: Swemac ArthroVision⁵

ArthroVision (Swemac, Linköping, Sweden) virtual reality arthroscopy skills box-trainer simulator.

1.7.6 Precision OS

Precision OS (Precision OS Technology, Vancouver, Canada) is a fully immersive VR simulation trainer and pre-operative planner (Figure 1.9). The user wears a VR headset with two handheld controllers to visualize and manipulate the surgical environment. The system can generate some haptic feedback but due to the controller design, no force feedback is generated. The system is equipped with educational modules to improve surgical skill of novice surgeons. Precision OS can also be used as a pre-operative planning tool where surgeons can upload a peri-articular fracture and develop a pre-operative plan. The trainee/surgeon is then able to perform the surgery virtually before

⁵ Modified from ArthroVision [Internet]. Swemac Innovation AB, Linköping, Sweden. cited [March 14, 2019]. Available from <http://www.swemac.com/simulators/arthrovision>

performing the procedure in the operating room [58]. In December of 2018, Precision OS released a training module that will instruct trainees how to implant an augmented glenoid baseplate for reverse shoulder arthroplasty [59].



Figure 1.9: Precision OS - VR headset and controllers (left)⁶, VR simulation (right)⁷

Precision OS immersive VR simulation trainer and pre-operative planner. The simulator uses a headset and two handheld controllers (left). The simulator replicates an immersive surgical environment (right).

1.7.7 Osso VR

Similar to the Precision OS system, Osso VR (Osso VR, Palo Alto, USA) is a fully immersive VR system that creates a virtual operating room that the user visualizes using a VR head set and interacts with using two handheld controllers. The system provides haptic feedback through the two controllers and actively measures performance metrics to assess the trainee's proficiency. A unique feature that this system incorporates is the ability to train a team of surgeons in one virtual environment from any location. This allows for surgeons to practice team communication in an operating room setting [60].

⁶ Modified from VRfocus [Internet]. cited [March 14, 2019]. Available from <https://www.vrfocus.com/2018/11/precision-os-secures-2-3-million-investment-for-vr-orthopedic-surgical-education/>

⁷ Modified from VRroom [Internet]. cited [March 14, 2019]. Available from <https://vrroom.buzz/vr-news/tech/precision-os-makes-surgical-vr-training-thing>

1.8 Glenoid Reaming Simulator

At St. Joseph's Hospital in London, Canada, the first glenoid reaming simulator (GRS) is being developed. The first stage of development is described by Kusins et al.[61]. Kusins et al. determined that as a surgeon removes bone with a surgical reamer, the vibration felt through the reamer is correlated with the bone layer being removed (ie. cartilage, subchondral and cancellous bone) [61]. This vibration information is believed to be a valuable tool for training novice surgeons how to perform glenoid reaming. Therefore, the GRS simulates glenoid reaming by reproducing the vibrations that a surgeon would feel during reaming. The simulator measures the force applied by the trainee over time and uses this information to calculate a "virtual depth" of ream. Knowing the depth of ream, the simulator can determine what bone layer the user is reaming and provide vibrational feedback according to that bone layer.

The GRS is composed of three main components, the force measurement system, the vibration transduction system and the user interface (shown in Figure 1.10). The force measurement system consists of a uniaxial load cell mounted to the support wall of the simulator and the simulator housing is mounted onto the load cell. Inside of the simulator housing is the vibration transduction system. This system consists of a haptic vibration transducer (Model TST329, Clark Synthesis Inc.,Colorado, USA) encased in foam mounted to a metal rod. The foam surrounding the transducer is used to dampen the acoustic vibrations produced by the transducer and simulate the passive motion of the scapula that occurs when a surgeon applies a force to the glenoid during reaming. The metal rod fixed to the vibration transducer is fastened on the opposite end to a metal base plate. The simulator user interface consists of a truncated 3D printed scapula model from a patient CT image mounted to the base plate of the simulator. To interact with the system, the user is provided with a fully functional pneumatic surgical reamer that is fitted with a non-fluted 3D printed reaming tip so that the reamer does not remove any material when engaged with the 3D printed scapula. The load cell is oriented so that its measurement axis is normal to the face of the 3D printed glenoid mounted to the simulator. This enables the simulator to measure force normal to the glenoid face and

simulate concentric reaming cases; however, the simulator cannot measure off-axis forces and therefore cannot simulate off-axis or eccentric reaming.

When a user reams on the glenoid surrogate, the simulator measures the force applied by the user and determines what vibration profile to play. This profile is sent to the vibration transducer that causes the scapula to vibrate. The vibrations translate through the reamer shaft and into the hands of the user. This vibration feedback is used as the main source of feedback to train novice surgeons to perform glenoid reaming.

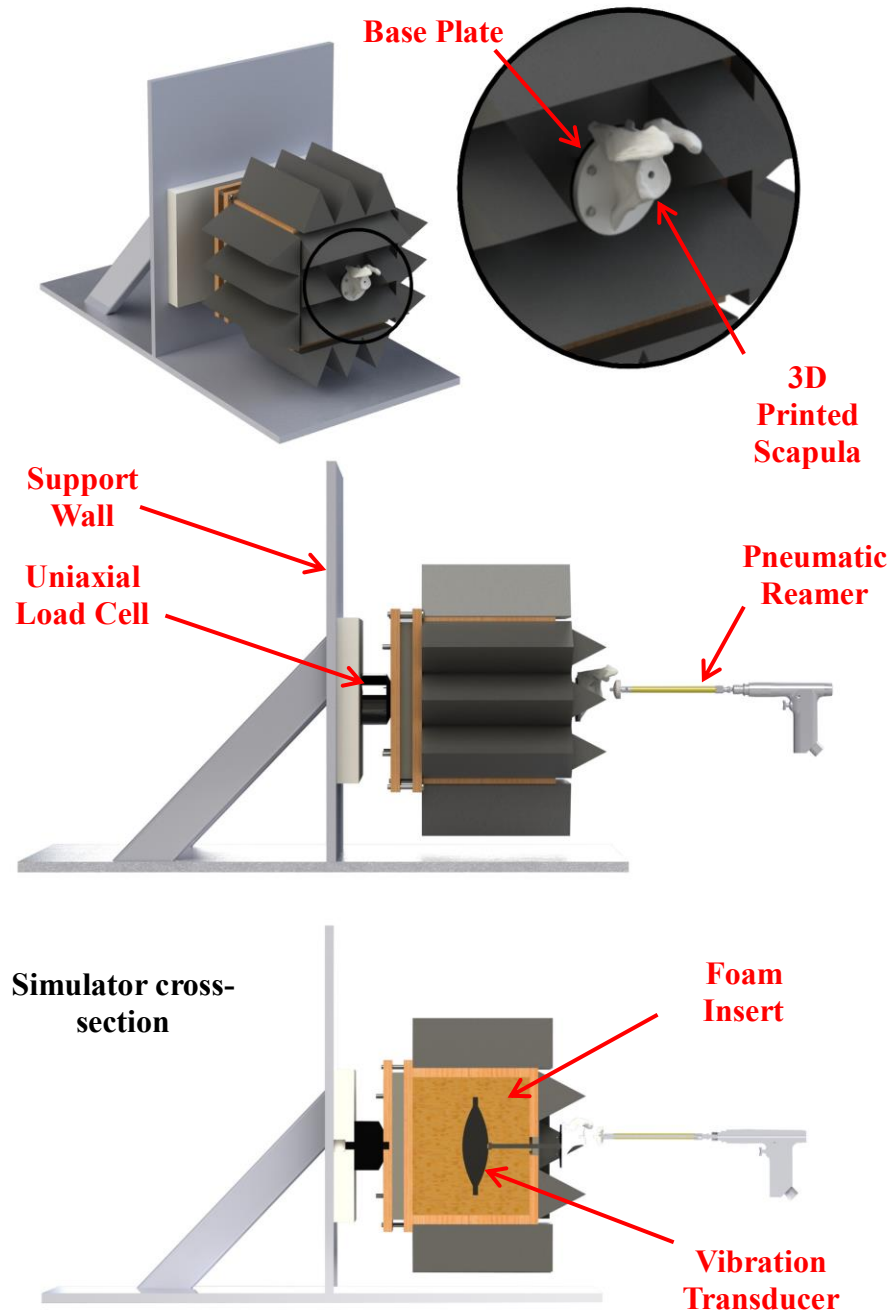


Figure 1.10: Glenoid Reaming Simulator [61]

The glenoid reaming simulator was equipped with a 3D printed shoulder model (top) and a uniaxial load cell (middle). The user reams on the shoulder model using a fully functional surgical reamer (middle) and a vibration transducer reproduces reaming vibrations (bottom).

1.9 Tracking Systems

1.9.1 Encoded Linkage

In many existing simulators, including the ARTHO Mentor, Sim-Ortho TraumaVision and ArthroVision, a serial linkage device is used to measure the orientation of the user instruments (similar to what is shown in Figure 1.11). Each joint of the linkage system contains an encoder that measures the joint angle. From the measured joint angles, the system can calculate the position and orientation of the surgical instrument. These linkages can allow the user to interact with instruments that resemble surgical tools, but they have limited maneuverability because they are attached to the simulator. The linkage systems can also function as force feedback tools by providing resistance to motion of the tool.



Figure 1.11: Touch 3D Systems Serial Linkage Haptic Device⁸

Serial linkage device has encoded joints that measure the position and orientation of the instrument.

⁸ Modified from Touch [Internet]. 3D Systems., Rock Hill, USA. cited [March 15, 2019]. Available from <https://www.3dsystems.com/haptics-devices/touch>

1.9.2 Electromagnetic Tracking

Another method of tracking that is used with some simulators such as VirtaMed ArthroS is electromagnetic (EM) tracking. EM tracking consists of an electromagnetic transmitter that emits an electromagnetic field and sensors that are free to move within the generated field. The magnetic field induces a current in a wire coil inside of the sensors that cues the tracking system to know the position and orientation of the sensor within the magnetic field. In the case of surgical simulation, the transmitter would likely be attached to the simulator platform and a sensor would be placed on the surgical tool to track its position and orientation with respect to the simulator platform. When using these systems, care needs to be taken with the materials that are placed within the electromagnetic field since ferritic materials can interfere with the field and introduce errors [62] as can other equipment used within the simulator that emit an electromagnetic field [63]. Electromagnetic tracking systems allow for unrestricted motion of the surgical tool but cannot serve as a method of haptic feedback like a serial linkage arm. To generate haptic feedback additional systems are required. Fully immersive VR systems like Precision OS and OssoVR often use a combination of electromagnetic tracking, accelerometers and gyroscopes.

1.9.3 Optical Tracking

Optical tracking systems are less common in surgical simulation applications but are very prevalent in surgical settings [64]. An optical tracking system consists of an optical camera and trackers. The system can use either active or passive trackers and may utilize multiple cameras. Optical tracking systems often have higher accuracy than electromagnetic systems and they not susceptible to magnetic interference, but since these systems use cameras, there must always be a line-of-sight between the camera and the trackers [64]. For this reason, implementation of optical systems can be difficult when a line-of-sight is difficult to establish. Similar to electromagnetic tracking systems, optical devices are not capable of generating haptic feedback so additional systems are required when active haptic feedback is desired. Some commercial optical tracking systems include Stryker NAV3i, Northern Digital Inc. Polaris and Optotrak Certus, and Medtronic StealthStation system.

1.10 Force Measurement Systems

Forces cannot be seen or touched and therefore cannot be measured directly. Force is measured by measuring a physical response to the presence of a force. The most common way of measuring force is by measuring deflection or strain. When a force acts on an object, the object changes shape in response to the force, this change in shape is called strain. In one dimension, strain is the ratio of the change in length of a body to the initial length of the body. When considering a volume, strain (volumetric strain) is the ratio of the change in volume of a body to the original volume of the body.

Strain Gauges

To measure strain, a thin-film electrical resistive device called a strain gauge is often used. This device operates under the principle that a change in length of a conductive wire will cause a change in resistance. This is demonstrated by equation (1.1) where R is the resistance, ρ is the resistivity of the material, l is the length of the material, and A is the cross-sectional area of the material.

$$R = \frac{\rho l}{A} \quad (1.1)$$

The gauge structure consists of two leads connected by a long wire arranged in a grid pattern. This grid pattern makes the gauge sensitive to strain in a single direction while being insensitive to strain in the perpendicular directions.



Figure 1.12: Strain Gauge Schematic

A strain gauge is composed of a grid pattern and lead tabs. The grid pattern causes the strain gauge to be sensitive to strain in a single direction.

A common circuit used to measure strain is a Wheatstone bridge circuit. This circuit is a voltage divider circuit containing four branches with a resistor on each branch (shown in Figure 1.13). Depending on the application, a quarter, half or full Wheatstone bridge circuit can be made by replacing one, two or four of the resistors in the bridge with strain gauges, respectively. Different bridge configurations and strain gauge orientations are used to isolate for different strain types (such as bending strain or axial strain). Once a system has been designed and is measuring strain, the Wheatstone bridge circuit can be calibrated to convert the measured strain into force applied.

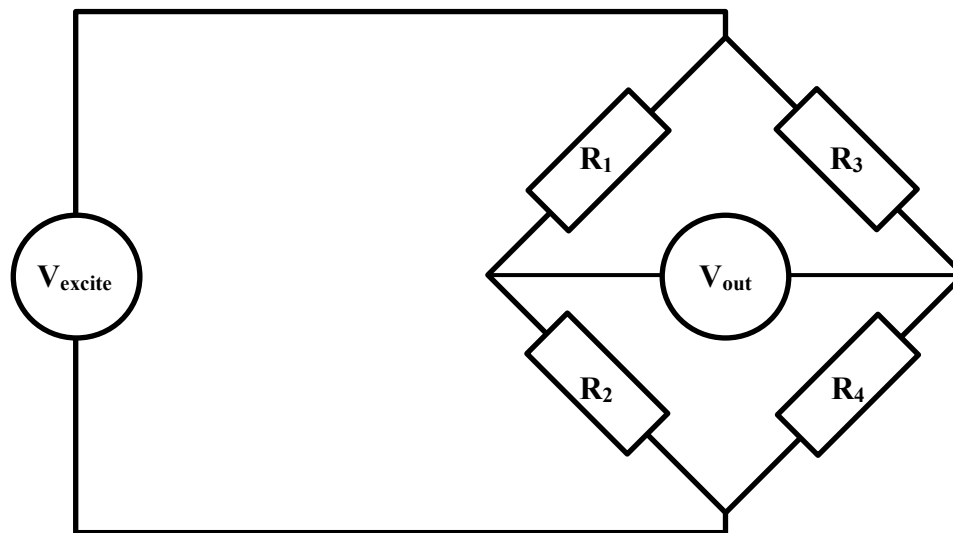


Figure 1.13: Wheatstone Bridge Circuit

A Wheatstone bridge is a voltage divider circuit with four branches; each containing a resistive device. A strain gauge can be insert into one, two or four branches of the bridge.

Load Cells

Load cells are calibrated commercial devices that use internal strain gauges to measure loads and torques. These devices come in a variety of form factors with varying measurement ranges and measurement resolutions. A load cell is designed with a certain number of degree-of-freedom (DOF) that defines the number of independent load and moment measurements. A single DOF load cell measures the forces along a single axis

whereas, multi-axis load cells such as a six degree-of-freedom (6DOF) load cell can measure forces along 3 perpendicular axes and the moments about each of these three axes.

1.11 Rationale

Glenoid reaming is a complex psychomotor skill and is a crucial part of a total shoulder replacement procedure contributing significantly to the performance and longevity of the prosthesis. Complex skills, like reaming, are difficult for novice surgeons to learn and with the introduction of resident work hour restrictions, the acquisition of these skills will become more difficult using historical training methods. Surgical simulation has been introduced as a training modality that can assist trainees in developing required surgical skills by providing objective progress measures while distancing the trainee from patients until they are considered proficient.

As described above, in orthopaedic surgery, there have been several simulators developed that train surgeons on basic laparoscopic techniques, bone fracture fixation and lower extremity arthroplasty. Most recently, an immersive virtual reality simulator has introduced a training module that instructs trainees on the installation of an augmented base plate for reverse total shoulder arthroplasty; however, other than the simulator being developed at our institution no simulator exists that uses tactile vibrations to simulate glenoid reaming for total shoulder arthroplasty.

Previous development of the glenoid reaming simulator at our institution utilized a uniaxial load cell to measure the forces applied perpendicular to the glenoid surface. This enabled the simulator to simulate concentric reaming but prevented it from simulating off-axis or eccentric reaming maneuvers. To simulate eccentric reaming, the simulator must be able to measure the user applied net force vector magnitude and orientation as well as the reamer's angle of approach. Therefore, a reamer vector measurement system capable of measuring the reamer's angle of approach and net force vector is required.

The developed reamer vector measurement system should continue to allow the user to use a fully functional reamer with full maneuverability of the instrument and should not

be hindered by line-of-sight issues or be susceptible to electromagnetic interference. This thesis will discuss the development of a reamer vector measurement system that can be easily incorporated into the simulator set-up. This system will not rely on optical or electromagnetic tracking but will use forces to measure the reamer's angle of approach and the net force vector magnitude applied by the user. With the addition of a reamer vector measurement system, the glenoid reaming simulator's capabilities will be expanded and allow for eccentric reaming simulation in the future.

1.12 Objectives and Hypotheses

The aim of this work is to develop a single measurement system that uses forces to measure both the reamer angle of approach and net force magnitude and integrate this system with the current glenoid reaming simulator.

Objective 1: To design and calibrate a reamer vector measurement system capable of measuring reamer angle of approach and net force magnitude.

Studies have shown that the typical “just” noticeable difference for forces applied during various movements is 5-10 percent of the force being applied [65] and that the ability to differentiate between force magnitudes decreases in the presence of low frequency haptic noise [66]. It has been shown that typical reaming forces lie between 50 N and 100 N [61] so a force measurement accuracy of 1 N is sufficient for a glenoid reaming application. A study has reported that arm angle proprioception error ranges from 0.5 to 2.5 degrees [67] and given that glenoid retroversion measurements are typically reported to the nearest degree [68], a reamer angle of approach accuracy of 0.5 degrees is sufficient.

Hypothesis 1: The reamer angle of approach absolute error will be less than 0.5 degrees and the force magnitude absolute error will be less than 1 Newton.

Objective 2: To use the reamer vector measurement system to assess surgeon's ability to correct glenoid version according to a pre-operative plan. Moreover, to compare these results to expected surgeon performance from the literature, in order to validate the simulator.

A previous glenoid retroversion correction study has reported that of all the cases presented, 100 percent of the cases with pre-operative retroversion of under 10 degrees were corrected within 10 degrees of the ideal orientation and 67% of cases were corrected within 5 degrees of the ideal orientation [68].

Hypothesis 2: The average difference between a surgeon's ideal post-operative glenoid orientation and the actual post-operative orientation will be less than 5 degrees and the average difference will increase as the initial glenoid retroversion angle increases.

1.13 Thesis Overview

Chapter 2 describes the development of the reamer vector measurement system. This includes the system design, calibration and error reduction. The overall error of the system at different force targets is reported.

Chapter 3 describes the system error characterization protocol and results. This includes a description about the systems and testing protocol used to characterize the reamer vector measurement system error. The error for reamer angle of approach and net force magnitude measurements are reported as a function of reamer angle of approach.

Chapter 4 presents a study conducted using the reamer vector measurement system to assess surgeon's ability to correct glenoid retroversion according to a pre-operative plan. The chapter describes a simulated CT generation method for repeatable measures and the overall study protocol. The difference between surgeon's pre-operative targets and the actual reamed correction are reported and discussed.

Chapter 5 gives the conclusions from this research and proposes future work.

Chapter 2

2 Development of a Force-based Reaming Vector Measurement System

Overview: This chapter outlines the design and calibration of a force-based reamer vector measurement system to be used with a glenoid reaming surgical simulator. The scope of the chapter includes the definition of relevant coordinate systems and desired measurands, system design and instrumentation, and calibration. General performance of the measurement system is also presented.

2.1 Anatomical and Simulator Coordinate System Definition

2.1.1 Defining a Glenoid Coordinate System and Desired Measurands

A clinically relevant coordinate system was defined to determine the required measurands for the force-based measurement system. The constructed coordinate system is a glenoid centered system formed from three anatomical land marks; the glenoid center (GC), the inferior scapular angle point (AI) and the trigonum spinae (TS) as shown in Figure 2.1A. Collectively, these three points defined the scapular plane and an axis through GC and TS defined the neutral inclination axis. The glenoid coordinate system is depicted in Figure 2.1B showing an origin at the glenoid center and three orthogonal axes. The coordinate system axes were defined by the scapular plane and the neutral inclination axis. The SI axis was oriented parallel to the scapular plane and normal to the neutral inclination axis in the superior – inferior direction. The AP axis was oriented normal to the scapular plane in the anterior – posterior direction and the ML axis was oriented collinear with the neutral inclination axis in the medial-lateral direction.

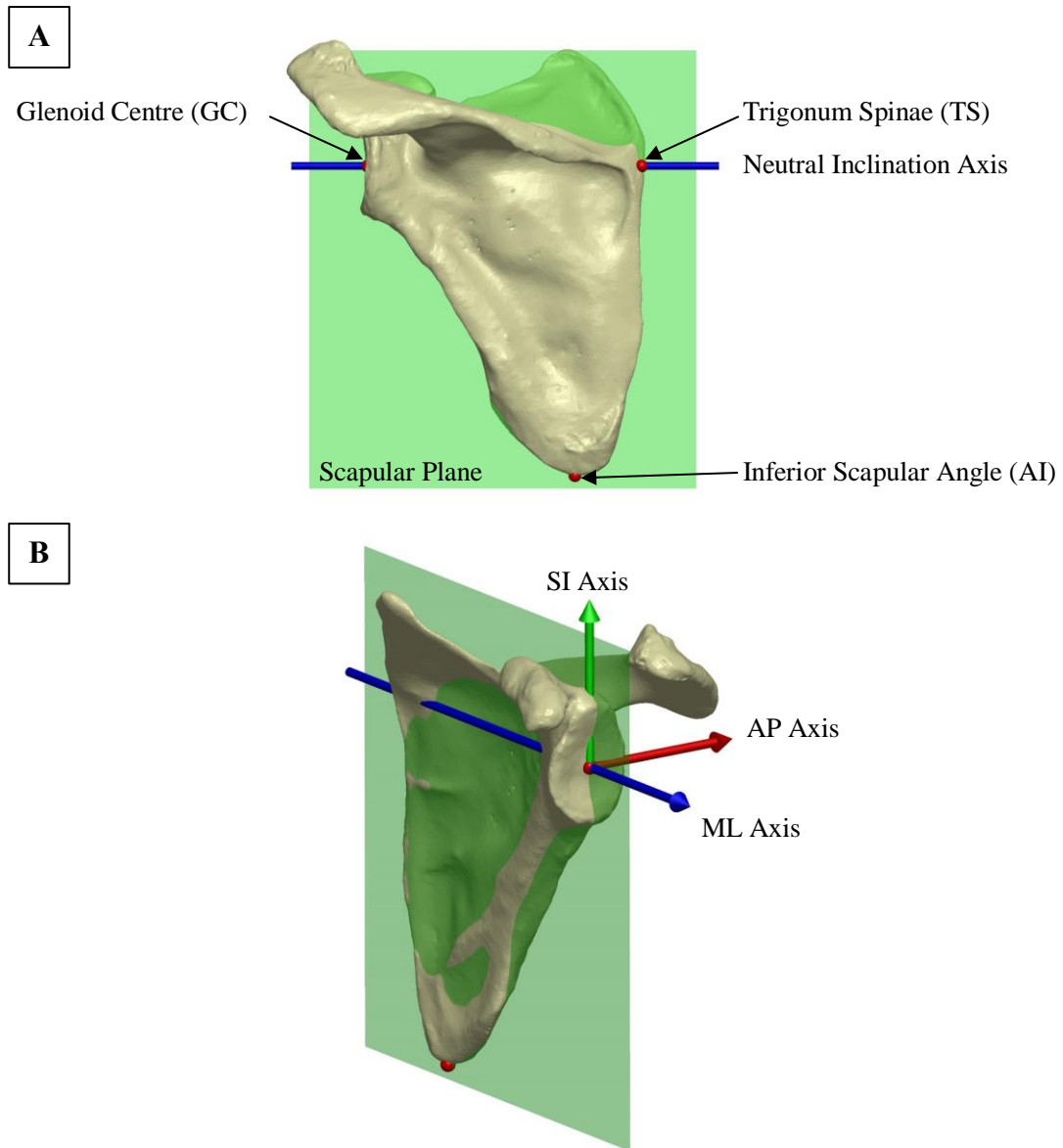


Figure 2.1: Glenoid-Centered Coordinate System Definition

An anatomical coordinate system was defined to determine clinically relevant measurands [A] The glenoid center (GS), trigonum spinae (TS), and inferior scapular angle (AI) were used to define the scapular plane, neutral inclination axis and the glenoid-centered coordinate system. [B] Coordinate system origin is located at the glenoid center and the three orthogonal axes (positive directions) were defined relative to the scapular plane and neutral inclination axis.

To expand the simulator's capabilities and incorporate off-axis reaming, the simulator was calibrated to measure the user's applied net force and the reamer's angle of approach. To measure the reamer's angle of approach in three-dimensional space, the angle was separated into two angles on orthogonal planes; inclination angle of approach and version angle of approach as shown in Figure 2.2. Version angle was defined as the angle between the reamer shaft and the ML axis in transverse plane. Inclination angle was defined as the angle between the reamer shaft and the ML axis in the coronal plane.

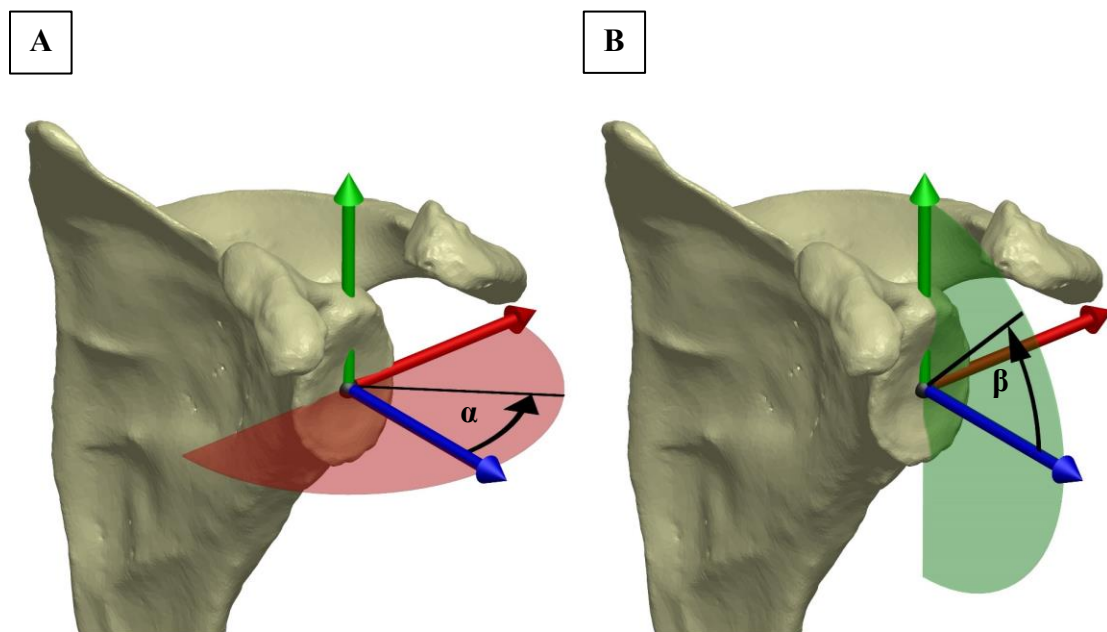


Figure 2.2: Angle of Approach Definition

The reamer angle of approach was divided into two orthogonal angles. [A] Version angle (α) is the angle of approach contained within the transverse plane. Positive direction is from the positive ML axis towards the positive AP axis. [B] Inclination angle (β) is the angle contained in coronal plane. Positive direction is from the positive ML axis to towards the positive SI axis.

2.1.2 Defining a Glenoid Reaming Simulator Coordinate System

A simulator coordinate system was defined to measure the reamer angle of approach and net force magnitude relative to the simulator construct. The simulator coordinate system orientation was defined by three orthogonal axes (SI axis, AP axis and ML axis) as depicted in Figure 2.3. The SI axis was oriented in the vertical direction parallel to the base plate. The AP axis was oriented in the horizontal direction parallel to the base plate and the ML axis was oriented normal to the base plate. The coordinate system origin was located so that the ML axis passed through the center of the base plate but was offset from the base plate along the ML axis by 71.2mm. This offset corresponds with the distance between the base plate and glenoid center of the shoulder model that was used with the simulator. The simulator coordinate system was fixed to the base plate.

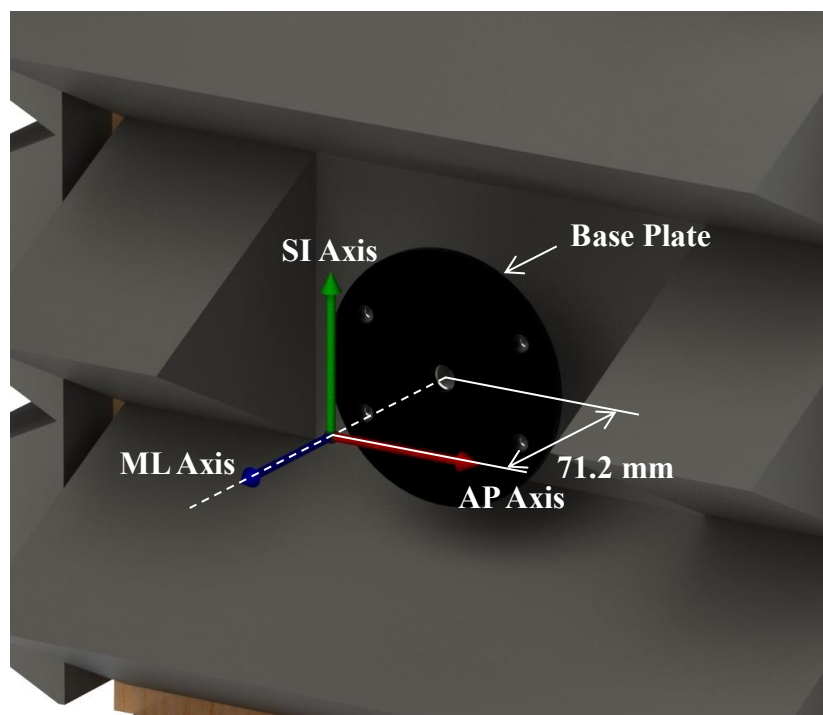


Figure 2.3: Simulator Coordinate System Definition

The anatomical coordinate system was defined within the context of the reaming simulator hardware. This coordinate system was used as the frame of reference for the force-based reamer vector measurement system calibration.

2.2 System Design for Force Triangulation

2.2.1 System Hardware Design

Multiple designs were considered for the reamer vector measurement system; however, a few design constraints limited possible design solutions. The first constraint was that the developed system needed to continue to allow the user to interact with the simulator using a fully functional surgical reamer. This constraint prevented modifications from being made to the reamer. Secondly, the added system could not alter the vibrations felt by the user during simulation. This constraint prevented the developed reamer vector measurement system from being placed between the vibration transducer and the 3D printed scapula mounted to the front of the simulator since this could alter the transmission of vibrations to the user. Additionally, it was advantageous to place the reamer vector measurement system outside of the vibration environment to reduce signal noise caused by vibrations. Given these constraints, the force measurement system was placed between the simulator housing and the support wall similar to the previous uniaxial force measurement system (shown in Figure 2.4D).

To measure the desired measurands defined in section 2.1.1, multiple solutions composed of a combination of multi-axis and single-axis load cells were considered. The simplest potential system consisted of a single multi-axis load cell. However, due to the high anticipated torsions, commercially available multi-axis load cells with the required measurement range and resolution are expensive. Additionally, since the load applied by the user to the simulator would not be applied at the origin of the multi-axis load cell, calibration algorithms would need to be included to transform the forces to the simulator coordinate system defined in section 2.1.2. The need for additional calibration algorithms minimized the advantage of having a commercially calibrated device. Due to cost and the minimized benefit of a commercial system, multiple single-axis load cells were chosen over a single multi-axis load cell. To further reduce costs, single-axis cantilever load cells were fabricated from stock materials and instrumented with strain gauges instead of purchasing commercial load cells. The design of the cantilever load cells used has been previously described [70]. To measure reamer angle of approach and net force applied using single-axis load cells, a minimum of three single-axis load cells were required.

The developed force-based measurement system consisted of three aluminum cantilever load cells mounted to the wall support of the simulator in a tripod configuration as shown in Figure 2.4A. These three cantilevers replaced the uniaxial load cell previously used with the simulator. The simulator housing was mounted to the cantilevers using rubber standoffs so that the simulator housing was a cantilevered system only supported by the three cantilever load cells (shown in Figure 2.4C and Figure 2.4D). With this design, any external load applied to the simulator caused a change in the reaction forces at each cantilever and with the addition of rubber standoffs the vibrations produced by the simulator were dampened so that there would be less vibration induced noise in the force measurements. To measure the change in reaction force, a full Wheatstone bridge strain gauge circuit (configuration type II) using two ‘T’ rosette strain gauges (MICRO-MEASUREMENTS MMF315026) was instrumented onto each cantilever (shown in Figure 2.4B). This bridge configuration allowed for isolated measurement of surface bending strain resulting from a normal force applied perpendicular to the rubber standoff while compensating for temperature and poison effects.

2.2.2 Force Data Acquisition System

All strain measured by the strain gauge circuits was supplied to a C series strain/bridge input module (NI 9237, National instruments Corporation, Austin, Texas). The input module was connected to the simulator computer through a USB chassis (NI USB-9162, National instruments Corporation, Austin, Texas) shown in Figure 2.5. All Data was collected using NI LabVIEW software.

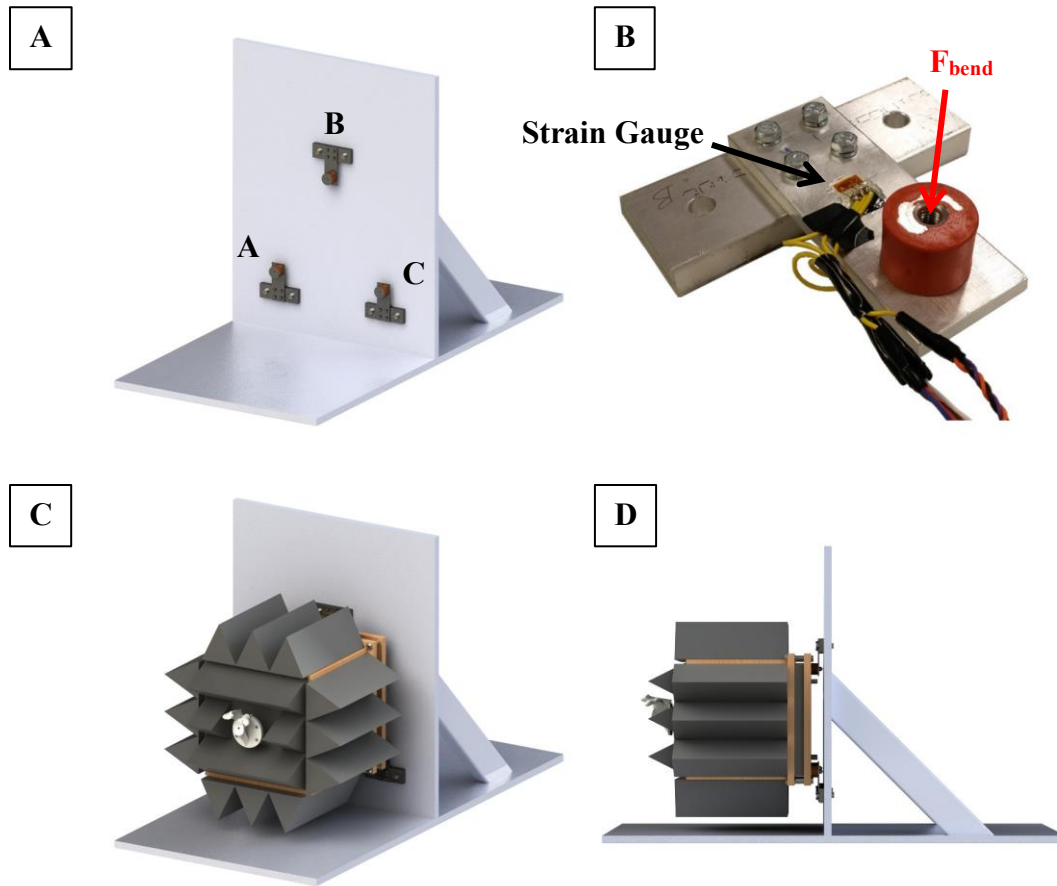


Figure 2.4: Force-based Measurement System Design and Instrumentation

[A] Three aluminum cantilever load cells (A, B & C) were oriented in a tripod configuration mounted to the simulator support wall. [B] Each cantilever was instrumented with a full Wheatstone Bridge strain gauge circuit. A bending force, F_{bend} , acts normal to the cantilever top face and caused bending strain that was measured by the strain gauges. An additional 'T' rosette strain gauge was mounted to the underside of the cantilever (not depicted in figure) [C] The simulator housing was mounted onto the cantilevers. [D] The simulator housing and cantilever load cells were a cantilevered system.

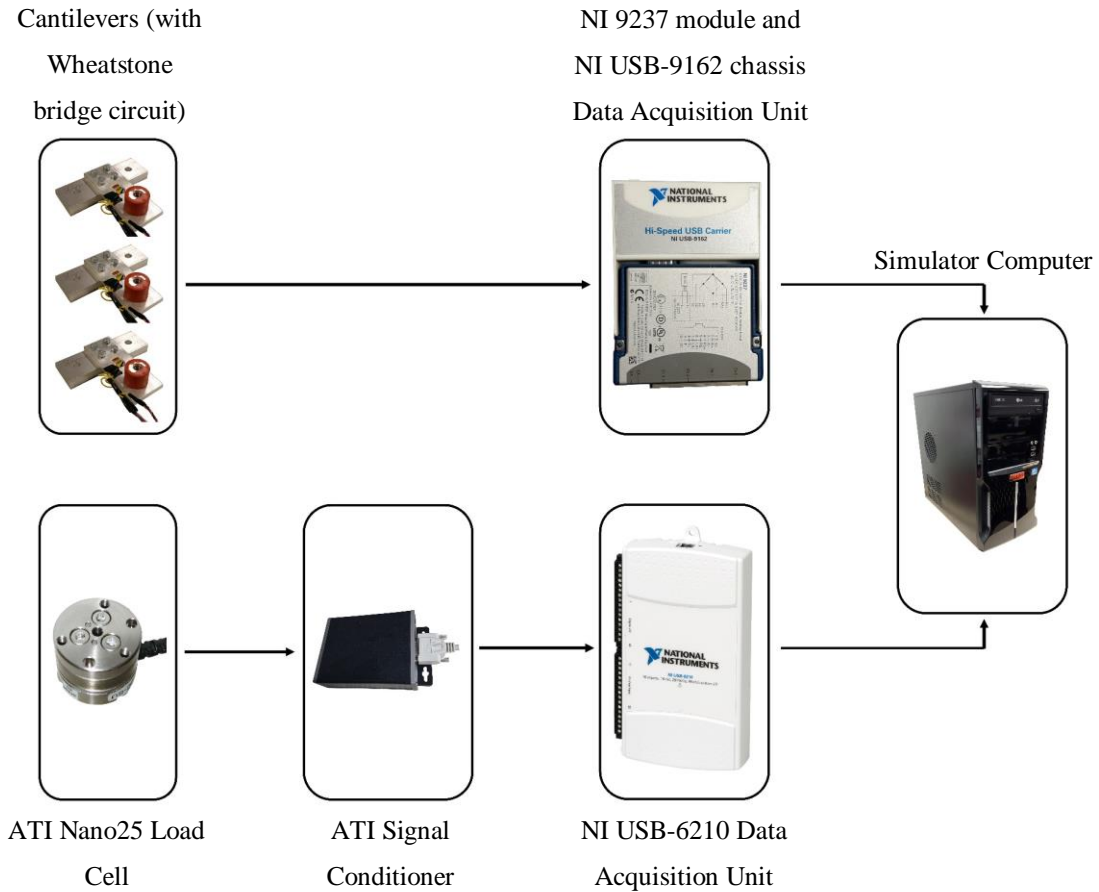


Figure 2.5: Data acquisition system

Three cantilever load cells were used to measure the simulator user's applied force and angle of approach. A commercial load cell was used to calibrate the system. All transducers were sampled via NI-USB data acquisition units using NI LabVIEW software.

2.3 Cantilever Load Cell Calibration

A commercial six degree-of-freedom (6DOF) load cell (Nano25, ATI Technologies, Markham, Ontario) was used to develop a calibration curve for each cantilever load cell. This load cell was used because it was easily accessible; however, measurements were only taken from a single axis to calibrate the cantilevers. This curve was used to convert measured bending strain into normal force applied. Each cantilever was mounted to the

simulator wall support prior to calibration. The load cell was mounted onto one of the cantilevers as shown in Figure 2.6. As shown in Figure 2.5, the load cell was connected to an ATI signal conditioner and was routed to the simulator computer using an USB-6210 data acquisition unit (National Instruments Corporation, Austin, Texas). A custom NI LabVIEW program was used to simultaneously collect strain measurements from the cantilever being calibrated and force measurements from the load cell. The loading protocol for calibration involved applying a steadily increasing and decreasing compressive load followed by an increasing and decreasing tensile load normal to the face of the load cell.

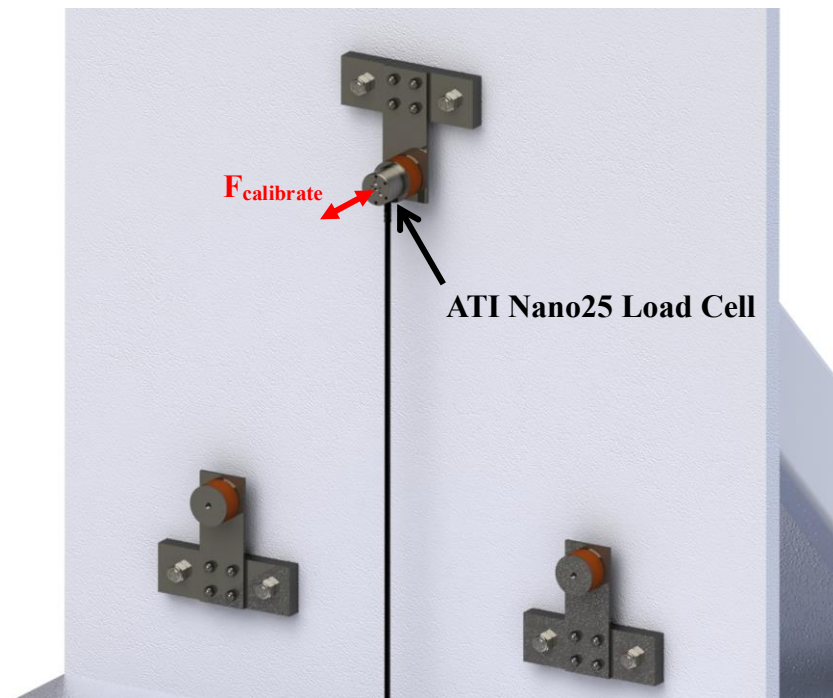


Figure 2.6: Cantilever Load Cell Calibration Setup

An ATI Nano25 load cell was mounted onto each cantilever to calibrate the cantilever to convert measured bending strain into force applied normal to the cantilever. A ramped compressive and tensile load ($F_{calibrate}$) was applied to the load cell while recording measurements from the load cell and cantilevers simultaneously.

A plot was generated with bending strain as the independent variable and force applied as the dependent variable. A first order regression was fit to the plotted points to generate the calibration curve. The developed calibration curves are shown in Figure 2.7 through Figure 2.9. The simulator was mounted onto the three cantilever load cells after they were calibrated.

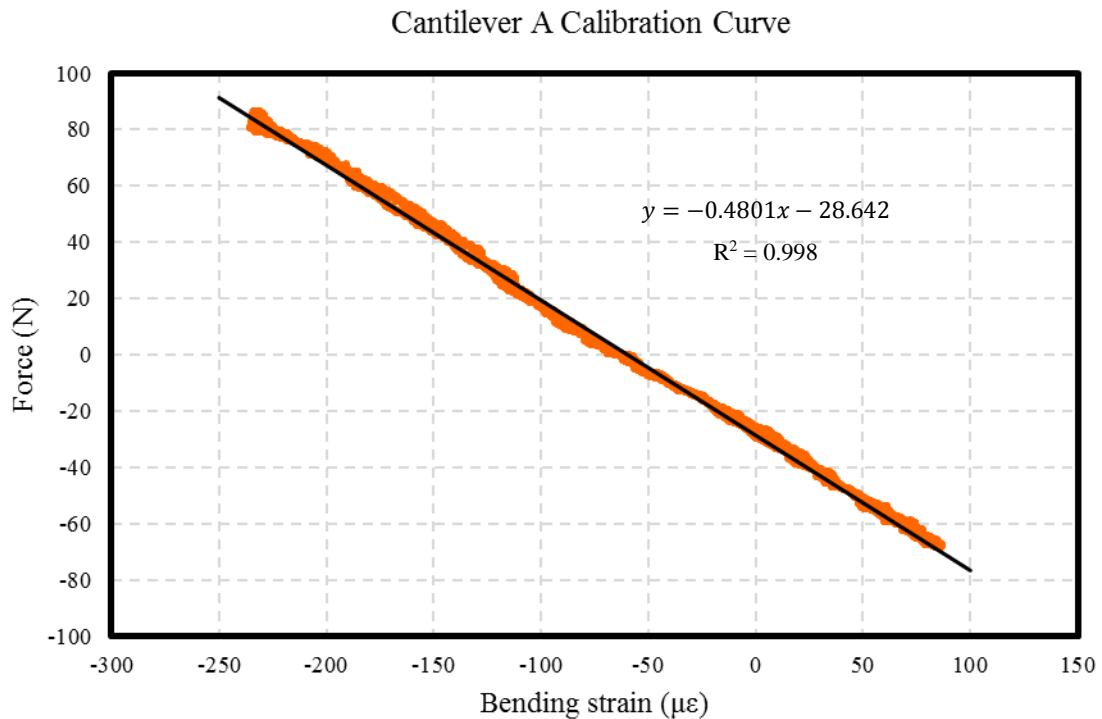


Figure 2.7: Cantilever A Calibration Curve

Calibration data from the commercial load cell and the Wheatstone bridge of cantilever A were plotted on a scatter plot. A line was fit to the points to develop the calibration curve that would allow for the conversion from measured bending strain into force applied.

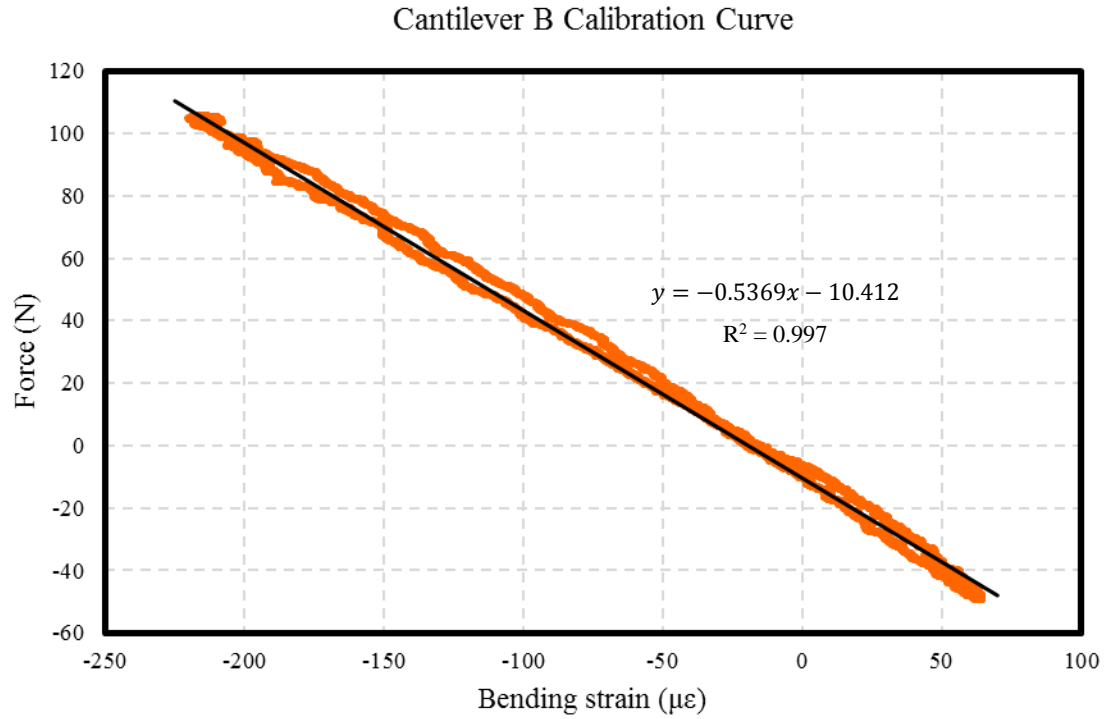


Figure 2.8: Cantilever B Calibration Curve

Calibration data from the commercial load cell and the Wheatstone bridge of cantilever B were plotted on a scatter plot. A line was fit to the points to develop the calibration curve that would allow for the conversion from measured bending strain into force applied.

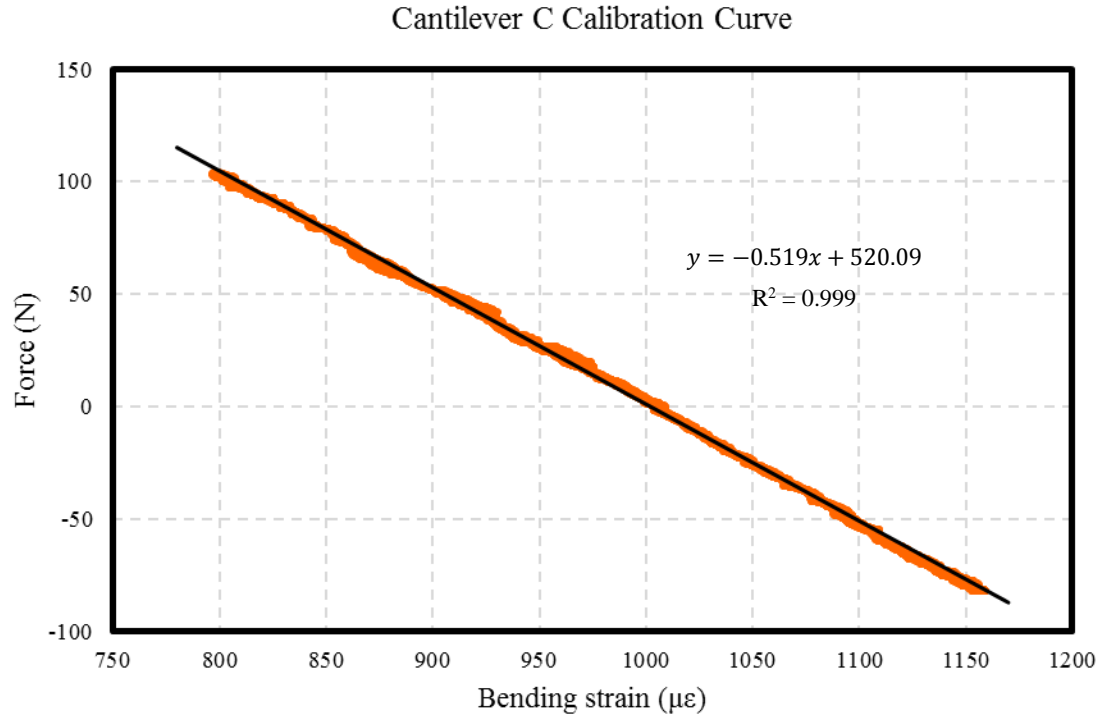


Figure 2.9: Cantilever C Calibration Curve

Calibration data from the commercial load cell and the Wheatstone bridge of cantilever C were plotted on a scatter plot. A line was fit to the points to develop the calibration curve that would allow for the conversion from measured bending strain into force applied.

2.4 Force-based Measurement System Calibration

To calibrate the reamer vector measurement system, a custom mount was used to attach the load cell to the simulator base plate that aligned the measurement axes of the load cell with the simulator coordinate system defined in section 2.1.2 (shown in Figure 2.10A). To apply controlled loads to the load cell, a KUKA 7 axes light weight robot (LWR) (KUKA Robotics Canada Limited, Mississauga, Ontario) was used with a surgical reamer mounted to the effector end of the robot shown in Figure 2.11. A plate with a pilot hole was mounted to the front of the load cell to serve as a guide for the reamer tip (shown in Figure 2.10B). A data acquisition system as shown in Figure 2.5

was used with a custom LabVIEW program to simultaneously measure load cell data and cantilever data.

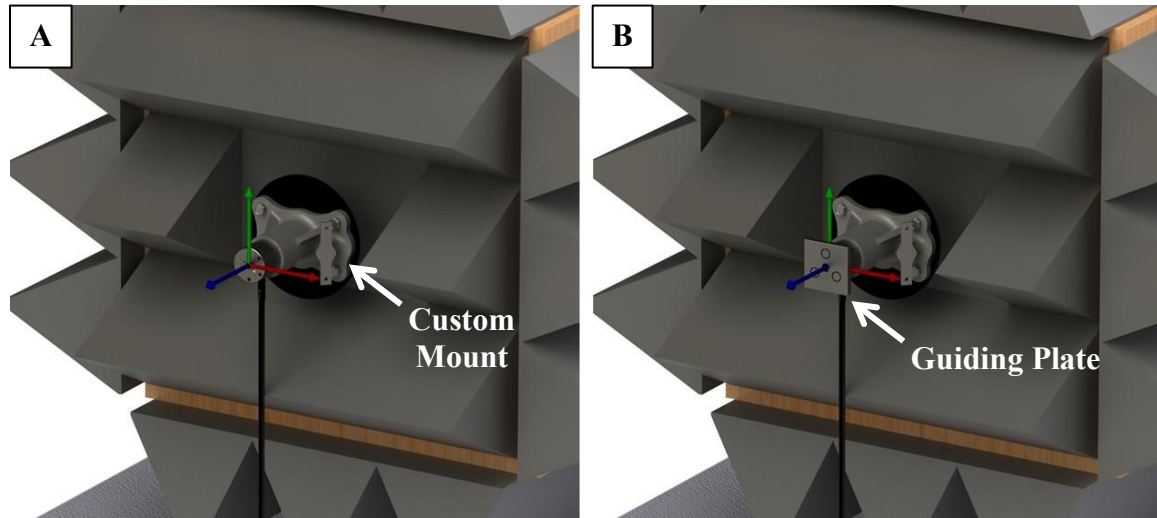


Figure 2.10: Commercial Load Cell Setup for Force-based Measurement System Calibration

[A] A custom mount was used to align the measurement axes of the load cell to the simulator coordinate system axes. [B] A plate with a pilot hole was mounted to the load cell to guide the reamer tip during the loading protocol.

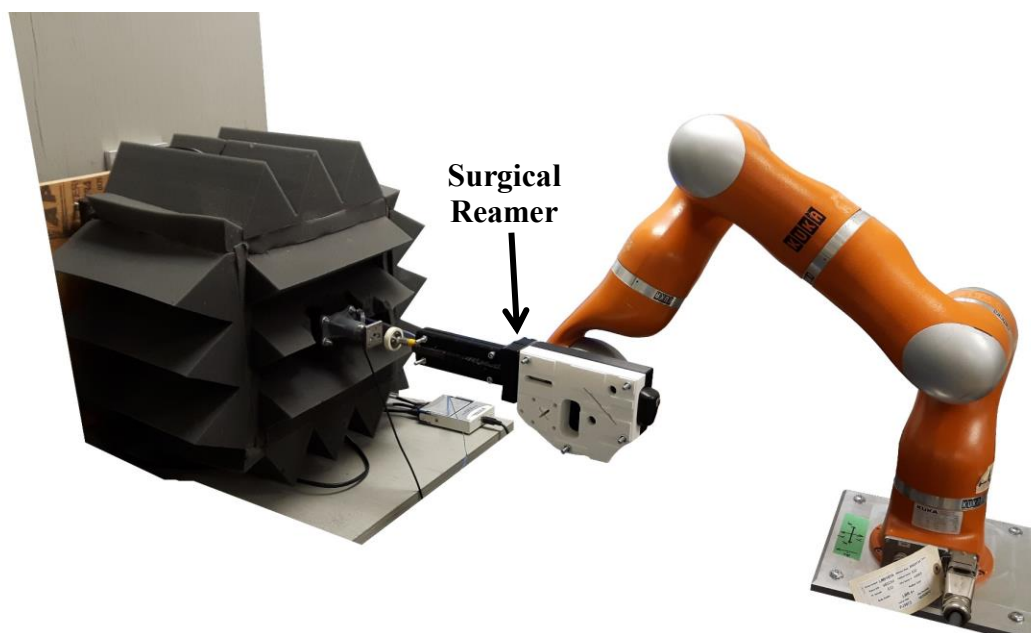


Figure 2.11: KUKA 7 Axes Light Weight Robot and Reamer Mount

A surgical reamer was mounted to a KUKA 7 Axes light weight robot using a custom clamp. The robot was used to apply consistent loads to the commercial load cell mounted to the front of the simulator.

The robot was actuated using position control to apply specific loads to the load cell mounted to the front of the simulator. After recording force data, relationships between the load cell and cantilever data was used to develop calibration equations that would transform measured cantilever forces into net force applied at the user-tool interface and the reamer angle of approach.

To calibrate the system using force magnitudes, an assumption about the reamer angle of approach was needed. Specifically, the orientation of the force vector applied by a surgeon during glenoid reaming was considered collinear with the reamer shaft.

Consequently, the reamer orientation is equivalent to the orientation of the force vector applied to the simulator. Using this assumption, the commercial load cell can be used as the gold standard for calibration of the cantilever force-based reamer vector measurement system.

2.4.1 Measurand Calibration

2.4.1.1 Version Angle Calibration

To develop the version angle calibration algorithm, the KUKA robot was oriented so that the reamer shaft was collinear with ML axes of the load cell and simulator coordinate systems. The robot was advanced into the load cell along the ML axis until a target force was reached. Once the target was reached, the robot was actuated side-to-side along the AP axis to generate a horizontal force component acting on the simulator. This affected the force vector version angle of approach while holding the inclination angle of approach at zero. For each test, the robot was used to gradually sweep through the desired version angle measurement range. The sweep started with a version angle of zero degrees that was increased to +15 degrees of version and then decreased to -15 degrees. Finally, the robot was actuated to bring the version angle back to zero degrees. This version angle sweep was completed for target loads of 20, 40, 60, 80, 100, and 120 N. Using multiple target loads decreased any effect of force magnitude on the calibration curve. To develop the main calibration curve, the collected data for all target loads was plotted on a scatter plot with version angle measured by the load cell as the dependent variable and the version cantilever load ratio (VLR), defined in equation 2.1, plotted as the independent variable as shown in Figure 2.12.

$$VLR = \frac{\text{Cantilever}A}{\text{Cantilever}C} \quad (2.1)$$

By inspection, the data points were noted to approach one vertical and one horizontal asymptote. For this reason, a curve of the following form was chosen for the curve fit operation:

$$y = \frac{a}{x + b} + c \quad (2.2)$$

Where x is the independent variable, y is the dependent variable and a , b and c are the coefficients that are determined by the curve fit. MATLAB was used to fit a curve to the data points using the nonlinear least squares method with the trust-region algorithm. The

plot and curve fit can be seen in Figure 2.12 and the resulting calibration equation is shown in equation 2.3.

$$VersionAngle = \frac{-28.3}{VLR + 1.011} + 15.04 \quad (2.3)$$

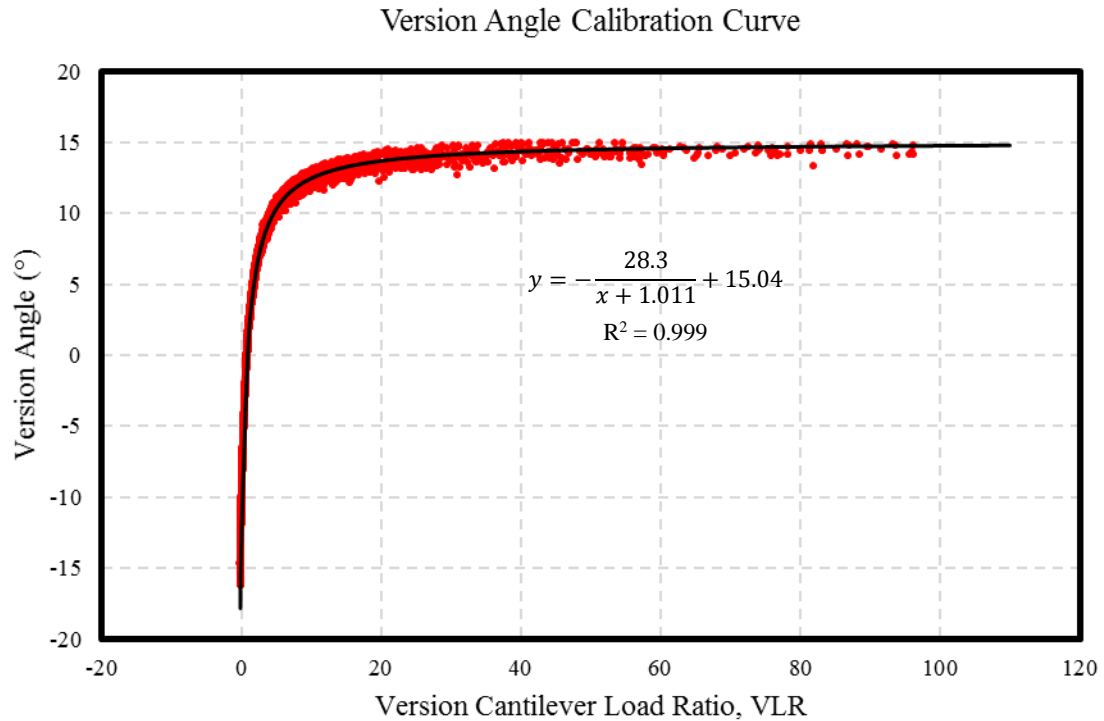


Figure 2.12: Calibration Curve for Version Angle Calculation

Version angle measured by the load cell was plotted on the vertical axis and the version cantilever load ratio was plotted on the horizontal axis. MATLAB was used to fit a curve of the form of equation 1.2 to the version calibration data using a nonlinear least squares method with a trust-region algorithm. This curve formed the main calibration curve for version angle calculation.

The calibration curve is expected to have this form. When a target load is applied along the ML axis, both cantilever A and C measure a similar reaction force. Once a force component along the AP axis is introduced, the force measured by either cantilever A or cantilever C increases while the other decreases. For negative version angles the force on cantilever A approaches zero while the force on cantilever C increases. This causes the VLR to approach zero as the version angle becomes more negative. For positive version angles there is an increase in the force measured by cantilever A and a decrease in the force measured by cantilever C. This causes the VLR to diverge to infinity as the denominator approaches zero.

2.4.1.2 Inclination Angle Calibration

The calibration algorithm for inclination angle was developed similarly to the version angle calibration algorithm. The robot was advanced into the load cell along the ML axis with the reamer shaft collinear with the ML axis until a target load was reached. Once reached, the robot was actuated along the SI axis of the simulator coordinate system to apply a net force vector with a vertical force component. This caused the inclination angle to change while maintaining a zero degree version angle of approach. The robot was used to sweep through the desired inclination angle measurement range. This involved actuating the robot along the SI axis until an inclination angle of 15 degrees was reached. Following this, the robot was actuated in the opposite direction along the SI axis until -15 degrees was reached. Lastly, the robot was brought back to a neutral position where the inclination angle was zero degrees. This process was repeated for target loads of 20, 40, 60, 80, 100, and 120N. Data for all target loads were plotted together on a scatter plot with inclination angle measured by the load cell plotted as the dependent variable and the inclination cantilever load ratio (ILR), defined in equation 2.4, plotted as the independent parameter.

$$ILR = \frac{CantileverB}{CantileverA + CantileverC} \cdot 2 \quad (2.4)$$

A calibration equation in the form of equation 2.2 was fit to the collected data points using a nonlinear least squares line fit with a trust-region algorithm in MATLAB. The output curve had the equation:

$$\text{inclination angle} = \frac{89.44}{\text{Load Ratio} + 2.276} - 22.47 \quad (2.5)$$

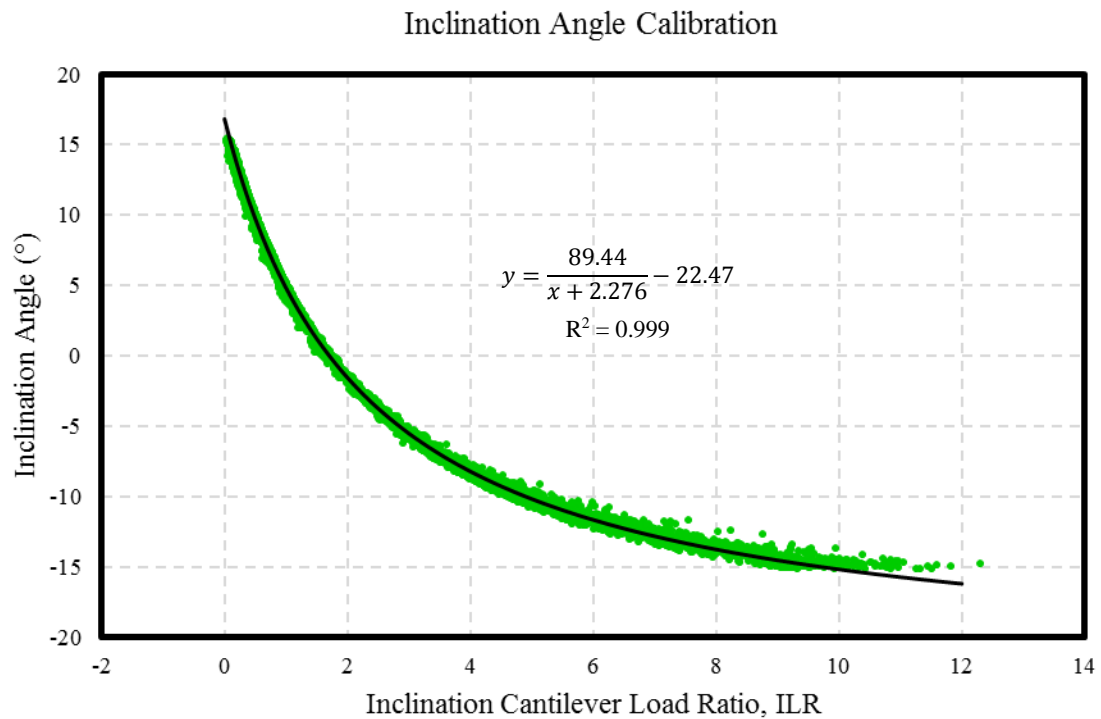


Figure 2.13: Calibration Curve for Inclination Angle Calculation

Inclination angle measured by the load cell was plotted on the vertical axis and the inclination cantilever load ratio was plotted on the horizontal axis. MATLAB was used to fit a curve of the form of equation 2.2 to the version calibration data using a nonlinear least squares method with a trust-region algorithm. This curve formed the main calibration curve for inclination angle calculation.

A calibration curve of this form is expected for inclination angle calibration. When a target force is applied along the ML axis of the simulator, the cantilevers measure similar reaction forces. But when a force component along the SI axis is applied, either the ILR denominator or numerator increases while the other decreases. When there is a positive inclination angle the numerator approaches zero and so does the ILR. When there is a negative inclination angle the denominator approaches zero and the ILR diverges to infinity.

2.4.1.3 Net Force Calibration

The net force magnitude, F_{net} , was calibrated using trigonometric relationships and force balance equations. The net force vector is a vector in 3-dimensional space; therefore, it can be represented as the root sum of squares of three orthogonal force vectors along the simulator coordinate system axes as shown in equation 2.6.

$$F_{net} = \sqrt{F_{SI}^2 + F_{AP}^2 + F_{ML}^2} \quad (2.6)$$

Where F_{SI} , F_{AP} , and F_{ML} are force acting along the SI, AP and ML axes, respectively. This can be represented in terms of F_{ML} and version ($verAngle$) and inclination ($incAngle$) angles using trigonometric relationships.

$$F_{net} = \sqrt{(F_{ML} \cdot \tan(incAngle))^2 + (F_{ML} \cdot \tan(verAngle))^2 + F_{ML}^2} \quad (2.7)$$

By extracting the common factor, equation 2.8 is obtained.

$$F_{net} = F_{ML} \cdot \sqrt{(\tan^2(incAngle) + \tan^2(verAngle) + 1)} \quad (2.8)$$

The force applied normal to the base plate can be calculated from the measured cantilever loads using a force balance equation. By summing the forces along the ML axis, the following equation is obtained:

$$F_{ML} = F_{cantA} + F_{cantB} + F_{cantC} \quad (2.9)$$

Where F_{cantA} , F_{cantB} and F_{cantC} are the forces measured by cantilever A, B and C, respectively. Substituting equation 2.9 into equation 2.8 results in a calibration equation containing measured and calibrated terms of the reamer vector measurement system.

$$F_{net} = (F_{cantA} + F_{cantB} + F_{cantC}) \cdot \sqrt{(\tan^2(incAngle) + \tan^2(verAngle) + 1)} \quad (2.10)$$

2.4.1.4 Initial Calibration Performance Assessment

To assess the performance of the calibration, the KUKA robot was used to sweep across the calibrated measurement range of the system. The robot and load cell were used in the same configuration described earlier in section 2.4. Similar to calibration, the robot was advanced into the load cell along the ML axis until the target load was reached with version and inclination angles of zero degrees. The robot was used to sweep across the entire reamer vector measurement system range. The robot was actuated along the SI axis until an inclination angle of 15 degrees was reached. The robot was then actuated in the opposite direction along the SI axis until -15 degrees was reached. The robot was brought back to a neutral position (inclination angle equal to zero). This was repeated for constant version angles in increments of 2.5 degrees spanning the range of -15 to 15 degrees of inclination. This system sweep was done for target loads of 20, 40, 60, 80, 100 and 120 N.

After completing the load sweeps, the forces and angles measured by the load cell were compared to the forces and angles measured by the reamer vector measurement system. For each measurand, a mean error and mean absolute error between the reamer vector measurement system and the load cell were calculated for the entire measurement range averaged over all target loads. The error summary is shown in Table 2.1.

Table 2.1: Measurement System Sweep Error Summary

	<i>Mean Error</i>	<i>Mean Absolute Error</i>
Version Angle (°)	-0.1 ± 6.0	2.9 ± 5.2
Inclination Angle (°)	0.0 ± 0.4	0.3 ± 0.2
Net Force Magnitude (N)	-3.1 ± 5.1	4.3 ± 4.2

These results show that the most significant errors are found in version angle and net force magnitude measurements. These errors are believed to be from a two main sources. Firstly, the simulator was originally designed to passively simulate the motion of the scapula that occurs when a surgeon applies a force to the glenoid. This adds to the realism of the simulation but complicates the force calibration because the coordinate system moves with the base plate when the user applies a force. This motion changes the distribution of reaction forces between the three cantilever load cells from what would be expected if the system was rigid. This motion results in errors in the net force measurement. The motion causes cosine error between the normal of each cantilever face and the ML axis defined by the base plate. The formula for calculating the normal force magnitude (equation 2.10) assumes that the simulator coordinate system ML axis is normal to the faces of the cantilevers. This assumption is not valid given that the base plate moves causing small changes in the measurement coordinate system orientation and position relative to the cantilevers.

The second main source of error is the instability of the tripod configuration. Figure 2.14 shows that there is an increase in version angle error when there is a non-zero inclination angle. This error is greatest when the inclination angle is negative (when there is a force component acting in the superior direction). In the presence of a non-zero version angle and a negative inclination angle, the simulator tends to twist causing an exaggeration in the version angle measurement resulting from an exaggerated cantilever load ratio measurement. This error is increased as the force applied by the user increases. This

source of error doesn't have as large of an impact on the inclination angle measurement because its affect is normalized due to the load averaging of cantilevers A and C in the inclination angle calibration. When the simulator twists, there is an increase in the force measured by either cantilever A or C and a decrease in the other. This results in an exaggerated load ratio for version angle calibration, but if the increase in load measured by one cantilever is equal to the decrease measured by the other cantilever then the average force measured by both cantilevers would remain unchanged. Therefore, the load ratio, ILR, is largely unaffected.

These errors can be reduced by using correlations between the measurement error and the measurands (measured version angle, inclination angle and net force magnitude) to predict and compensate for the error.

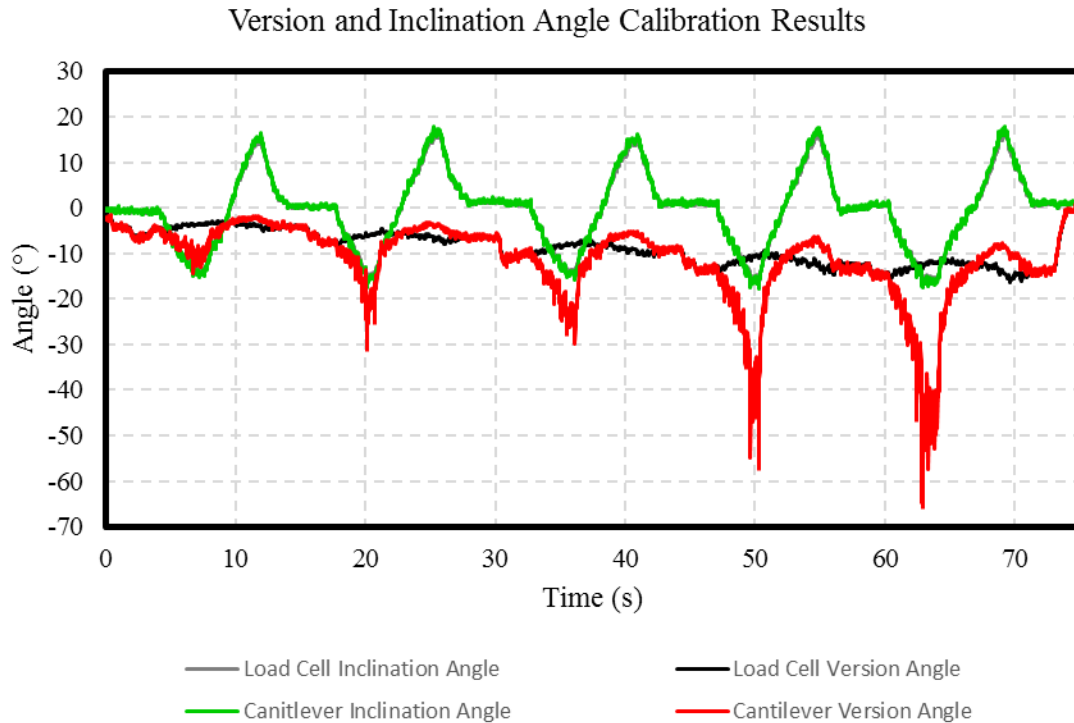


Figure 2.14: Sample Reamer Angle of Approach Output from Force-based Measurement System Calibration

This sample output from the commercial load cell and the force-based measurement system calibration shows that when there is a non-zero inclination angle there is an increased error in the version angle measurement. This error is the result of the unstable tripod configuration.

2.4.2 Error Compensation

Although there were large errors present in the system, they were reduced by predicting the error based on measured parameters. The load sweep data from the initial calibration performance assessment was used to improve the system calibration by observing trends in error as it relates to parameters measured by the cantilevers. Error compensation was performed in stages and the different stages of compensation involved using different error predictors.

2.4.2.1 Error Compensation Summary and Naming Convention

Moving forward, a naming convention will be used to refer to each measurand after calibration and after each stage of error compensation. This naming convention is shown in Table 2.2.

Table 2.2: Measurand Naming Convention and Calibration Summary

		Calibrated	Error Compensation Stage		
			1	2	3
Version Angle	Name	VerC	VerC1	VerC2	VerC3
	Function of:	VLR	VerC, ILR	VerC1, F _{net} C	VerC2, IncC2
Inclination Angle	Name	IncC	IncC1	IncC2	
	Function of:	ILR	IncC, VerC1	IncC1, F _{net} C	
Force along ML axis (F _{ML})	Name	F _{ML} C	F _{ML} C1	F _{ML} C2	F _{ML} C3
	Function of:	Cantilever Loads	F _{ML} C, VerC1	F _{ML} C1, IncC1	F _{ML} C2
Net Force Magnitude (F _{net})	Name	F _{net} C	F _{net} C1	F _{net} C2	F _{net} C3
	Function of:	VerC, IncC, F _{ML} C	VerC1, IncC1, F _{ML} C3	F _{net} C, VerC3	F _{net} C1, IncC2

2.4.2.2 Version Angle Error Compensation

The first stage of version angle error compensation sought to address the error caused by simulator twist with the presence of a non-zero inclination angle. To predict this error, the ILR was plotted as the independent variable on a scatter plot while VerC percent error was plotted as the dependent variable as shown in Figure 2.15. However, for version

angles between -1 and 1 degree, the low signal to noise ratio resulted in very large percent errors in VerC measurement. For this reason, data points corresponding to version angles between -1 and 1 degree were omitted from this stage of the calibration. MATLAB was used to find the line of best fit using a nonlinear least squares method with trust-region algorithm. The stage of calibration resulted in the equation:

$$VerC1 = VerC \cdot \left(\frac{(-25.26 \cdot ILR + 42.89)}{100} + 1 \right)^{-1} \quad (2.11)$$

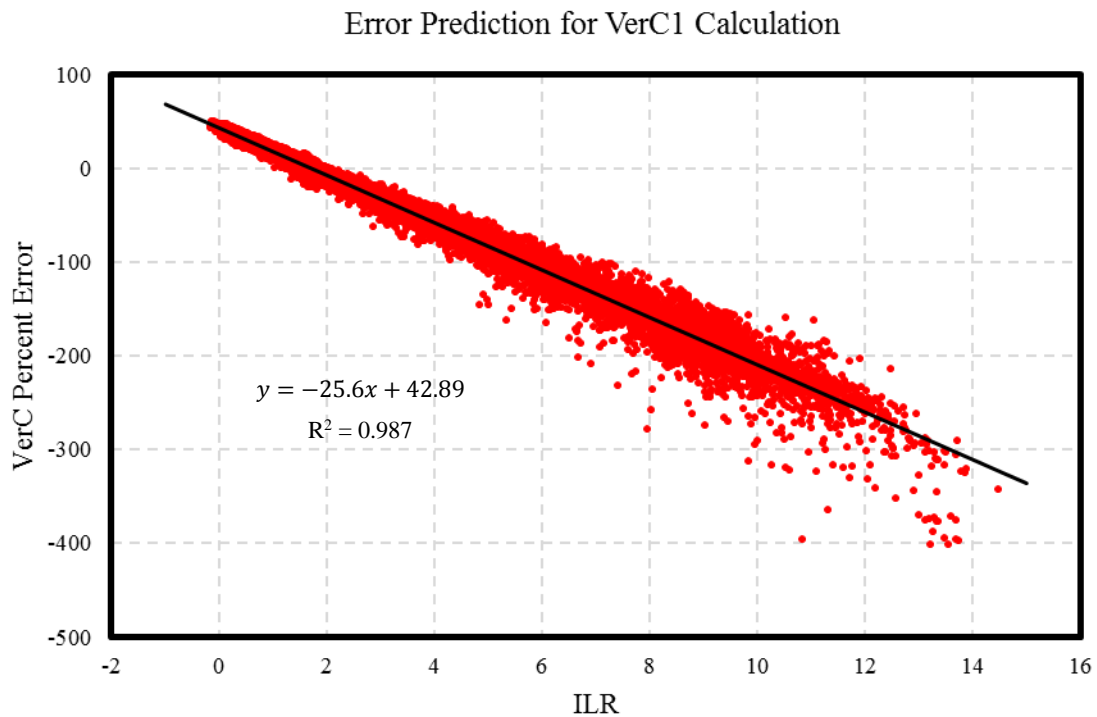


Figure 2.15: Version Angle Error Compensation Stage 1 Calibration Curve

Inclination angle cantilever load ratio (ILR) was used to predict the error in the version angle measurement when a non-zero inclination angle of approach is present. The percent error in the version angle calibration was on the vertical axis and the inclination load ratio was on the horizontal axis. MATLAB was used to find the line of best fit using a nonlinear least squares method with trust-region algorithm. This compensation stage was used to calculate VerC1.

The second stage of error compensation involved plotting $F_{net}C1$ (described in section 2.4.2.5) and $VerC1$ as independent variables and $VerC1$ error in degrees as the dependent variable as shown in Figure 2.16. A third order polynomial surface was fit to the data points using the nonlinear least squares method and trust-region algorithm in MATLAB.

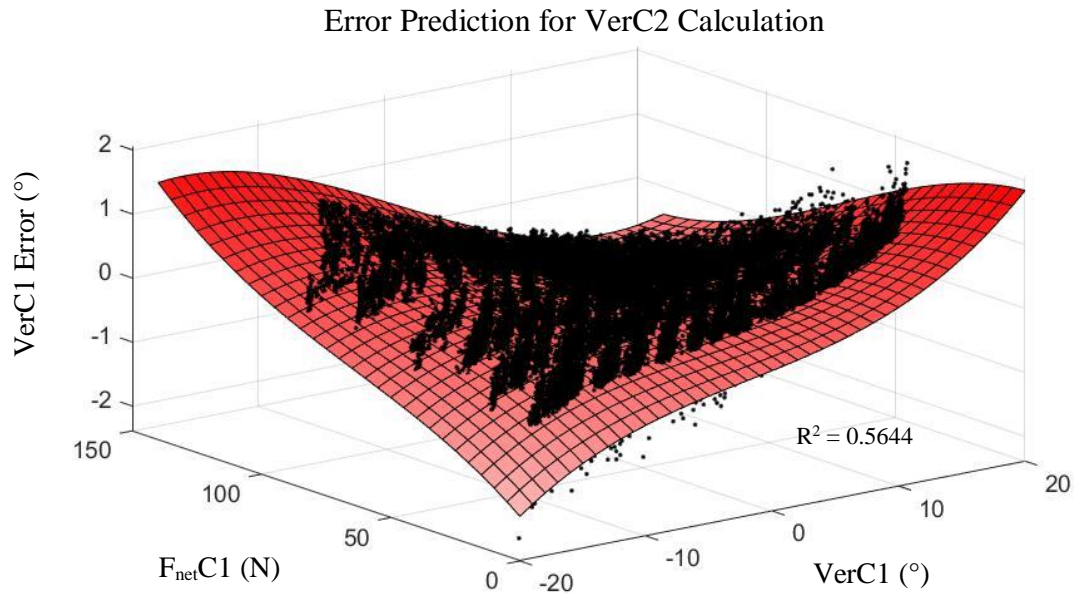


Figure 2.16: Version Angle Error Compensation Stage 2 Surface Fit

The error in version angle measurement with one stage of error compensation was plotted as the dependent variable on a 3D scatter plot and net force and version angle were plotted as the dependent variables. A third order polynomial surface was fit to the data points using the nonlinear least squares method and trust-region algorithm in MATLAB. This calibration was used to calculate VerC2

This stage of calibration resulted in equation 2.12.

$$\begin{aligned}
 VerC2 = VerC1 - & (-0.1926 + 0.04115 \cdot VerC1 \\
 & - 0.0518 \cdot F_{net}C1 + 0.0006685 \cdot VerC1^2 \\
 & - 0.0008999 \cdot VerC1 \cdot F_{net}C1 - 0.0002744 \\
 & \cdot F_{net}C1^2 + 0.0001177 \cdot VerC1^3 - 1.63E - 06 \\
 & \cdot VerC1^2 \cdot F_{net}C1 - 6.91E - 07 \cdot VerC1 \\
 & \cdot F_{net}C1^2 + 1.38E - 06 \cdot F_{net}C1^3)
 \end{aligned} \tag{2.12}$$

The final stage of error compensation for version angle involved plotting VerC2 error in degrees as the dependent variable and IncC2 (described in section 2.4.2.3) as the independent variable on a scatter plot as shown in Figure 2.17. MATLAB was used to find the line of best fit. The resulting equation is shown in equation 2.13.

$$VerC3 = VerC2 - (0.0172 \cdot IncC2 + 0.0036) \tag{2.13}$$

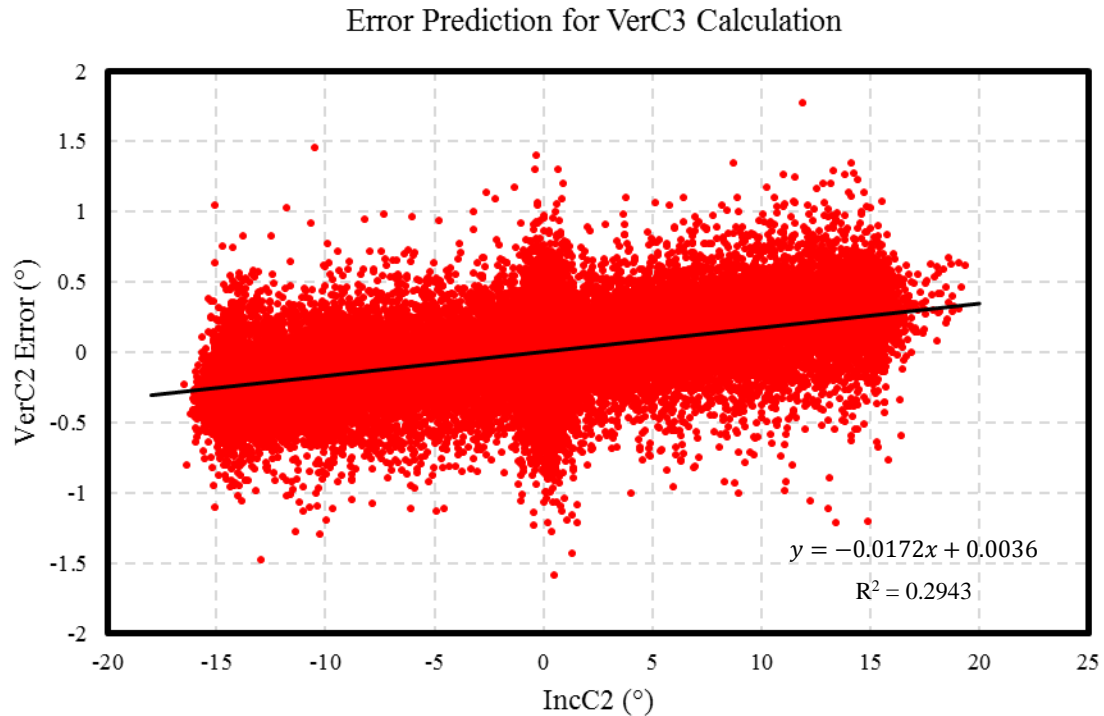


Figure 2.17: Version Angle Error Compensation Stage 3 Calibration Curve

Inclination angle (IncC2) was used to predict the error in the version angle measurement. The error in the second stage of version angle error compensation was on the vertical axis and inclination angle was on the horizontal axis. MATLAB was used to find the line of best fit using a nonlinear least squares method with trust-region algorithm. This compensation stage was used to calculate VerC3.

2.4.2.3 Inclination Angle Error Compensation

The first stage of error compensation for inclination calibration involved determining the relationship between IncC error and VerC. To determine the error compensation curve, VerC1 (described in section 0) was plotted on the independent axis and IncC error in degrees was plotted on the dependent axis as shown in Figure 2.18. The nonlinear least squares curve fitting method in MATLAB was used to find the line of best fit using the trust-region algorithm. The resulting compensation equation is shown in equation 2.14.

$$IncC1 = IncC + (0.01327 \cdot VerC1 - 0.04412) \quad (2.14)$$

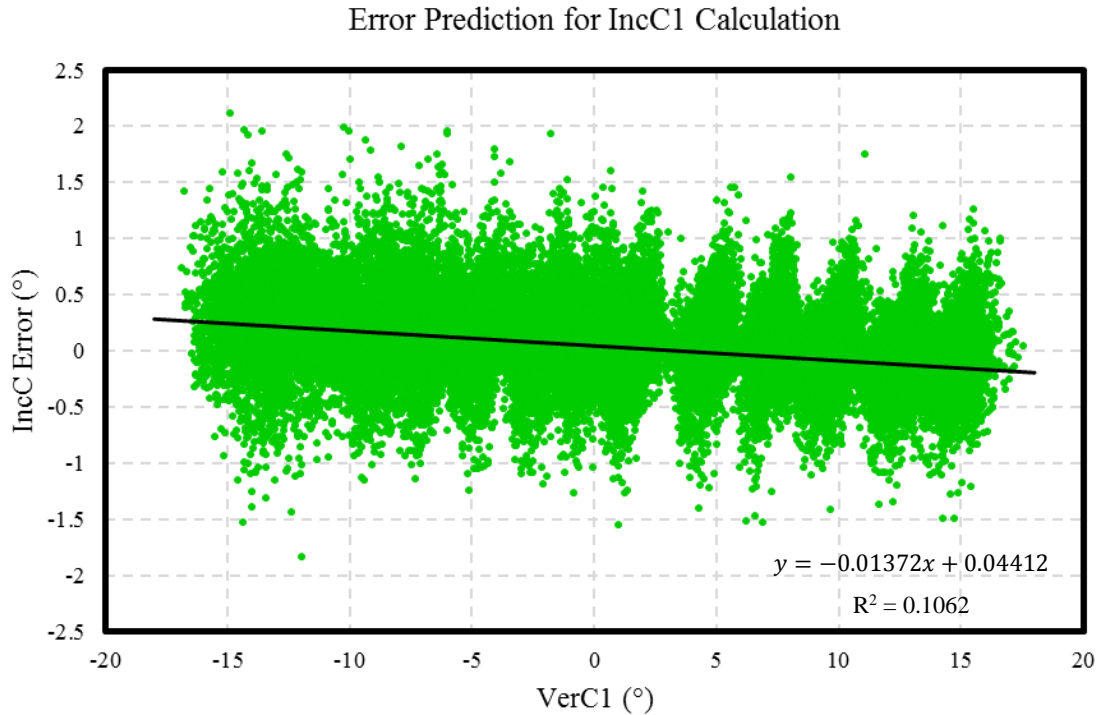


Figure 2.18: Inclination Angle Error Compensation Stage 1 Calibration Curve

Version angle (VerC2) was used to predict the error in the inclination angle measurement. Inclination angle calibration error was on the vertical axis and version angle was on the horizontal axis. MATLAB was used to find the line of best fit using a nonlinear least squares method with trust-region algorithm. This compensation stage was used to calculate IncC1.

The second stage of error compensation for inclination angle involved plotting a 3D scatter plot with $F_{net}C1$ (described in section 2.4.2.5) and $IncC1$ as dependent variables and $IncC1$ error in degrees as the dependent variable. Within MATLAB a third order surface polynomial was fit to the collected data using a nonlinear least squares method with trust-region algorithm. The surface equation is shown in equation 2.15 and the surface fit is shown in Figure 2.19.

$$\begin{aligned}
 IncC2 = IncC1 & \\
 & - (0.4329 + 0.04305 \cdot IncC1 \\
 & - 0.01693 \cdot F_{net}C1 - 0.000568 \cdot IncC1^2 \\
 & - 0.00104 \cdot IncC1 \cdot F_{net}C1 \quad (2.15) \\
 & + 0.00022 \cdot F_{net}C1^2 + 0.000113 \cdot IncC1^3 \\
 & + 1.21E - 05 \cdot IncC1^2 \cdot F_{net}C1 + 2.55E - 06 \\
 & \cdot IncC1 \cdot F_{net}C1^2 - 9.78E - 07 \cdot F_{net}C1^3)
 \end{aligned}$$

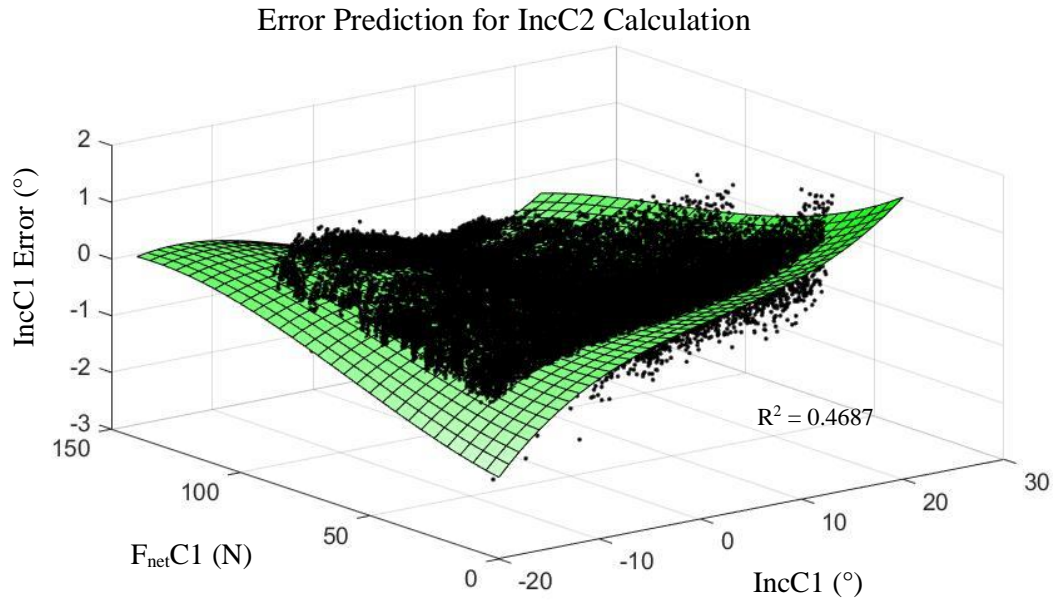


Figure 2.19: Inclination Angle Error Compensation Stage 2 Surface Fit

The error in inclination angle measurement with one stage of error compensation was plotted as the dependent variable and net force and inclination angle were plotted as the independent variables. A third order polynomial surface was fit to the data points using the nonlinear least squares method and trust-region algorithm in MATLAB.

2.4.2.4 F_{ML} Magnitude Error Compensation

The force measured on the ML axis, F_{ML}, requires three stages of error compensation.

The first stage of calibration involved plotting VerC1 (described in section 2.4.1.1) as the independent variable and F_{MLC} percent error as the dependent variable on a scatter plot as shown in Figure 2.20. MATLAB was used to determine the line of best fit using a nonlinear least squares method with a trust-region algorithm. The final equation is shown in equation 2.16.

$$F_{MLC1} = F_{MLC} \cdot \left(\frac{(-0.033 \cdot VerC1 + 0.021)}{100} + 1 \right)^{-1} \quad (2.16)$$

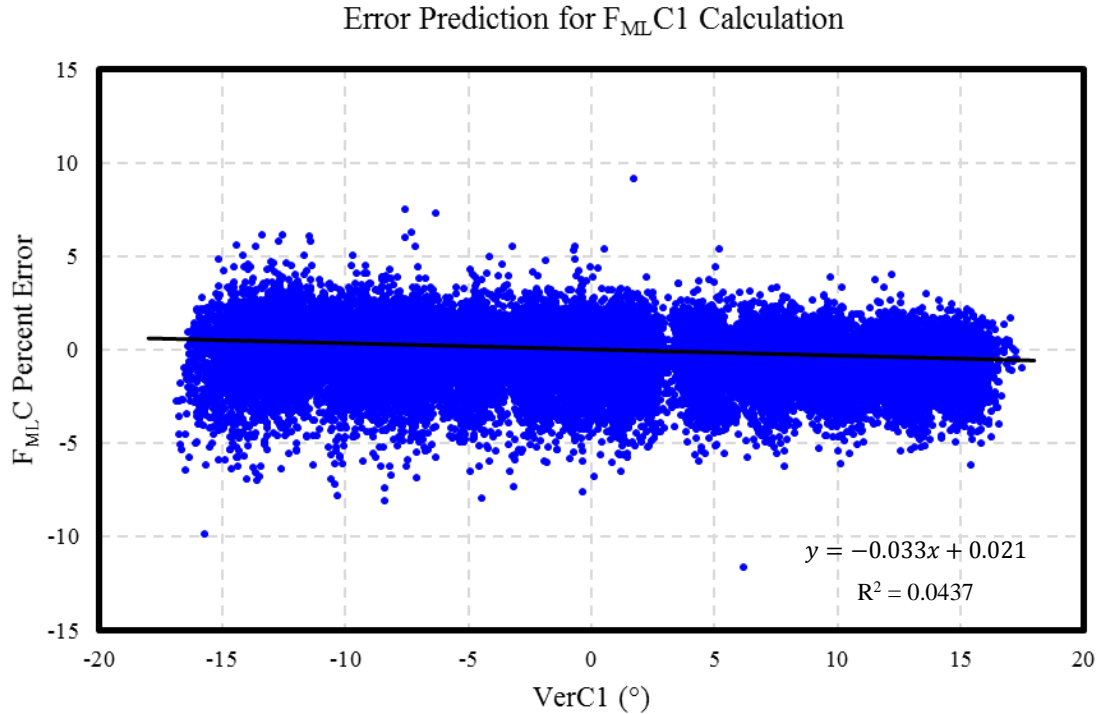


Figure 2.20: Force on ML Axis Error Compensation Stage 1 Calibration Curve

Version angle ($VerC1$) was used to predict the error in the F_{ML} measurement. The percent error in the calibration for the force acting along the ML axis was on the vertical axis and version angle was on the horizontal axis. MATLAB was used to find the line of best fit using a nonlinear least squares method with trust-region algorithm. This compensation stage was used to calculate $F_{ML}C1$.

In the second stage, MATLAB was used to determine the linear relationship between $F_{ML}C$ percent error and $IncC1$ (described in section 2.4.2.3) as shown in Figure 2.21. A nonlinear least squares method with trust-region algorithm was used. The resulting equation was:

$$F_{ML}C2 = F_{ML}C1 \cdot \left(\frac{(-0.3109 \cdot IncC1 - 6.513)}{100} + 1 \right)^{-1} \quad (2.17)$$

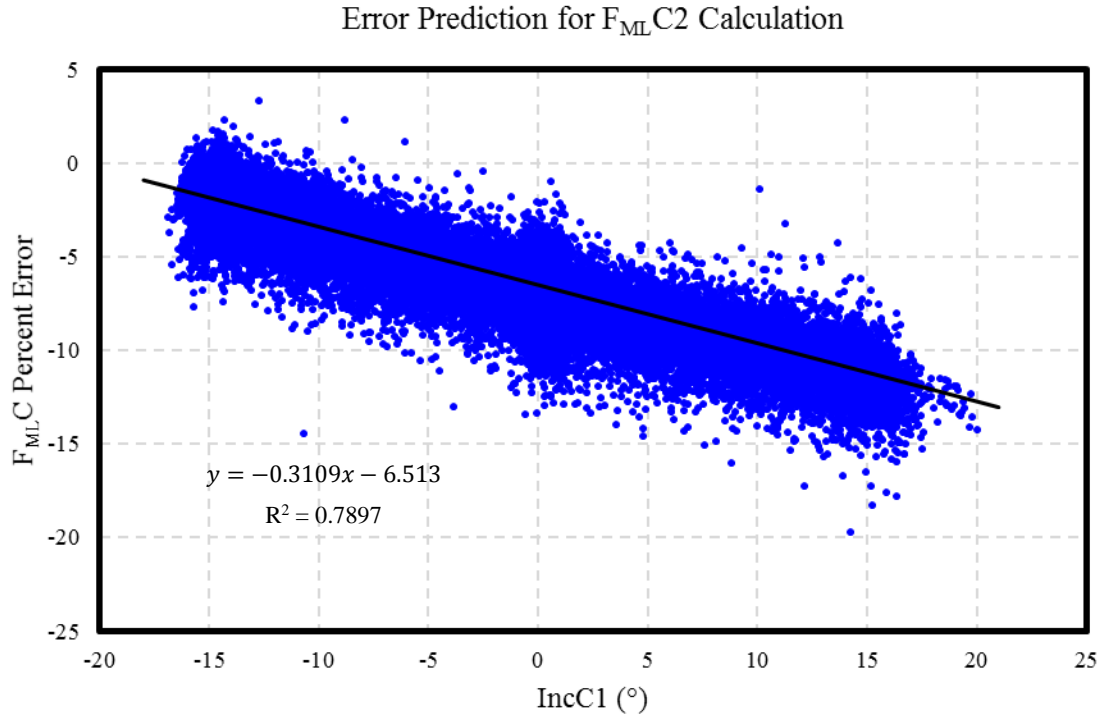


Figure 2.21: Force on ML Axis Error Compensation Stage 2 Calibration Curve
Inclination angle ($IncC1$) was used to predict the error in the F_{ML} measurement. The percent error in the calibration for the force acting along the ML axis was on the vertical axis and inclination angle was on the horizontal axis. MATLAB was used to find the line of best fit using a nonlinear least squares method with trust-region algorithm. This compensation stage was used to calculate $F_{ML}C2$.

The final stage of error compensation for F_{ML} involved plotting $F_{ML}C2$ as the independent variable and F_{ML} error in Newtons as the dependent variable as shown in Figure 2.22. MATLAB was used to find the line of best fit. Equation 2.18 shows the equation for the last stage of error compensation for F_{ML} .

$$F_{ML}C3 = F_{ML}C2 \cdot \left(\frac{(0.0146 \cdot F_{ML}C2 - 0.672)}{100} + 1 \right)^{-1} \quad (2.18)$$

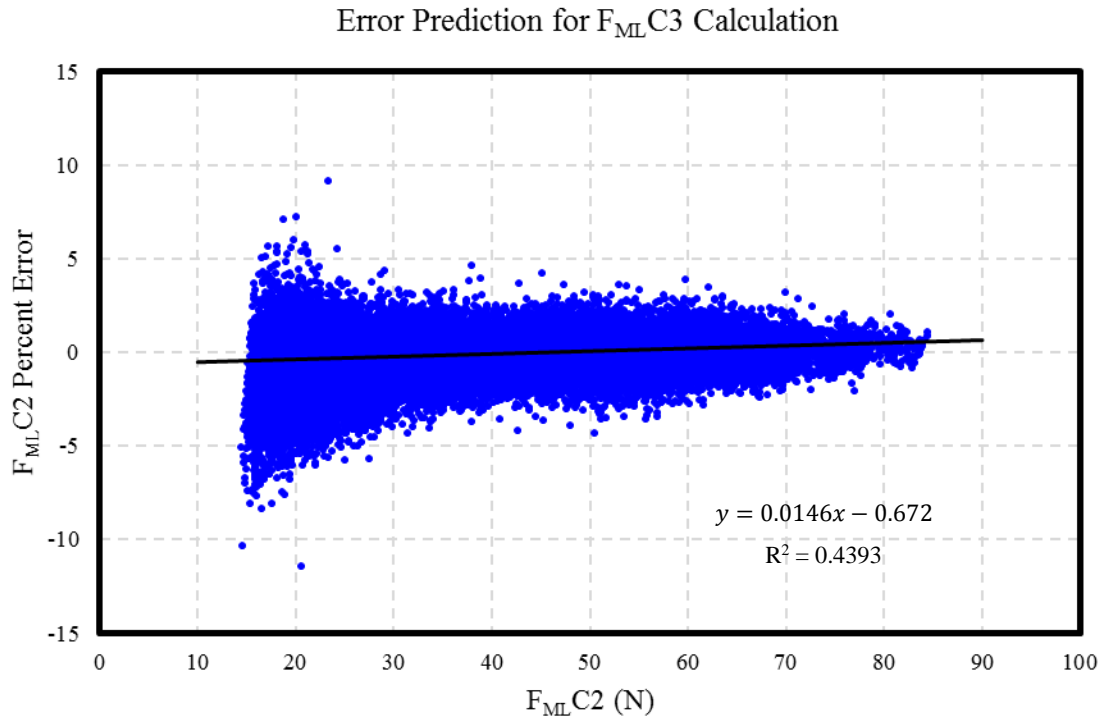


Figure 2.22: Force on ML Axis Error Compensation Stage 3 Calibration Curve

Force along the ML axis ($F_{ML}C2$) was used to predict the error in the F_{ML} measurement. Percent error of the second stage of error compensation for the force acting along the ML axis was on the vertical axis and the force magnitude of the force component acting along the ML axis was on the horizontal axis. MATLAB was used to find the line of best fit using a nonlinear least squares method with trust-region algorithm. This compensation stage was used to calculate $F_{ML}C3$.

2.4.2.5 Net Force Error Compensation

Net force error compensation involved three stages. Unlike the other measurands, the net force initial calibration accuracy is dependent on the accuracy of the other three measurand calibrations. Therefore, the first stage of error compensation used for the net force magnitude involved using equation 2.10 but substituting in measurands with error compensation included. This is shown in equation 2.19.

$$F_{net}C1 = F_{ML}C3 \cdot \sqrt{(\tan^2(VerC1) + \tan^2(IncC1) + 1)} \quad (2.19)$$

In the second stage, net force ($F_{net}C1$) error in newtons was plotted as the dependent variable and version angle ($VerC2$) was plotted as the independent variable on a scatter plot as shown in Figure 2.23. MATLAB was used to fit a second order polynomial to the data points using a nonlinear method with trust-region algorithm. The following equation resulted.

$$F_{net}C2 = F_{net}C1 - (0.0014 \cdot VerC3^2 - 0.0079 \cdot IncC3 - 0.118) \quad (2.20)$$

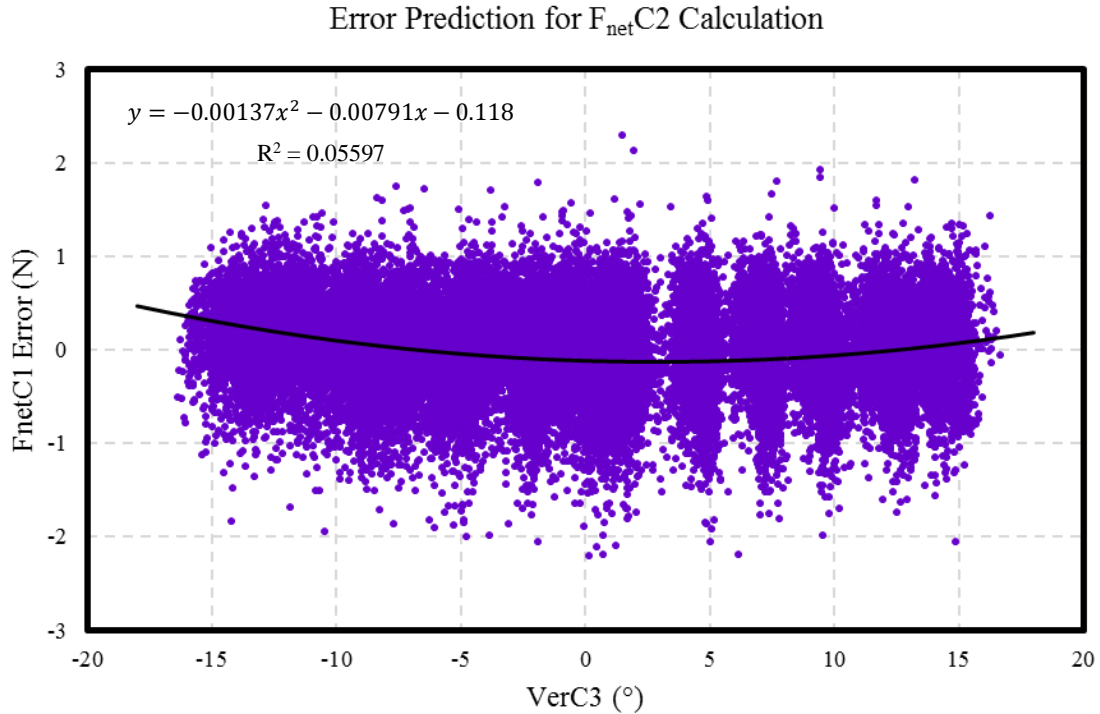


Figure 2.23: Net Force Error Compensation Stage 2 Calibration Curve

Version angle (VerC3) was used to predict the error in the F_{net} measurement. The error in the first error compensation stage for net force magnitude was on the vertical axis and version angle was plotted on the horizontal axis. MATLAB was used to find the line of best fit using a nonlinear least squares method with trust-region algorithm. This compensation stage was used to calculate $F_{net}C2$.

The third stage of error compensation was similar to the second except inclination angle (IncC3) was plotted as the dependent variable instead of version angle as shown in Figure 2.24. The resulting equation is shown in equation 2.21.

$$F_{net}C3 = F_{net}C2 - (0.0016 \cdot Inc2^2 + 0.003 \cdot IncC2 - 0.116) \quad (2.21)$$

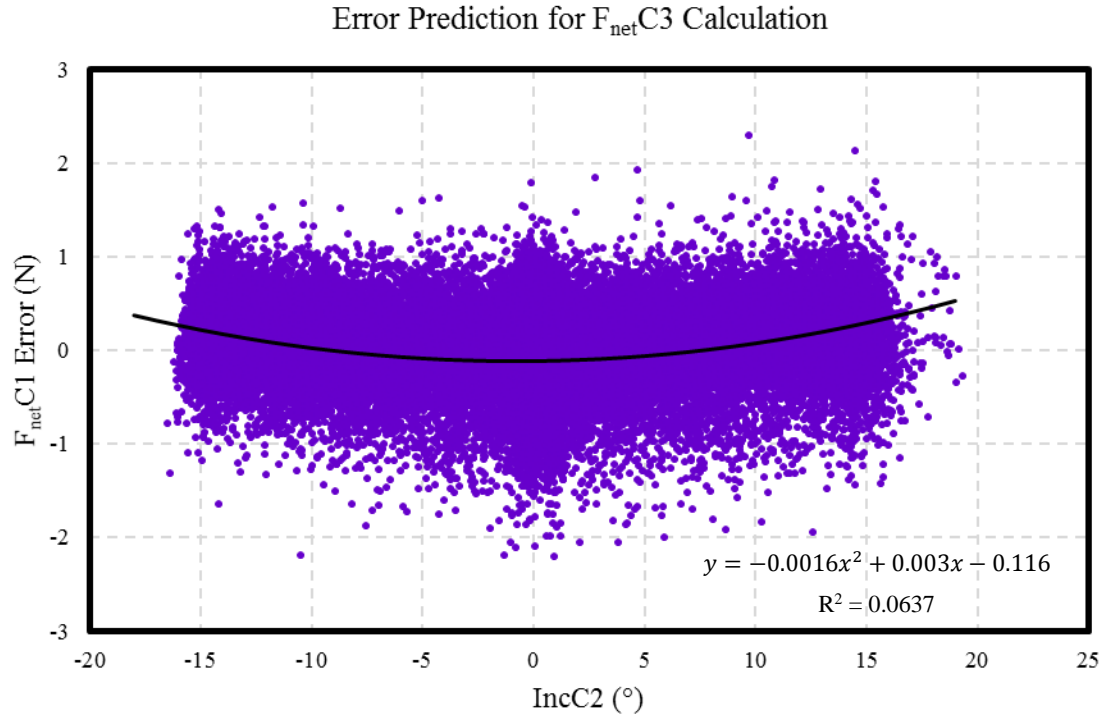


Figure 2.24: Net Force Error Compensation Stage 3 Calibration Curve

Inclination angle (IncC2) was used to predict the error in the F_{net} measurement. The error in the first error compensation stage for net force magnitude was on the vertical axis and inclination angle was plotted on the horizontal axis. MATLAB was used to find the line of best fit using a nonlinear least squares method with trust-region algorithm. This compensation stage was used to calculate $F_{net}C3$.

2.5 Final Calibration Performance Assessment

To assess the overall performance of the calibration and error compensation algorithms a procedure similar to section 2.4.1.4 was used. The robot was aligned with the simulator so that the reamer shaft was collinear with the ML-axis of the load cell. The robot was advanced along the ML-axis into the load cell until a target load was reached. The starting force vector orientation was zero degrees of version and inclination. The robot was actuated along the SI axis until an inclination angle of 15 degrees was reached. Once 15 degrees was reached the robot was actuated in the opposite direction along the SI axis

until -15 degrees was achieved. Finally, the robot was returned to a neutral position (0 degrees of inclination). This was repeated for version angles held constant in 2.5 degree increments spanning the range of -15 to 15 degrees of version. This procedure was repeated for swapped conditions for version and inclination angles. Instead of sweeping through inclination angles and holding version angles constant, a version angle sweep was conducted for constant inclination angles. To do this, the robot was advanced along the ML-axis until the target force was reached. The starting vector orientation was zero degrees of version and inclination. The robot was actuated along the AP-axis until a version angle of 15 degrees was reached. The robot was then actuated in the opposite direction until -15 degrees of version was achieved. Finally, the robot was brought back to a neutral version angle of zero degrees. This protocol was repeated for constant inclination angles spanning the measurement range of -15 to 15 degrees of inclination in 2.5 degree increments. This was repeated for target loads of 20, 40, 60, 80, 100 and 120 N. This entire protocol, including all target loads and both sweeping patterns was completed five times to determine the calibration repeatability.

To determine repeatability, SPSS was used to calculate the intraclass correlation coefficient (ICC) for version angle error, inclination angle error and net force magnitude error across all five trials with a two-way mixed model with absolute agreement. When using a single measure, the ICCs were 0.655, 0.786 and 0.593 for version angle error, inclination angle error and net force magnitude error, respectively. Using average measures, the resulting ICCs were 0.905, 0.948 and 0.879 for version angle error, inclination angle error and net force magnitude error, respectively. The reliability for average measures is regarded as good to excellent for all three measurands [71]. Therefore, the errors reported are average measurement errors from all five trials.

The mean error and mean absolute error for the entire measurement range were calculated for each measurand averaged across all five trials. Table 2.3 shows a summary of the errors.

Table 2.3: Force Measurement System Error Summary

	<i>Mean Error</i>	<i>Mean Absolute Error</i>
Version Angle (°)	0.0 ± 0.2	0.2 ± 0.2
Inclination Angle (°)	-0.1 ± 0.3	0.2 ± 0.2
Net Force Magnitude (N)	0.0 ± 0.5	0.4 ± 0.3

The error summaries show that the error prediction algorithms were successful in reducing the errors in the system. Although the overall errors of the measurement system are sufficiently low, it is of interest to examine the error of the system as a function of measured version and inclination angle. To examine this, the data points were grouped into bins based on measured version and inclination angle. The measurement range for version and inclination angle was broken into 13 bins with bin centers spaced 2.5 degrees apart starting at -15 degrees and finishing at 15 degrees. Each bin was 2.5 degrees wide. Measurement errors for all three measurands were average for all data points contained in a bin. The resulting averages were plotted as a 3D surface with version and inclination angle measured by the cantilevers as the dependent variables and the measurement error plotted on the vertical axis.

Figure 2.25 shows the resultant plot for version angle error binning and averaging. The maximum positive error was 0.2 degrees for 15 degrees of version and 15 degrees of inclination. The maximum negative error was -0.1 degrees for 2.5 degrees of version and -15 degrees of inclination.

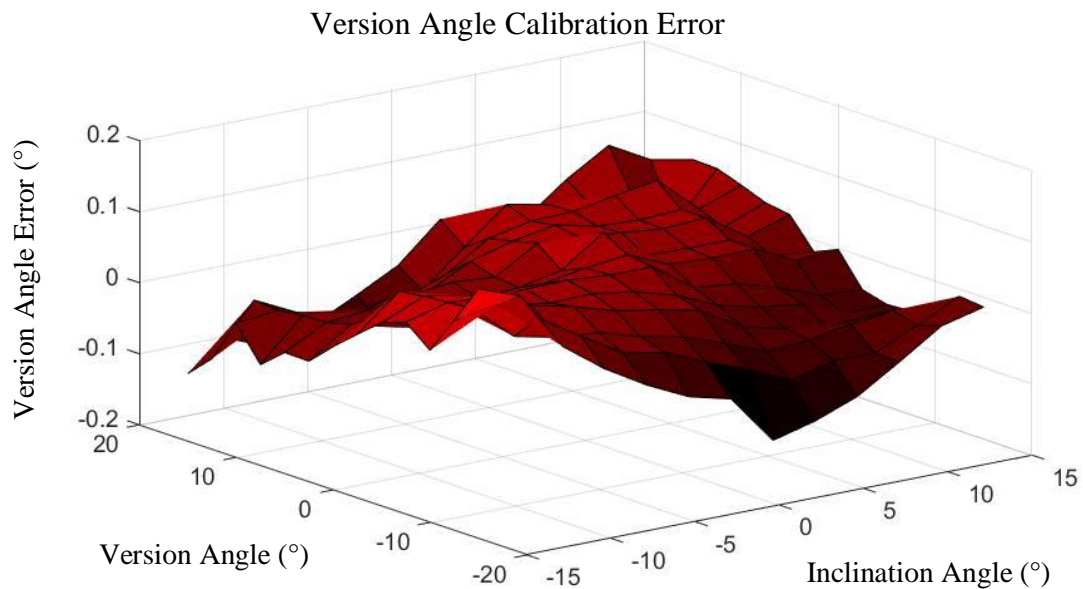


Figure 2.25: Version Angle Error After Calibration and Error Prediction

Surface plot of version angle error as a function of inclination and version angle measured by the cantilever force-based measurement system.

Figure 2.26 shows the resultant plot for inclination angle error binning and averaging. The maximum positive error was 0.1 degrees for 15 degrees of version and -12.5 degrees of inclination. The maximum negative error was -0.4 degrees for zero degrees of version and 15 degrees of inclination.

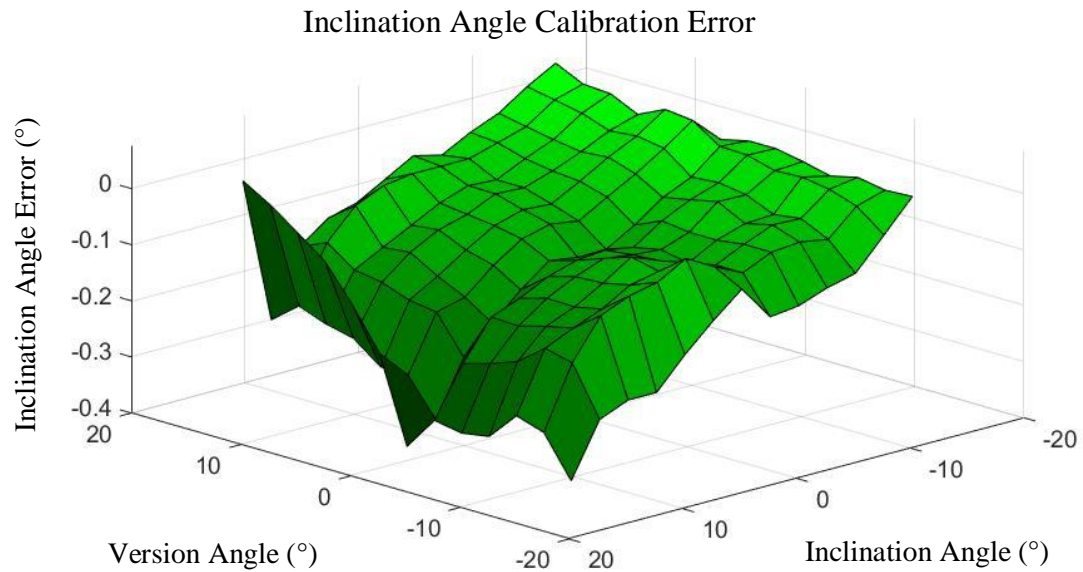


Figure 2.26: Inclination Angle Error After Calibration and Error Prediction

Surface plot of inclination angle error as a function of inclination and version angle measured by the cantilever force-based measurement system.

Figure 2.27 shows the error results for binning net force measurement errors. The maximum positive error was 0.3 Newtons for -15 degrees of version and -15 degrees of inclination. The maximum negative error was 0.4 Newtons for 12.5 degrees of version and 12.5 degrees of inclination.

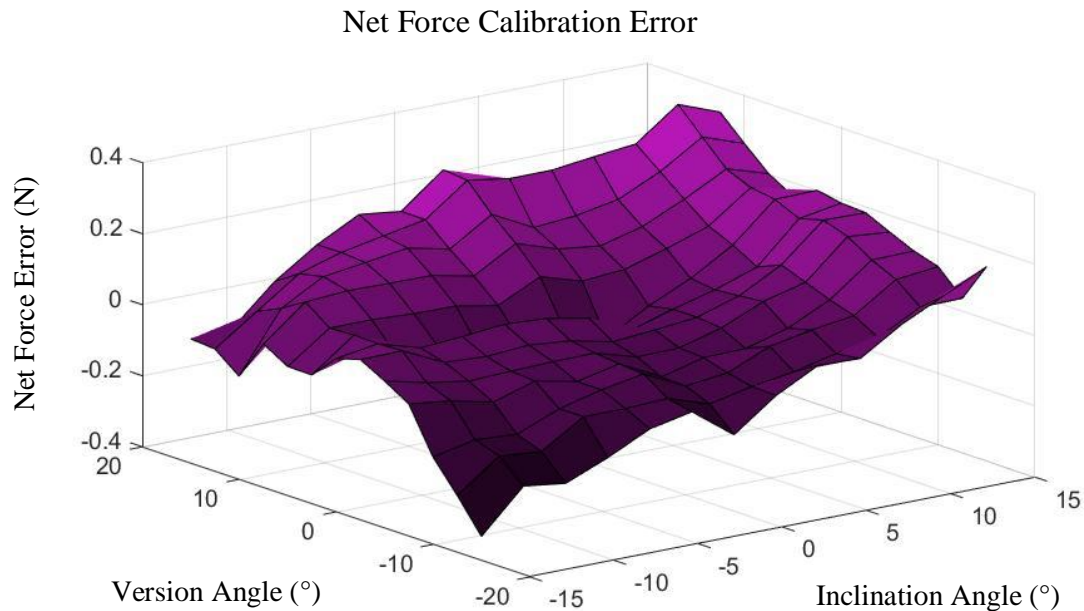


Figure 2.27: Net Force Error After Calibration and Error Prediction

Surface plot of net force error as a function of inclination and version angle measured by the cantilever force-based measurement system.

There do appear to be trends in the measurand errors; however, these errors are not considered significant and there would not be much added value in attempting to calibrate these errors out further. The errors are considered sufficiently low to proceed to further studies.

2.6 Summary

This chapter outlined the design and calibration of a force-based measurement system for a glenoid reaming simulator. This system uses force information to measure the net force applied to the simulator using a surgical reamer as well as the reamer's angle of approach.

First, a clinically relevant coordinate system was developed using scapular anatomical landmarks and this coordinate system was translated onto the simulator to be used with the shoulder model mounted to the simulator. Using these coordinate systems, the desired measurands for the reamer vector measurement system were defined. Following this, a cantilever-based force measurement system was designed and calibrated. However, there were significant maximum errors of 50 degrees for version angle, 2 degrees for inclination angle and 120 Newtons for net force magnitude found after calibration so multiple stages of error prediction and compensation were applied to reduce the system errors. Finally, the error of the system was investigated as a function of the inclination angle and version angle measured by the reamer vector measurement system. The mean absolute errors for version angle, inclination angle and net force magnitude were 0.2 ± 0.2 degrees, 0.2 ± 0.2 degrees and 0.4 ± 0.3 N, respectively.

The aforementioned results demonstrate that the reamer vector measurement system can measure the net force applied to the simulator as well as the reamer's angle of approach without the need for additional tracking hardware. In this chapter, the force-based measurement system has shown to be reliable and accurate when applying a force using a robot in position control. In conclusion, a reliable measurement system has been developed and tested for use in a glenoid reaming simulator.

Chapter 3

3 Reamer Vector Measurement System Error Characterization

Overview: This chapter outlines the error characterization of the reamer vector measurement system including the experimental setup and an outline of the measurement systems used. A reamer coordinate system is defined. The error of each measurand is examined in detail and the sources of error are discussed.

The previous chapter explored the error of the developed reamer vector measurement system using a robot controlled with position control. With this method of control, the reamer was used to apply a changing net force vector to the simulator while holding the reamer orientation constant. The assumption that the reamer shaft and the net force vector orientation are collinear allowed for this manner of calibration. However, controlling the robot with force control and varying the reamer angle of approach would be more representative of a typical glenoid reaming procedure. It is important to understand the error of the reamer vector measurement system using a more clinically relevant method of control.

3.1 Experimental Setup

3.1.1 Force Application System

To apply a force to the simulator a KUKA 7 axes light weight robot (LWR) (KUKA Robotics Canada, Mississauga, Ontario), as employed in the previous chapter, was used. The robot interfaced with the simulator using a surgical reamer with a 3D printed tip. The reamer was mounted to the robot using a custom clamp (shown in Figure 2.11).

As previously discussed, for this loading protocol the robot was actuated using force control to more accurately replicate clinically relevant loading scenarios. The robot was actuated relative to a tool-tip coordinate system (shown in Figure 3.1). This system had an origin at the tip of the reamer and three orthogonal axes. The axis defined as the Z_{ream} axis was aligned so that it was collinear with the reamer shaft and the x_{ream} and y_{ream} axes

were oriented orthogonal to the z_{ream} axis along the horizontal and vertical planes, respectively. When using force control, the robot needs to compensate for the weight of the clamp and reamer to be accurately controlled. Therefore, the center of gravity of the tool was calculated using the internal functions of the KUKA robot and used in the robot control programs.

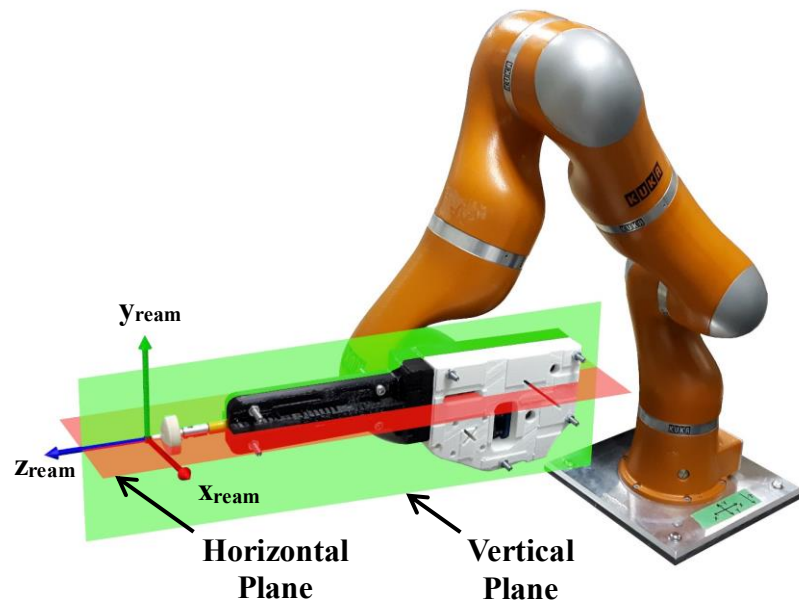


Figure 3.1: Reamer Tool-Tip Coordinate System

A tool-tip coordinate system was defined for the surgical reamer mounted to the KUKA LWR. All motions in the loading protocol are with respect to this coordinate system.

The robot was programmed to apply a load along the z_{ream} axis of the reamer while minimizing the reaction forces along the x_{ream} and y_{ream} axes. Similarly, a stiffness of 5000 N/m was prescribed to the translation along the z-axis and a zero stiffness was prescribed to translations along the x_{ream} and y_{ream} axes. By minimizing the force and prescribing a zero stiffness in the $x_{ream}y_{ream}$ plane, the robot translated freely within this plane to track with the motion of the base plate that occurred when a force was applied. Free motion within the $x_{ream}y_{ream}$ plane reduced the transverse loads applied at the tool tip

and resulted in a net force vector orientation that is collinear with the reamer shaft. A stiffnesses of 500 N/m was prescribed to rotations about all three axes. This rotational stiffness prevented the orientation of the reamer from changing with respect to the robot base throughout the loading protocol.

3.1.2 Force Recording Systems

Two systems were used to measure the force applied by the robot. The force-based reamer vector measurement system developed in Chapter 2 was used to record the net force applied using the calibration and error compensation algorithms. Secondly, an ATI Nano25 six degree-of-freedom (DOF) load cell (ATI Technologies, Markham, Ontario) was mounted to the front of the simulator using a custom mount as described in section 2.4 and shown in Figure 2.10. The mount was designed to align the measurement axes of the load cell with the force measurement axes of the reamer vector measurement system. The load cell was used as a comparator to determine the net force magnitude measurement accuracy of the reamer vector measurement system. The data acquisition system for the two force measurements is described in section 2.2.2 and shown in Figure 2.5.

3.1.3 Reamer Angle of Approach Tracking System

The reamer's angle of approach was measured by three systems. The reamer vector measurement system was used to record the reamer's angle of approach by applying the calibration and error compensation algorithms developed in Chapter 2. Secondly, the load cell was used to measure the reamer's angle of approach through the application of the assumption that the force vector is collinear with the reamer shaft. Finally, an NDI Optotrak Certus system (Northern Digital, Waterloo, Ontario) was used as a comparator to determine the accuracy of the angle of approach measurements given by the reamer vector measurement system and the load cell. For this protocol, two NDI smart markers (Northern Digital, Waterloo, Ontario) were used. One tracker was mounted onto the clamp holding the reamer to track the reamer and the second tracker was mounted to the load cell mount to track the movement of the load cell as shown in Figure 3.2.

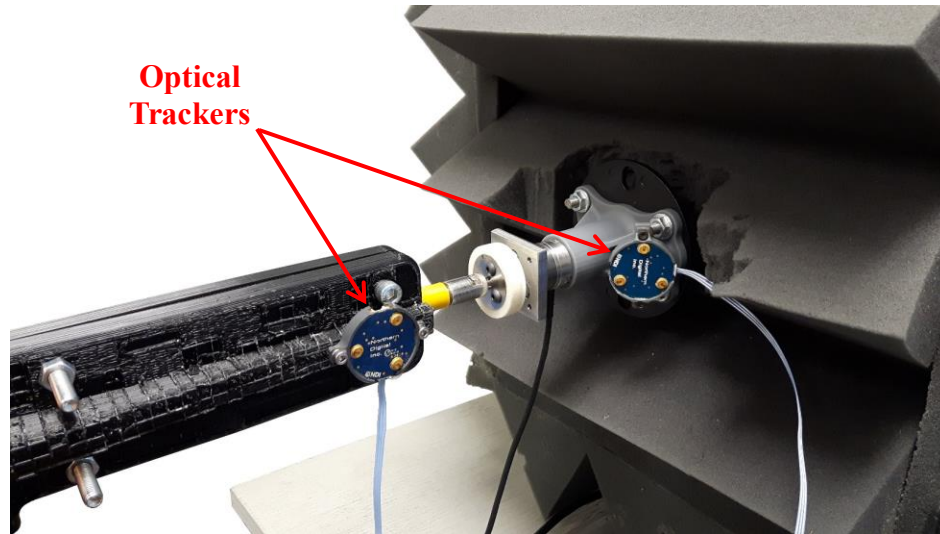


Figure 3.2: Optical Tracker Placement

Optical markers were mounted to the reamer clamp and the load cell mount to measure the reamer's angle of approach.

3.1.4 Optical Tracking Data Acquisition System

To collect the optical tracking data, the two markers were connected to an NDI wireless strober (Northern Digital, Waterloo, Ontario) which was connect to an NDI system control unit (Northern Digital, Waterloo, Ontario). The markers were tracked using an NDI Certus Optotrak camera (Northern Digital, Waterloo, Ontario) that was connect to the same control unit. Finally, The NDI system control unit was connected to a laptop via an ethernet cable. The data acquisition setup is depicted in Figure 3.3.

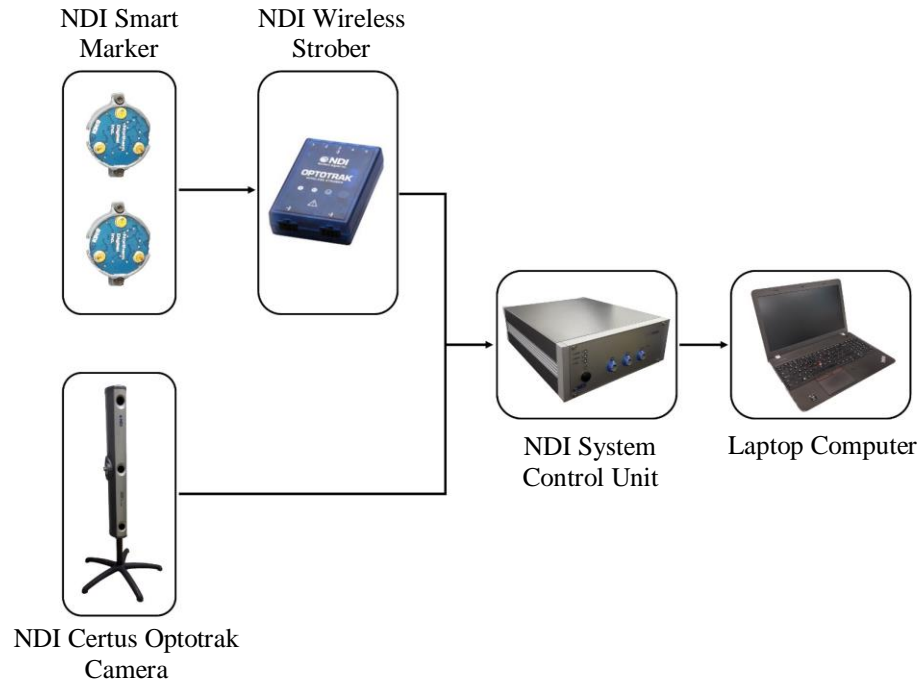


Figure 3.3: Optical Tracking Data Acquisition Setup

Two markers were used to track the position and orientation of the reamer and load cell. These trackers were connected to an NDI Wireless Strober which was connected to an NDI System Control Unit. The NDI Certus Optotrak camera was also connected into the System Control Unit which was connected to a laptop where all the optical data was collected using NDI First Principles software.

3.1.5 Optical Tracking Coordinate Systems

Using *NDI First Principles* (Northern Digital, Waterloo, Ontario), coordinate systems were constructed for the reamer and the load cell. Prior to digitizing points to construct the coordinate systems, the tool-tip coordinate system was aligned with the measurement axes of the load cell. To align the coordinate systems, a plate with the SI- and ML-axes of the load cell marked on it was mounted to the front of the load cell as shown in Figure 3.4. The reamer tip was moved to the point of intersection of the SI- and ML-axes and then actuated along the x and y axes of the tool-tip coordinate system. The reamer's orientation was adjusted until the reamer would closely trace with the SI- and ML- axes

when actuated along the x_{ream} and y_{ream} axes of the tool-tip coordinate system. Once aligned, the robot was taught the position using the KUKA “Touch-Up” function so that it could be recalled later.

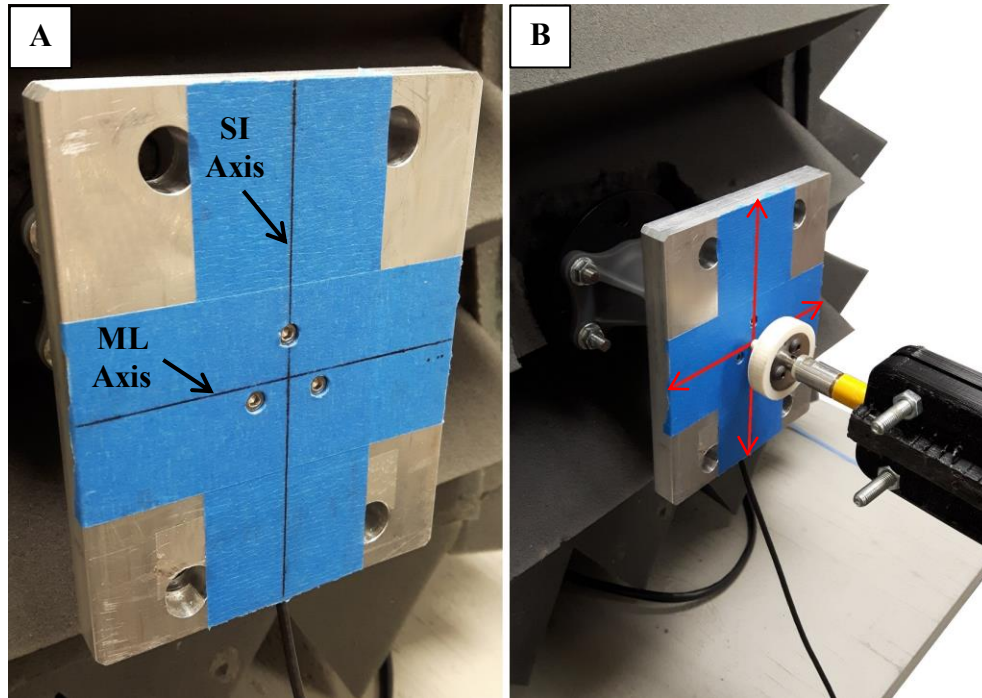


Figure 3.4: Robot and Load Cell Alignment

[A] A steel plate with the marked measurement axes of the load cell was mounted to the load cell. [B] The reamer tip was moved to the point of intersection of the load cell measurement axes. The orientation of the reamer was adjusted so that the reamer would trace the load cell axes marked on the steel plate when actuated along the x_{ream} and y_{ream} axes of the tool-tip coordinate axes (shown in red).

To construct the relevant coordinate systems, an optical stylus was used (shown in Figure 3.5A). A load cell coordinate system was constructed by digitizing the points shown in Figure 3.5B relative to the optical tracker mounted to the load cell mount. The intersection of the ML and SI axes defined the origin and points along the positive SI and ML axes were used to define the axis orientations. The plate was used to digitize the axes of the load cell because it allowed the axis orientations to be defined at a greater distance from the

load cell origin (this improved the accuracy of the digitizations). However, since the digitized points were on the face of the plate mounted to the load cell, the coordinate system was manually translated by the thickness of the plate along the ML axis to make the coordinate system coincident with the face of the load cell.

The reamer coordinate system was constructed by first digitizing the tip of the reamer with respect to the reamer optical tracker for the coordinate system origin. The reamer was then moved to the alignment position previously taught to the robot and the same points on the plate mounted to the load cell were used to define the axis orientations of the reamer (shown in Figure 3.5). For each loading experiment, the reamer position and orientation were tracked with respect to the load cell.

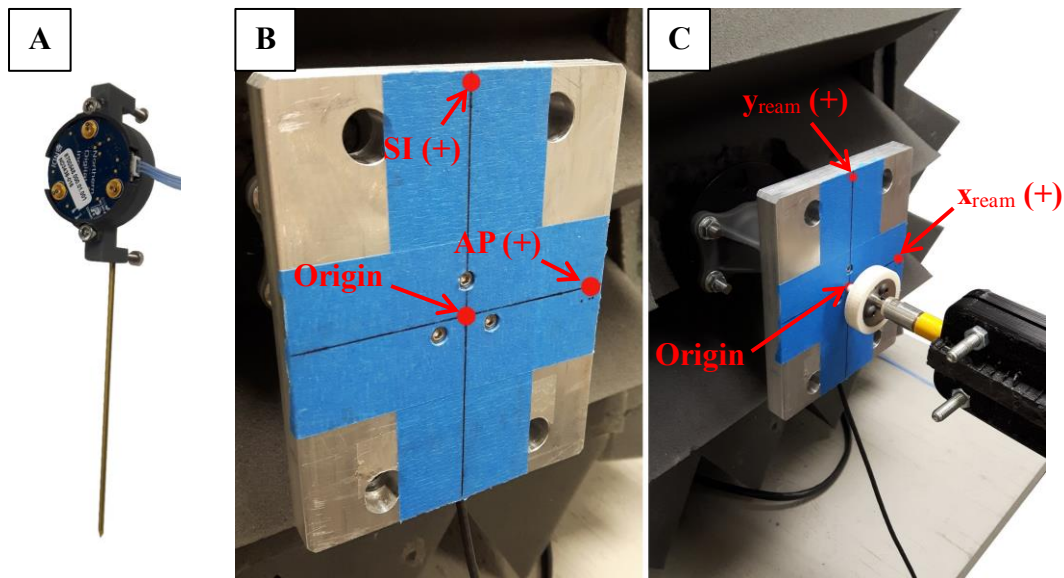


Figure 3.5: Digitization for Optical Tracker Coordinate System Construction

[A] An optical tracker stylus was used to digitize landmarks for coordinate system construction. [B] The three points shown were used to define the coordinate system for the load cell. After digitizing, the constructed coordinate system was manually translated so that it was coincident with the load cell. [C] The reamer tip was digitized to be used as the origin. The reamer was aligned with the load cell measurement axes and two points on the plate were used to define the axis orientations.

3.2 Loading Protocol

To quantify the errors of the system, the robot was used to apply a force at different reamer angles of approach. For each reamer orientation tested, force targets of 25, 50, 75 and 100 N were used. Reamer angles of approach were selected to span the measurement range of the force-based reamer vector measurement system. To determine the target version and inclination reamer angles, a polar coordinate system was used. In this system, the angle, γ , is the net angle between the neutral axis (ML axis) and the reamer shaft. Theta, θ , is the angle between the positive AP axis and the reamer shaft projected onto a sagittal plane (shown in Figure 3.6). In this system, version angle of approach was placed on the horizontal axis and inclination angle of approach was placed on the vertical axis. Reamer angles of approach targets were determined to have a net angle from the neutral axis, γ , in increments of 1.5 degrees spanning a range of zero to 13.5 degrees. The target orientations for each net angle, γ , were defined by projected angles on the sagittal plane, θ , in increments of 15 degrees spanning a range of zero to 345 degrees. Although the force-based measurement system was calibrated for angles from -15 to 15 degrees of version and inclination, a maximum net angle of 13.5 degrees was chosen because angles of 15 degrees caused the reamer tip to impinge in the pilot hole of the plate mounted to the front of the load cell. This presented a significant risk for potentially damaging the reamer tip so only angles of up to 13.5 degrees were chosen.

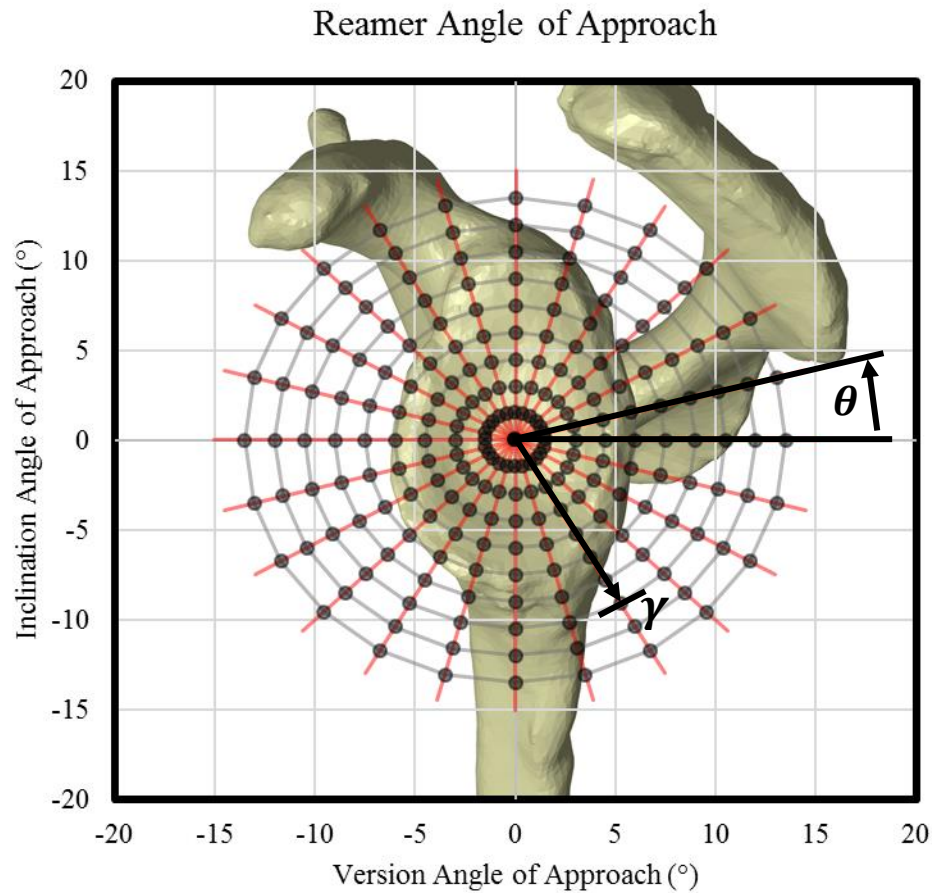


Figure 3.6: Reamer Angle of Approach Defined by a Polar Coordinate System

A polar coordinate system was used to define the target angles of approach for characterizing the system error. Each point represents a target version and inclination angle of approach (version and inclination angle plotted on the horizontal and vertical axes, respectively). The points were defined by a net angle of rotation from the ML axis (defined by angle, γ) and from the positive AP axis to the reamer shaft projected onto a sagittal plane (defined by, θ).

For each trial, the reamer was oriented with respect to the load cell using the live angle of approach readout from the NDI First Principles program. Once the desired orientation was achieved by manually actuating the robot, the reamer position and orientation was

taught to the robot to be used with the robot's control program. Then robot loading program was run, and five seconds of data was recorded from the force and angle of approach measurement systems once the robot had reached a steady-state. Angles and forces were averaged over five seconds. In total, this process was repeated for 217 angles of approach at four force magnitudes.

3.3 Force-Control Loading Repeatability

To test the repeatability of the force-controlled loading setup, a repeatability analysis was conducted using a smaller set of reamer orientations. The reamer orientations used were defined by net angles, γ , of 0, 4 and 8 and projected angles, θ , of 45 degree increments from 0 to 315 degrees (γ and θ defined in section 3.2). Measurements were taken 5 times for each orientation and SPSS was used to calculate an intraclass correlation coefficient (ICC) for each measured parameter using a two-way mixed model with absolute agreement. A summary of the ICCs presented in Table 3.1 show that the system reliability is regarded as excellent for all measures using single measure criteria [71]. This analysis indicates that the results for a single trail at each reamer orientation will reliably represent the accuracy of the reamer vector measurement system.

Table 3.1: Force Control Loading Repeatability Intraclass Correlation Coefficients

Measurand	Measured By:	Intraclass Correlation Coefficient
Version Angle	Reamer Vector Measurement System	0.994
	ATI Nano25 Load Cell	0.994
	Certus Optotrak	0.983
Inclination Angle	Reamer Vector Measurement System	0.978
	ATI Nano25 Load Cell	0.976
	Certus Optotrak	0.979
Net Force	Reamer Vector Measurement System	0.945
	ATI Nano25 Load Cell	0.949

3.4 Reamer Vector Measurement System Accuracy with Force-Control Loading

3.4.1 Coordinate System Alignment

Prior to examining the error of the force-based measurement system, the measurement systems axes were checked for alignment. To perform this, the reamer orientation measured by the optical tracking system was plotted with version angle on the horizontal axis and inclination angle on the vertical axis (Figure 3.7). The angle of approach measured via the load cell was included. The findings indicate that there was a constant orientation offset between the load cell and the optical system at all four target force magnitudes. To determine this offset, the average difference in version and inclination angle between the load cell and the Optotrak system for a neutral angle of approach (zero degrees of inclination and version) was calculated at all four target force magnitudes. The average offset for inclination angle was 5.03 ± 0.19 degrees and the average offset for version angle was 0.84 ± 0.19 degrees. To account for this misalignment, the angle offsets for version and inclination angle were subtracted from the load cell measured angles of approach. These offsets were also subtracted from the force-based reamer vector measurement system because the measurement axes of this system were calibrated so that they were aligned with the load cell. Therefore, the same offset was expected in the reamer vector measurement system.

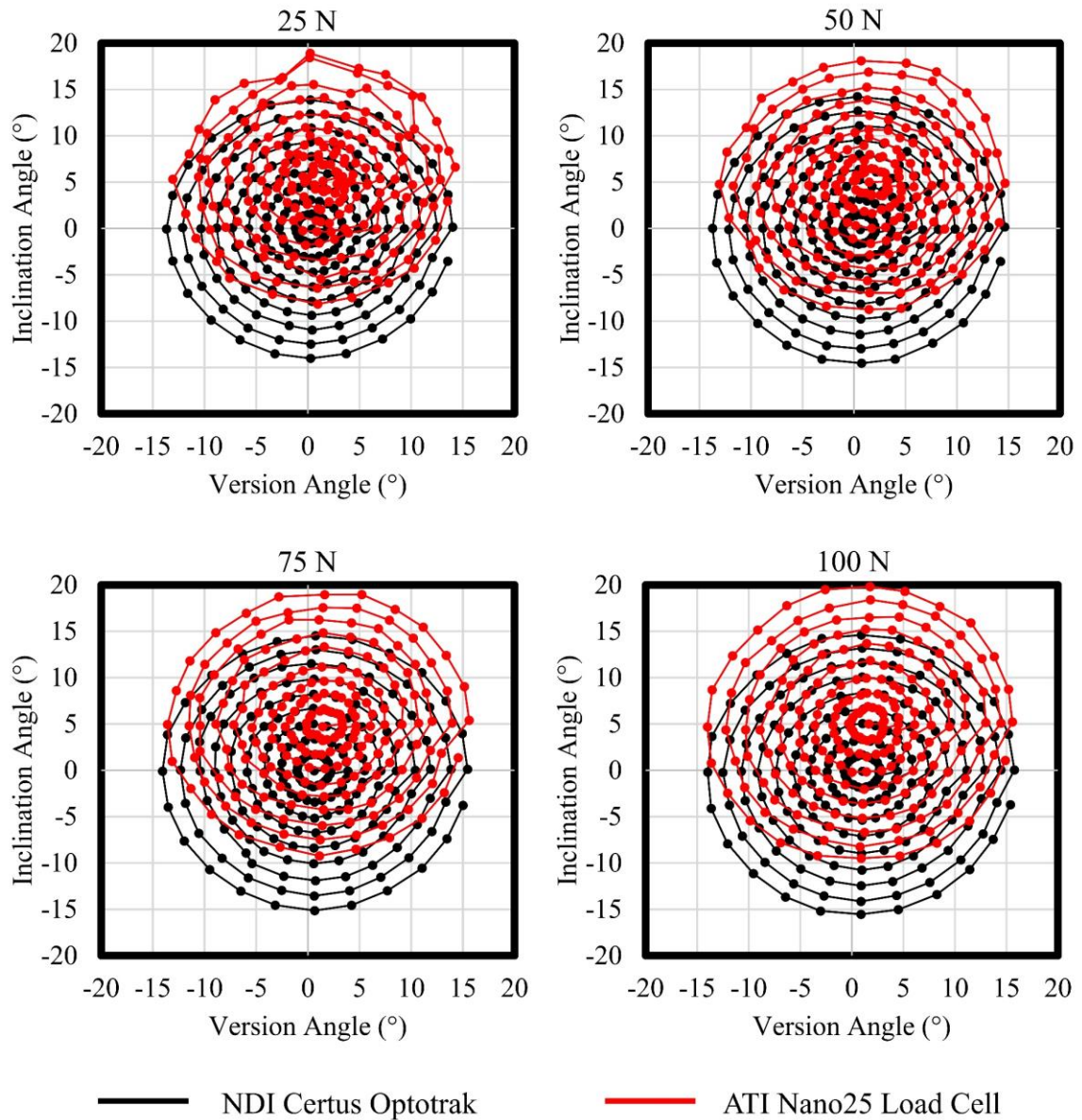


Figure 3.7: Certus Optotrak and ATI Nano25 Load Cell Coordinate System Alignment

The reamer angle of approach measured by the optical trackers and the commercial load cell were plotted on a scatter plot to determine the average axis orientation offset. The average offset for all target forces was determined and used to adjust the load cell and reamer vector measurement system angle measurements.

3.4.2 Version Angle of Approach Accuracy

To analyze the error in the version angle of approach measured by the reamer vector measurement system, the difference between the reamer vector measurement system and the optical system was examined for each reamer orientation at each force magnitude. The overall error averaged for all reamer orientations is shown in Table 3.2.

Table 3.2: Version Angle of Approach Overall Error – Reamer Vector Measurement System vs. Certus Optotrak

<i>Target Force</i>	<i>Mean Error (°)</i>	<i>Mean Absolute Error (°)</i>
25 N	0.0 ± 0.5	0.4 ± 0.3
50 N	0.0 ± 0.5	0.3 ± 0.3
75 N	-0.2 ± 0.5	0.4 ± 0.4
100 N	-0.5 ± 0.4	0.5 ± 0.4

These results show that there was a slight increase in the system errors when switching from a position-controlled approach (discussed in Chapter 2) to a force-control approach. To observe any trends that are present in the error, surface plots were generated. In these plots, the version and inclination angle of approach measured by the reamer vector measurement system were plotted as the two independent variables and the measurement error in degrees was plotted on the vertical axis. A plot for all four target force values is shown in Figure 3.8. There are trends in the error that become more apparent as the force increases but these are obscured at lower force magnitudes by an increased variability between orientations. The error increases negatively as version angle approaches extreme angles and there was an increase in error in the negative direction as inclination angle became more negative.

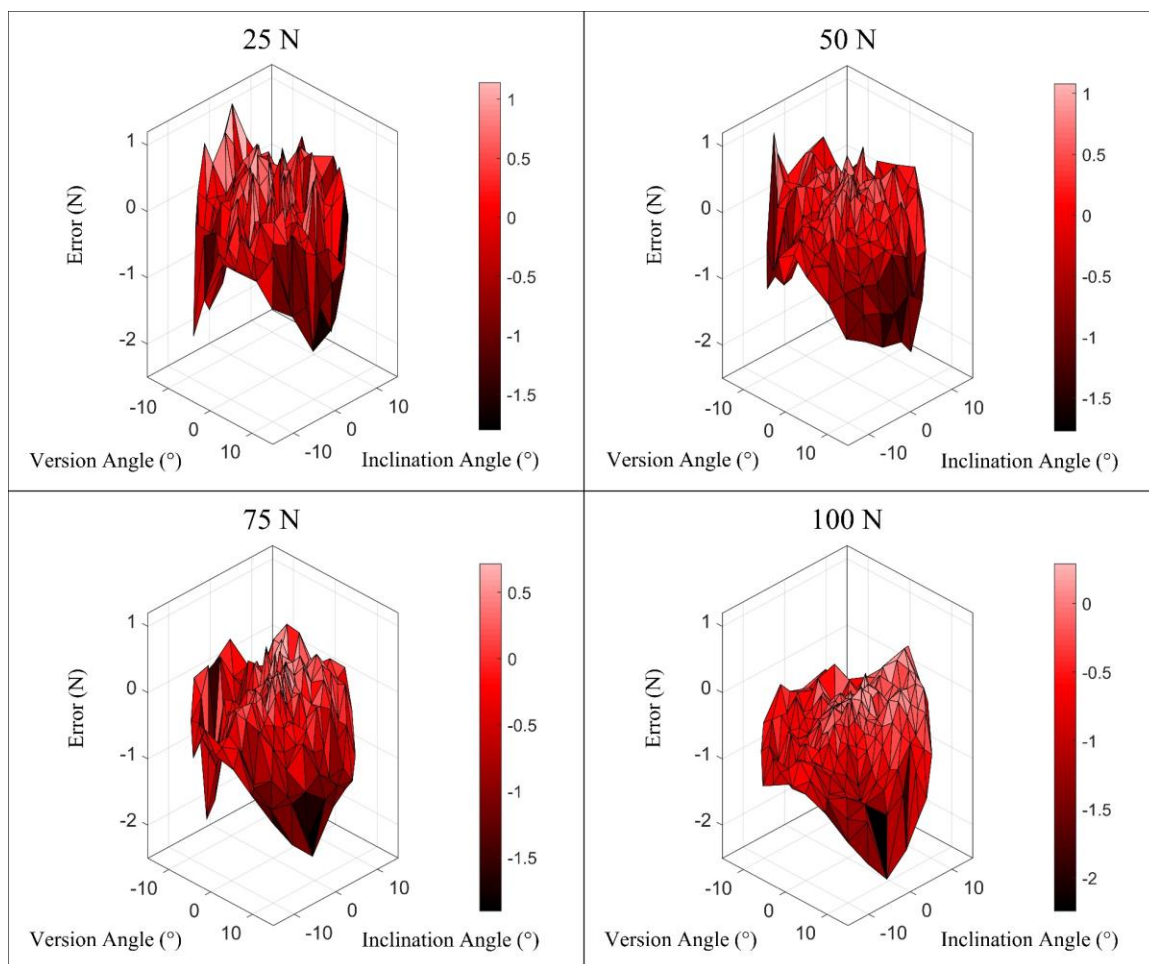


Figure 3.8: Version Angle of Approach Surface Plots – Reamer Vector Measurement System vs. Certus Optotrak

The error in the version angle of approach measurement from the force-based reamer vector measurement system was plotted as a surface plot. Version and inclination angles (measured by the reamer vector system) were plotted on the independent axes and the error in degrees was plotted on the dependent axis. Four plots were generated; one for each target force magnitude.

A repeated measures analysis of variance (ANOVA) was performed in SPSS to examine the effect of force magnitude on the error between the reamer vector measurement system and Optotrak. Results showed there was an effect of force on mean error ($P < 0.01$). There was a significant difference between all force magnitudes ($P < 0.05$) except between 25 N and 50 N force magnitudes ($P = 1.0$).

One source of error was revealed when comparing the version angle of approach measured by the load cell to the Optotrak system. Given the assumption that the force vector and reamer shaft are collinear, minimal errors between the load cell and the optical system would be expected. However, Table 3.3 shows that there were differences between these two systems. In addition, Figure 3.9 shows that the error trends found for the load cell were characteristically similar to the trend found for the reamer vector system (see Figure 3.8).

Table 3.3: Version Angle of Approach Overall Error – ATI Nano25 Load Cell vs. Certus Optotrak

<i>Target Force</i>	<i>Mean Error (°)</i>	<i>Mean Absolute Error (°)</i>
25 N	0.0 ± 0.5	0.4 ± 0.3
50 N	0.0 ± 0.4	0.3 ± 0.2
75 N	-0.2 ± 0.4	0.4 ± 0.3
100 N	-0.6 ± 0.3	0.6 ± 0.3

Since the load cell was used to calibrate the reamer vector measurement system, any differences that were present between the load cell and the optical system were also present between the reamer vector system and the optical system. The error that occurred between the load cell and optical system was believed to be a result of the limitations of the KUKA robot. Specifically, the robot was programmed with a zero stiffness in the $x_{ream}y_{ream}$ plane of the reamer to minimize the transverse load applied at the reamer tip. If any transverse load was applied, the assumption that the reamer angle of approach and the force vector are collinear lost its validity because the net force applied by the robot was not in-line with the reamer shaft. The robot was evidently not able to minimize the forces in the $x_{ream}y_{ream}$ plane to the degree required to meet the assumptions made. This was not unexpected given the common application for this robot. Typically, this robot is used in manufacturing and industrial environments where you would rarely find the need

to use force minimization to track with the movement of a component. In the context of manufacturing and other industrial applications, the errors that the robot caused would not be considered significant.

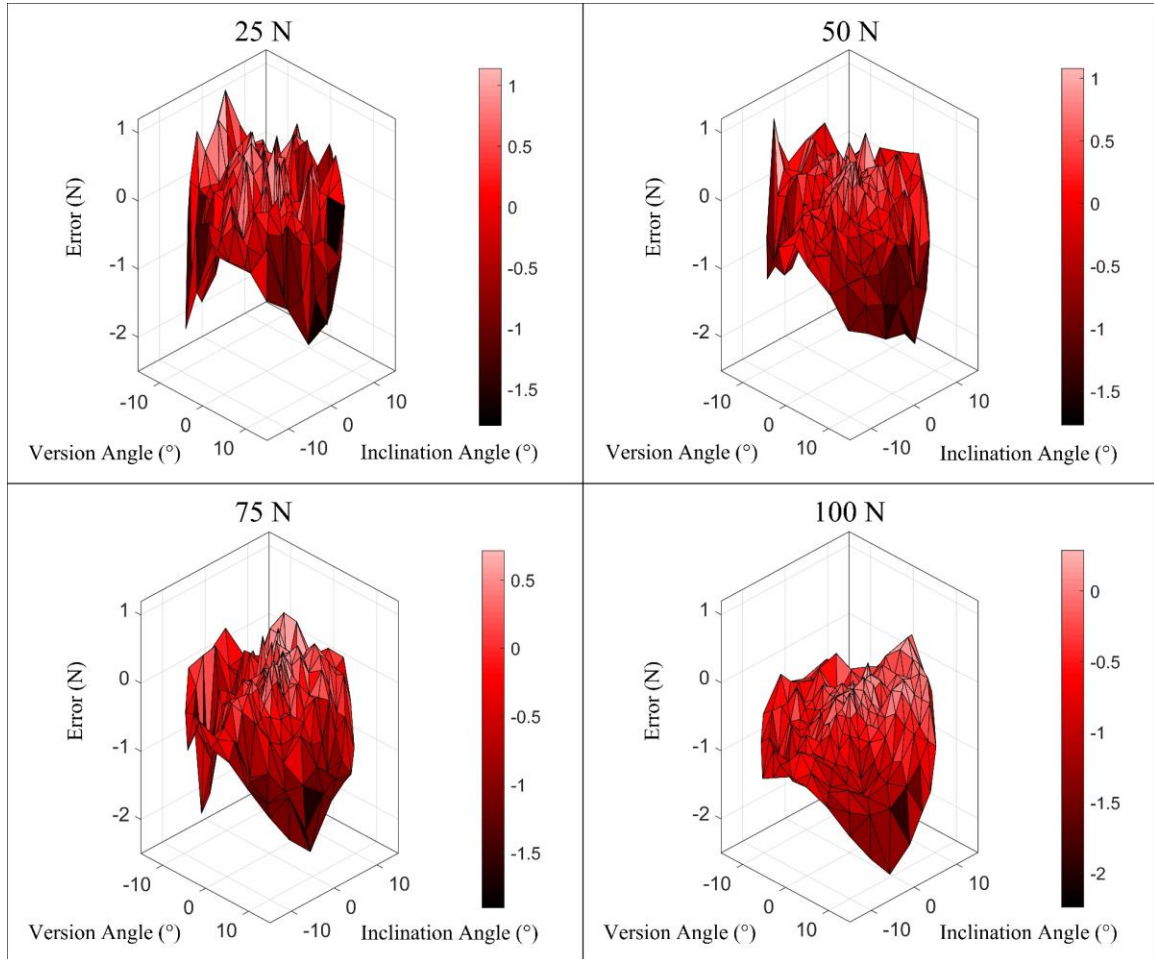


Figure 3.9: Version Angle of Approach Surface Plots – ATI Nano25 Load Cell vs. Certus Optotrak

The error in the version angle of approach measurement from the commercial load cell was plotted as a surface plot. Version and inclination angles (measured by the reamer vector system) were plotted on the independent axes and the error in degrees was plotted on the dependent axis. Four plots were generated; one for each target force magnitude.

A repeated measures ANOVA was performed in SPSS to examine the effect of force magnitude on the error between the load cell and Optotrak. Results showed there was an effect of force on mean error ($P < 0.01$). There was a significant difference between all force magnitudes ($P < 0.05$) except between 25 N and 50 N force magnitudes ($P = 1.0$).

To reveal a second source of error, the errors resulting from the transverse loads at the tool tip were subtracted from the reamer vector measurement system errors. Once removed, the resulting overall error was greatly reduced and there was less variability between adjacent orientations which made the trends in error more apparent (shown in Figure 3.10). The summary of errors can be seen in Table 3.4.

Table 3.4: Version Angle of Approach Overall Error – Reamer Vector Force Measurement System vs. Certus Optotrak minus Load Cell Errors

<i>Target Force</i>	<i>Mean Error (°)</i>	<i>Mean Absolute Error (°)</i>
25 N	0.0 ± 0.2	0.1 ± 0.1
50 N	0.0 ± 0.1	0.1 ± 0.1
75 N	0.0 ± 0.1	0.1 ± 0.1
100 N	0.1 ± 0.2	0.2 ± 0.1

Although the error was reduced, there was still more error present than when actuating the reamer in position control. This was believed to be caused by an induced moment at the reamer tip. For the development of the calibration and error compensation stages the reamer was kept at a neutral orientation with respect to the load cell coordinate system. This prevented the reamer tip from impinging in the pilot hole of the plate mounted to the front of the load cell. Once the reamer angle of approach was changed for the force-control protocol, the reamer tip began to impinge in the pilot hole. The impingement prevented angles above 13.5 degrees from being tested. When the reamer impinged it induced a moment at the reamer – load cell interface which introduced error into the

reamer vector system's measurements. With the tripod cantilever configuration, the reamer vector measurement system is not able to differentiate between axial loads and a moment applied to the simulator. Figure 3.10 shows that there was a negative increase in error as the version angle increased positively and a positive increase in error as version angle became more negative. This was expected because as the version angle became greater positively or negatively, the reamer tip impinged more in the pilot hole resulting in a greater induced moment and greater measurement error.

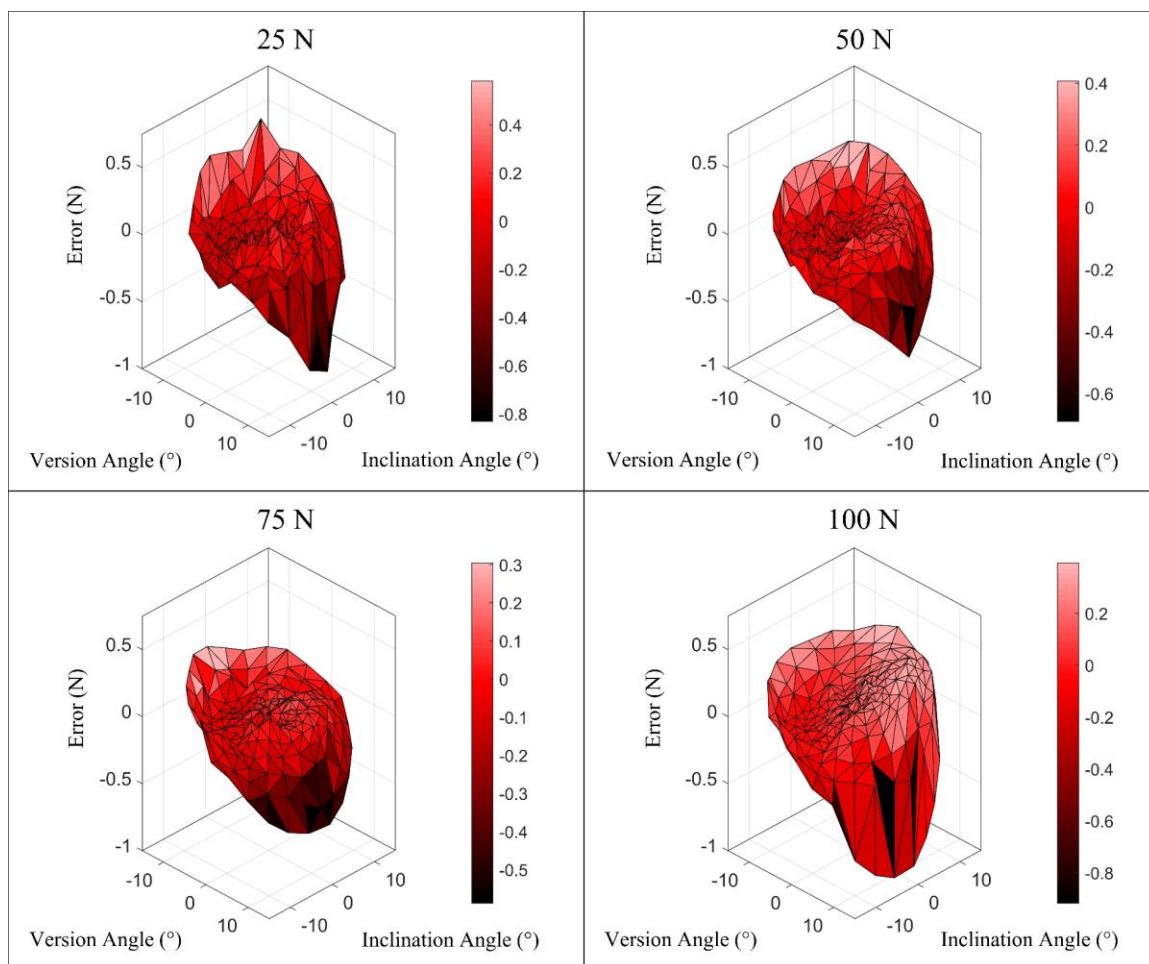


Figure 3.10: Version Angle of Approach Surface Plots – Reamer Vector Force Measurement System vs. Certus Optotrak minus Load Cell Errors

The error in the version angle of approach measurement from the force-based reamer vector measurement system minus the commercial load cell errors was plotted as a surface plot. Version and inclination angles (measured by the reamer vector system) were plotted on the independent axes and the error in degrees was plotted on the dependent axis. Four plots were generated; one for each target force magnitude.

A repeated measures ANOVA was performed in SPSS to examine the effect of force magnitude on the error between the reamer vector measurement system and Optotrak without the error from the load cell. Results showed there was an effect of force on mean error ($P < 0.01$). There was a significant difference between all force magnitudes ($P < 0.05$) except between 25 N and 75 N magnitudes ($P = 1.0$).

3.4.3 Inclination Angle of Approach Accuracy

The error in inclination angle of approach was examined in a similar way to version angle error. Firstly, inclination angle of approach error of the reamer vector measurement system compared to the optical system was examined for each reamer orientation at each force magnitude. The overall error averaged for all reamer orientations is shown in Table 3.5.

Table 3.5: Inclination Angle of Approach Overall Error – Reamer Vector Measurement System vs. Certus Optotrak

<i>Target Force</i>	<i>Mean Error (°)</i>	<i>Mean Absolute Error (°)</i>
25 N	-0.2 ± 0.8	0.6 ± 0.6
50 N	-0.6 ± 0.6	0.7 ± 0.5
75 N	-0.2 ± 0.6	0.5 ± 0.4
100 N	-0.1 ± 0.4	0.3 ± 0.3

Similar to the version angle of approach, there was an increase error when transitioning from a position-based control to a force-based control. The error appeared to be influenced by version and inclination angle measured by the reamer vector measurement system as shown by the surface plots in Figure 3.11. This figure shows that there were trends between error and inclination angle and there was an increase variability from what was seen in the error results from Chapter 2. Inclination angle error increased positively as inclination angle decreased and increased negatively as inclination angle increased. To better understand the sources of error, the error between the load cell and the optical system was examined.

A repeated measures ANOVA was performed in SPSS to examine the effect of force magnitude on the error between the reamer vector measurement system and Optotrak. Results showed there was an effect of force on mean error ($P < 0.01$). There was a

significant difference between all force magnitudes ($P < 0.05$) except between 25 N and 75 N ($P = 1.0$) and 25 N and 100 N ($P = 0.051$).

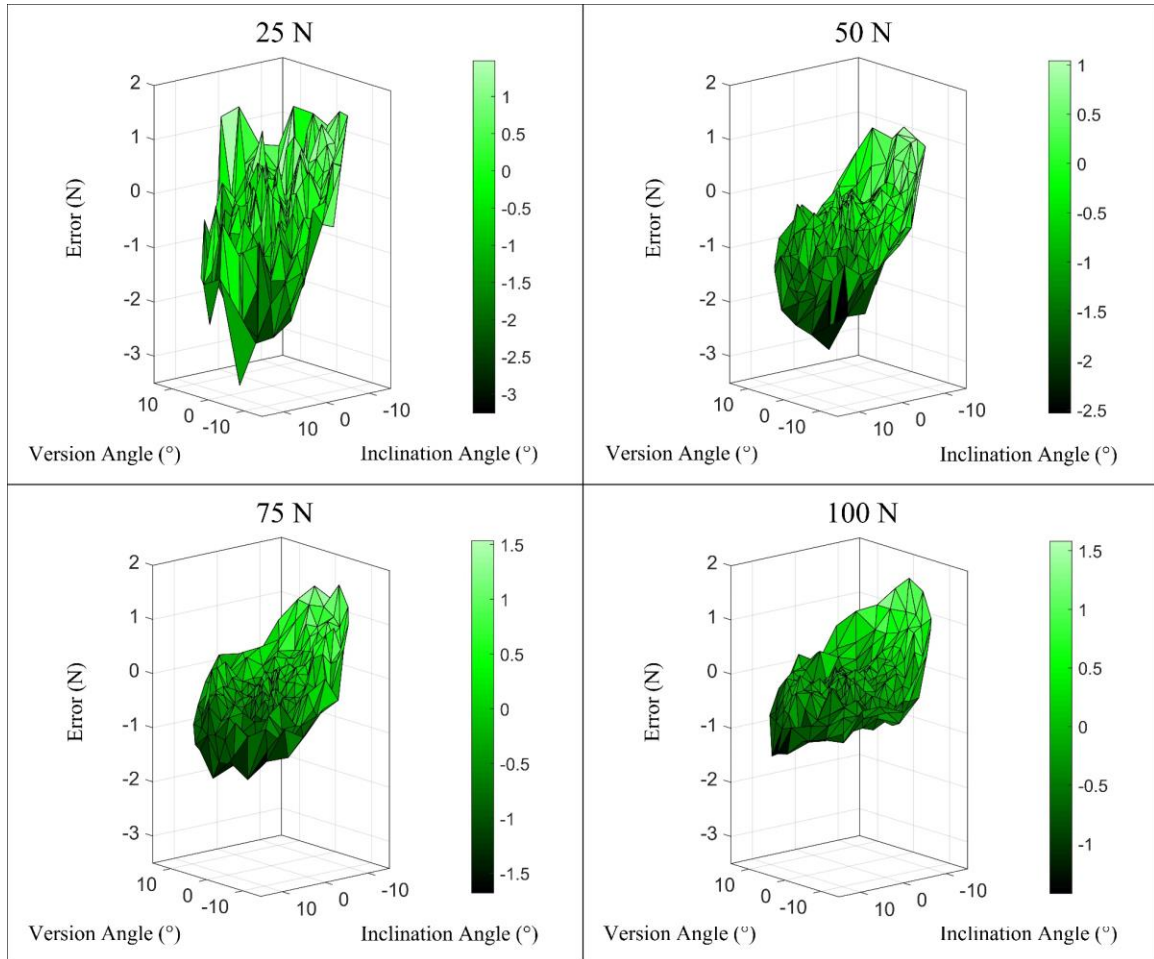


Figure 3.11: Inclination Angle of Approach Surface Plots – Reamer Vector Measurement System vs. Certus Optotrak

The error in the inclination angle of approach measurement from the force-based reamer vector measurement system was plotted as a surface plot. Version and inclination angles (measured by the reamer vector system) were plotted on the independent axes and the error in degrees was plotted on the dependent axis. Four plots were generated; one for each target force magnitude.

As discussed in section 3.4.2, the error between the load cell and the optical system would have been minimal if the assumption that the force vector and reamer shaft are collinear was valid. However, there were still differences present between these two systems. The errors at the four force target levels are summarized in Table 3.6. Figure 3.12 shows that the errors between the load cell and the optical system had similar trends to the error between the reamer vector measurement system and the Optotrak shown in Figure 3.11. These errors were caused by a transverse force applied at the reamer tip due to the limitations of the robot. The robot was limited in its ability to minimize the forces on the $x_{ream}y_{ream}$ plane of the reamer and therefore induced a transverse load at the reamer tip. This caused error in the reamer vector inclination angle of approach measurement.

Table 3.6: Inclination Angle of Approach Overall Error – ATI Nano25 Load Cell vs. Certus Optotrak

<i>Target Force</i>	<i>Mean Error (°)</i>	<i>Mean Absolute Error (°)</i>
25 N	0.2 ± 0.6	0.5 ± 0.4
50 N	-0.3 ± 0.5	0.4 ± 0.3
75 N	0.0 ± 0.4	0.3 ± 0.3
100 N	0.1 ± 0.3	0.2 ± 0.2

A repeated measures ANOVA was performed in SPSS to examine the effect of force magnitude on the error between the load cell and Optotrak. Results showed there was an effect of force on mean error ($P < 0.01$). There was a significant difference between all force magnitudes ($P < 0.05$) except between 75 N and 100 N ($P = 0.399$).

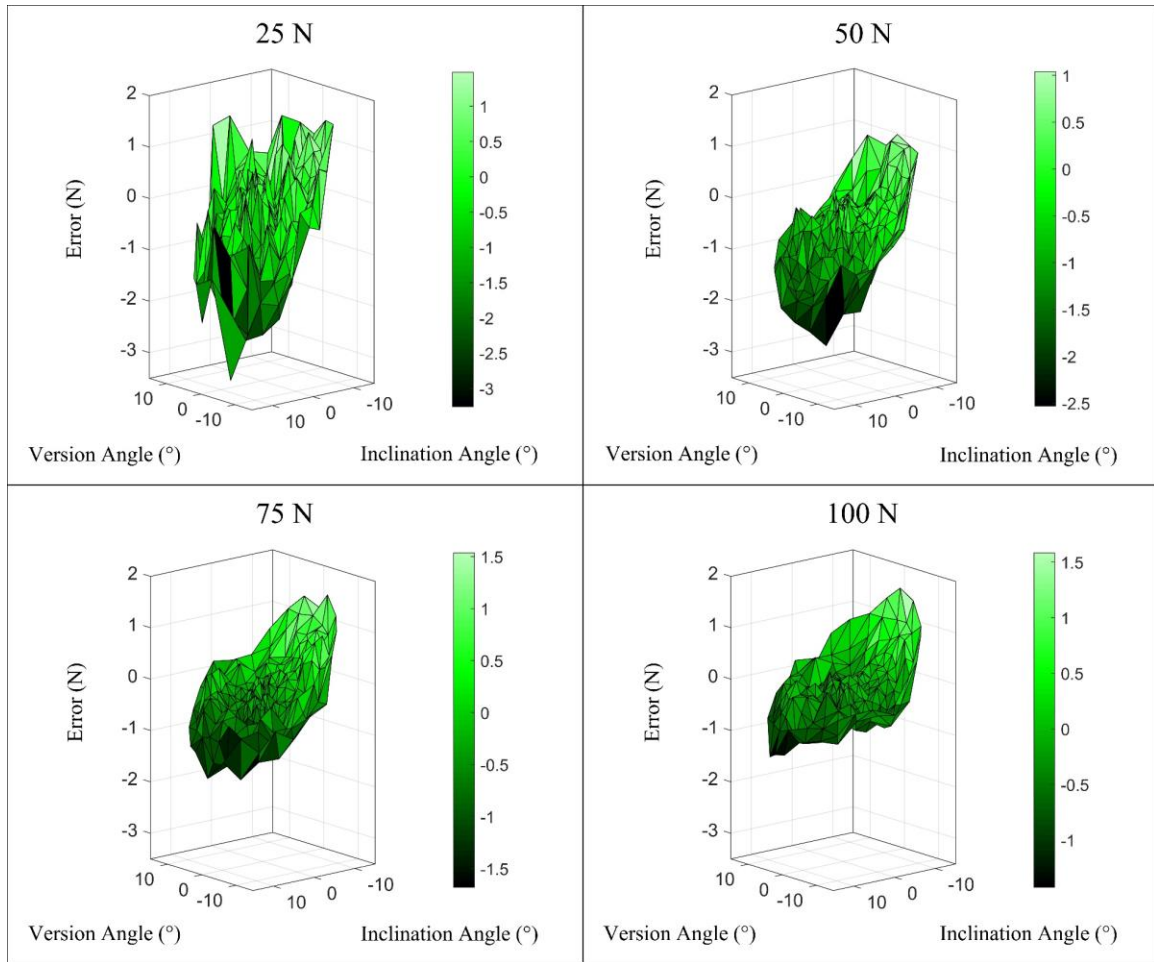


Figure 3.12: Inclination Angle of Approach Surface Plots – ATI Nano25 Load Cell vs. Certus Optotrak

The error in the inclination angle of approach measurement from the commercial load cell was plotted as a surface plot. Version and inclination angles (measured by the reamer vector system) were plotted on the independent axes and the error in degrees was plotted on the dependent axis. Four plots were generated; one for each target force magnitude.

When the errors resulting from the transverse loads was subtracted from the reamer vector measurement system errors, the error of the reamer vector force measurement system was moderately reduced but clearer error trends were revealed. The overall errors are summarized in Table 3.7.

Table 3.7: Inclination Angle of Approach Overall Error – Reamer Vector Force Measurement System vs. Certus Optotrak with Load Cell Errors Subtracted

<i>Target Force</i>	<i>Mean Error (°)</i>	<i>Mean Absolute Error (°)</i>
25 N	-0.5 ± 0.3	0.5 ± 0.2
50 N	-0.3 ± 0.2	0.3 ± 0.2
75 N	-0.3 ± 0.2	0.3 ± 0.2
100 N	-0.2 ± 0.3	0.3 ± 0.3

Figure 3.13 shows that there was an interaction between inclination angle and inclination angle error. As inclination angle increased there was a negative increase in error and as inclination angle decreased there was a positive increase in error. This is because an increase (positively or negatively) in inclination angle caused the reamer tip to impinge more in the pilot hole on the face of the load cell. This impingement induced a moment at the tool – load cell interface and increased the error of the reamer vector measurement system. This increased the error because the measurement system couldn't differentiate between axial loads and moments applied at the tool – load cell interface.

A repeated measures ANOVA was performed in SPSS to examine the effect of force magnitude on the error between the reamer vector measurement system and Optotrak with the load cell errors subtracted. Results showed there was an effect of force on mean error ($P < 0.01$). There was a significant difference between all force magnitudes ($P < 0.05$) except between 50 N and 75 N ($P = 0.377$).

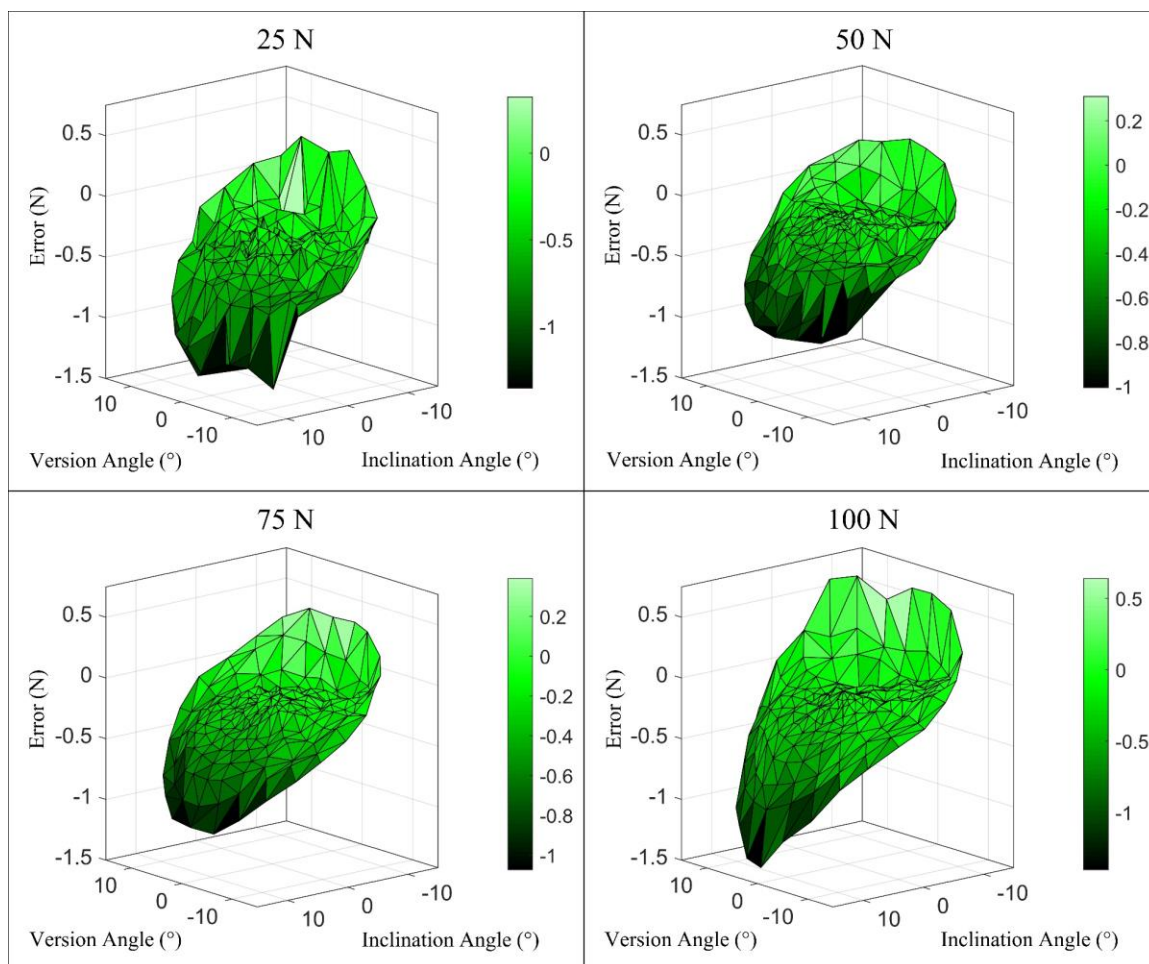


Figure 3.13: Inclination Angle of Approach Surface Plots – Reamer Vector Force Measurement System vs. Certus Optotrak with Load Cell Errors Subtracted

The error in the inclination angle of approach measurement from the force-based reamer vector measurement system while subtracting the commercial load cell errors was plotted as a surface plot. Version and inclination angles (measured by the reamer vector system) were plotted on the independent axes and the error in degrees was plotted on the dependent axis. Four plots were generated; one for each target force

3.4.4 Net Force Magnitude Accuracy

To determine the accuracy of the net force magnitude measurement the force measured by the reamer vector system was compared to the net force measured by the load cell. The average error of the system was calculated for each force magnitude across all reamer orientations and these errors are summarized in Table 3.8.

Table 3.8: Net Force Magnitude Overall Error – Reamer Vector Measurement System vs. ATI Nano25 Load Cell

<i>Target Force</i>	<i>Mean Error (N)</i>	<i>Mean Absolute Error (N)</i>
25 N	0.3 ± 0.1	0.3 ± 0.1
50 N	-0.2 ± 0.2	0.2 ± 0.1
75 N	-0.1 ± 0.3	0.2 ± 0.2
100 N	-0.6 ± 0.5	0.7 ± 0.3

These errors are slightly increased from the error results for the position-control protocol. Unlike the angle measurement, the net force magnitude measurement was not affected by the validity of the assumption that the reamer shaft is collinear with the force vector. However, it was affected by the reamer tip impingement in the pilot hole. When the reamer tip impinged in the pilot hole and induced a moment at the tool – load cell interface, there was an increase in the overall error of the system. This phenomenon is visualized in Figure 3.14. There appeared to be a very strong interaction between version angle of approach and net force error and a smaller but still visible interaction between inclination angle and net force magnitude error. This was expected because as the reamer deviated from a neutral angle of approach there was an increase in impingement resulting in a greater induced moment as discussed previously, and more measurement error. This error was also expected to increase with increasing force because a larger force applied induced a larger moment and increased the measurement error.

A repeated measures ANOVA was performed in SPSS to examine the effect of force magnitude on the error between the reamer vector measurement system and the load cell. Results showed there was an effect of force on mean error ($P < 0.01$). There was a significant difference between all force magnitudes ($P < 0.05$).

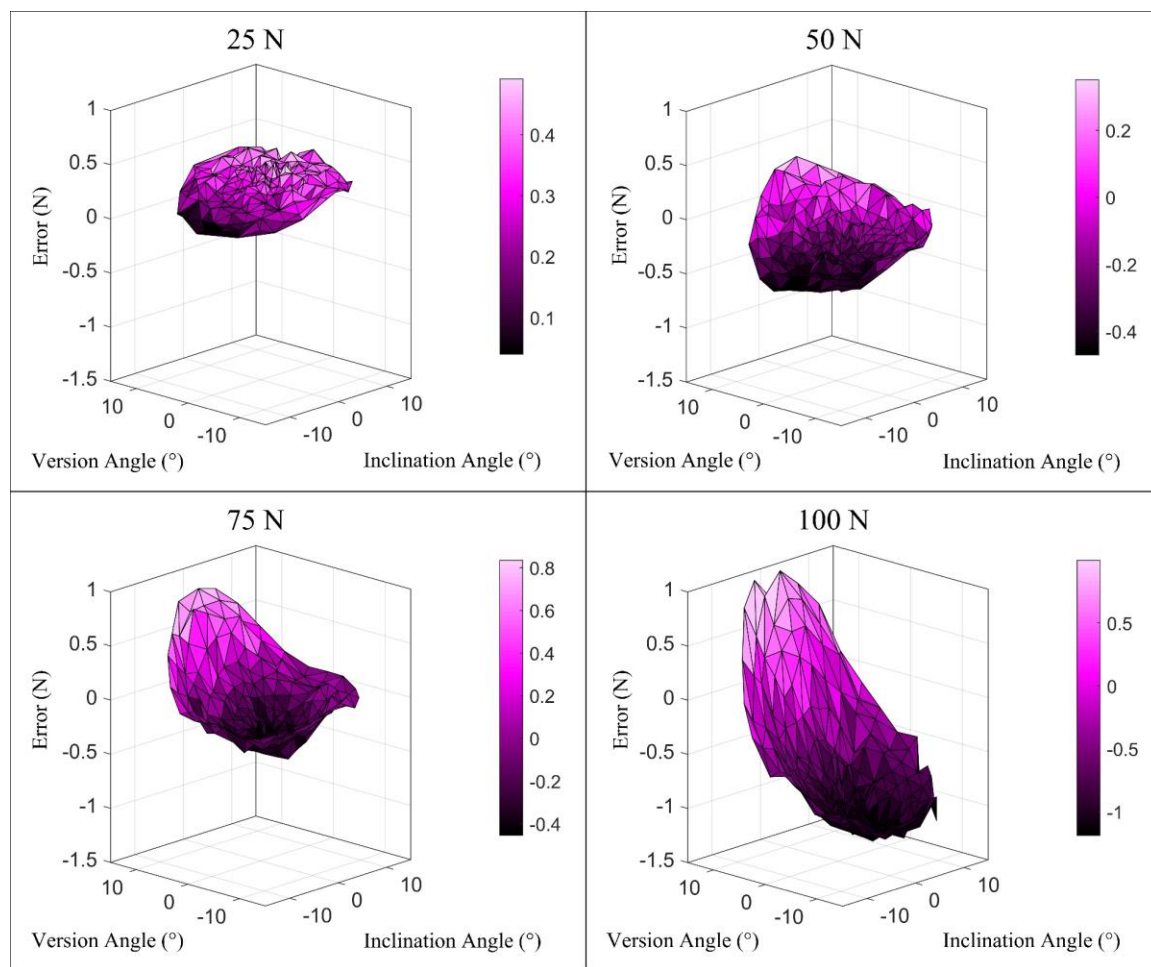


Figure 3.14: Net Force Magnitude Surface Plots – Reamer Vector Force Measurement System vs. ATI Nano25 Load Cell

The error in the net force magnitude measurement from the force-based reamer vector measurement system was plotted as a surface plot. Version and inclination angles (measured by the reamer vector system) were plotted on the independent axes and the error in Newtons was plotted on the dependent axis. Four plots were generated; one for each target force magnitude.

3.5 Summary

This chapter outlined the error characterization of the force-based reamer vector measurement system using a KUKA robot with more clinically relevant control methods.

The robot was used to apply loads to the simulator using a surgical reamer. The surgical reamer was mounted to the robot and a tool-tip coordinate system was defined for the reamer. The robot was programmed to apply a force to the simulator collinear with the reamer shaft with the reamer oriented in different angles of approach. The reamer's angle of approach was measured with the reamer vector force measurement system, the commercial load cell and an optical tracking system. The net force applied by the robot was measured by the reamer vector force measurement system and the commercial load cell.

Overall, there were increased errors in the reamer vector measurement system measurands when transitioning from position control to force control of the robot. Limitations of the KUKA robot increased the system error by applying a small transverse load at the tool tip. These transverse loads caused an increase in the error for angle of approach measurements. Secondly, errors were introduced from the reamer tip impinging in the pilot hole of the plate mounted to the load cell. This impingement induced a moment at the tool – load cell interface which the reamer vector measurement system was not able to account for. The induced moment introduced errors into the measurement of the reamer angle of approach measurements and the net force magnitude measurement.

Although the force-based loading protocol introduced more error into the reamer vector measurements, the increase in error was small. When considering force applied, studies have indicated that the typical “just” noticeable difference for forces applied during various movements is 5-10 percent of the force being applied [65] and that the ability to differentiate between force magnitudes decreases in the presence of low frequency haptic noise [66]. Errors less than 1 N are smaller than 5 percent of the force that a surgeon applies while reaming [61]. In addition, the reamer angle of approach errors are less than reported arm angle proprioception errors of 0.5 to 2.5 degrees [67]. Therefore, the errors of the system are sufficiently low to be used in reaming simulation studies.

Chapter 4

4 Haptic Glenoid Reaming Simulator for Shoulder Arthroplasty: Early Experience with Expert Surgeons

Overview: This chapter presents the use of the reaming vector measurement system to study a surgeon's ability to ream at a target angle of approach to correct glenoid retroversion.

Simulated CT images were generated to allow for a repeated measures approach and a 3D printed modular scapula was designed to accurately replicate glenoid anatomy. Comparisons are made between subjects' intended correction angle and the actual reamed angle and significant findings are discussed.

A previous study was conducted at our institution with fellowship-trained shoulder surgeons to evaluate the glenoid reaming simulator [61]. This study evaluated the efficacy of the vibration feedback produced by the simulator and examined the surgeons' ability to identify bone layers based on vibrational feedback. A uniaxial load cell was used to measure forces perpendicular to the glenoid surface; however, off-axis forces and reamer angle of approach were not able to be measured. With the incorporation of the reamer vector measurement system as described in the previous chapters, the study was conducted to evaluate the surgeons' ability to ream at a target angle of approach according to a pre-operative plan with the goal to correct glenoid retroversion.

4.1 Generating Simulated Computed Tomography DICOM Images for Pre-Operative Templating

To develop a pre-operative plan, the participants were required to measure glenoid retroversion from computed tomography (CT) images. The aim of this study was to analyze a surgeon's ability to correct glenoid retroversion according to a pre-operative plan. It was important to present the surgeons with number of operative cases that were nearly identical except for a change in glenoid version. If CT images from multiple sources were used, then there would be many changing factors between images that could influence the pre-operative templating and the glenoid reaming. To remove the effect of

multiple changing factors, a multi-slice CT was taken from one cadaveric specimen with a near neutral glenoid version (0.4 degrees anteversion). Within the CT stack, the glenoid version was altered to create multiple operative cases, each with different degrees of glenoid retroversion. By altering only the glenoid version within the image, all other parameters remained constant between cases.

To modify the CT images, the CT DICOM file was imported into Mimics software and the scapula was segmented from each slice. A mask was overlaid onto the segmented scapula and was used to generate a 3D scapular model as shown in Figure 4.1.

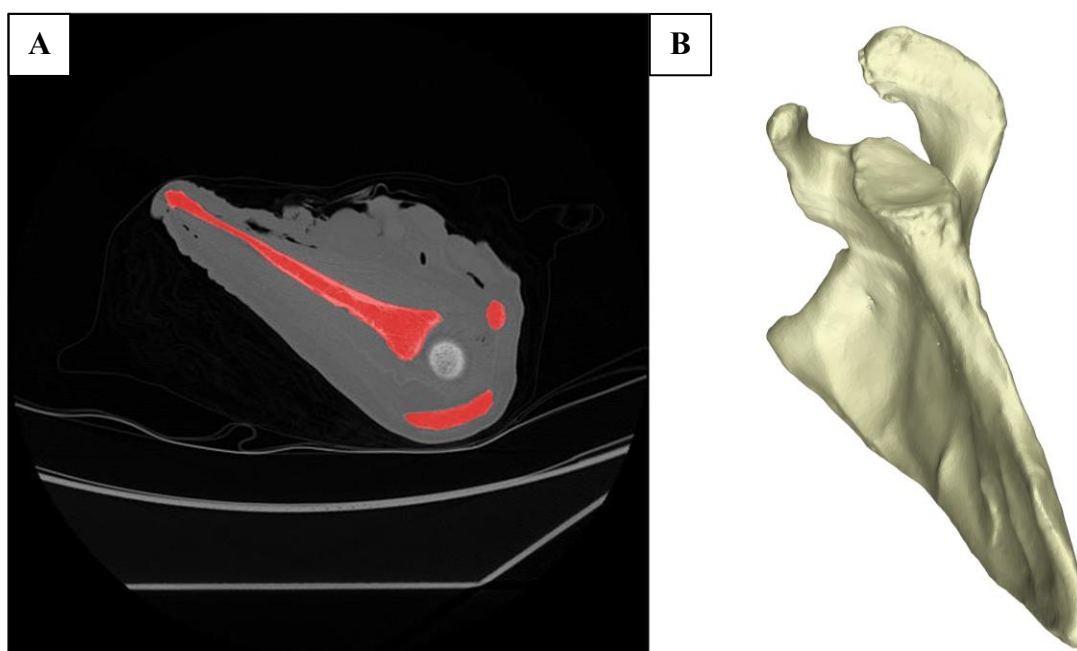


Figure 4.1: CT Scapula Segmentation and 3D Model Generation

[A] A sample DICOM slice shows the segmented scapula overlaid by a mask (red).

[B] The scapula mask was used to generate a 3D model of the scapula.

The position of each voxel that was overlaid by the scapula mask was exported from Mimics and the 3D model was exported as a stereolithography (STL) file. The exported STL file was imported into SOLIDWORKS where the glenoid version was altered. Within SOLIDWORKS, the scapular plane and neutral inclination axis were defined as described in section 2.1.1 and a neutral plane (zero degrees of version and inclination)

was defined as the plane normal to the neutral inclination axis. The neutral plane was placed near the base of the glenoid vault (shown in Figure 4.2A) and was used as the cut plane to remove the glenoid from the scapula. An additional cut plane was oriented orthogonal to the neutral plane near the base of the coracoid process (shown in Figure 4.2B).

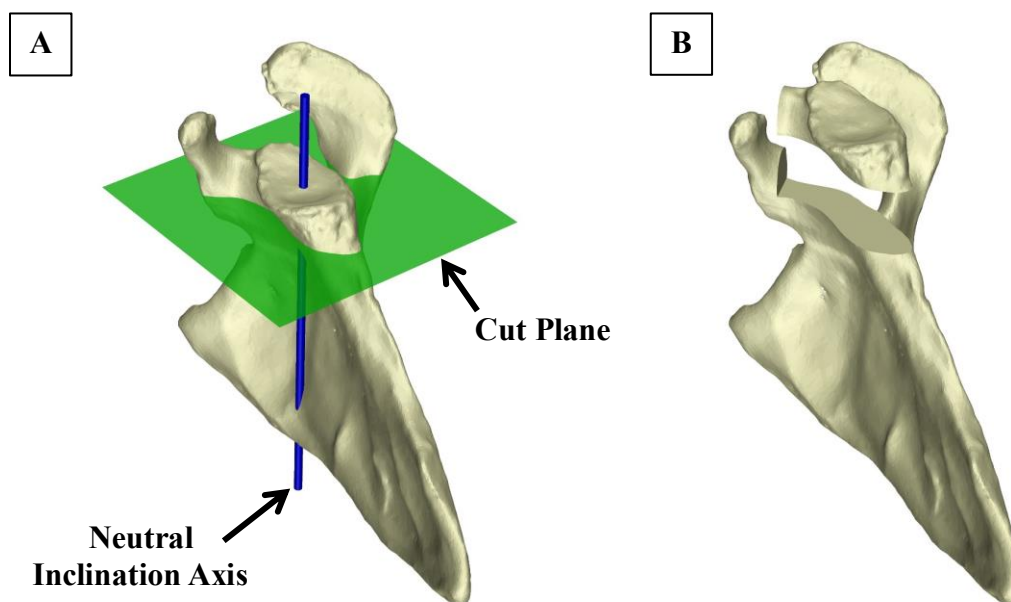


Figure 4.2: Sectioning the Glenoid From the 3D Scapula Model

[A] A cut plane was placed near the base of the glenoid vault. The cut plane was normal the inclination axis and represented zero degrees of glenoid version and inclination. [B] The glenoid was sectioned from the scapula. An additional cut plane was placed at the base of the coracoid so that the coracoid was not removed with the glenoid.

Once the glenoid was removed from the scapula, the glenoid version angle was altered by adding and removing bone material in specific regions to the backside of the glenoid. To ensure the addition and subtraction of material would only result in a change in glenoid version and would not affect glenoid inclination, a version axis was defined as the intersection between the neutral plane and the scapular plane. As shown in Figure 4.3, a

wedge of material was added anterior to the version axis and a second wedge of material was removed posterior to the version axis. By adjusting the wedge angle, the glenoid version angle was easily controlled. Once the glenoid model was altered it was reattached to the native scapula 3D model.

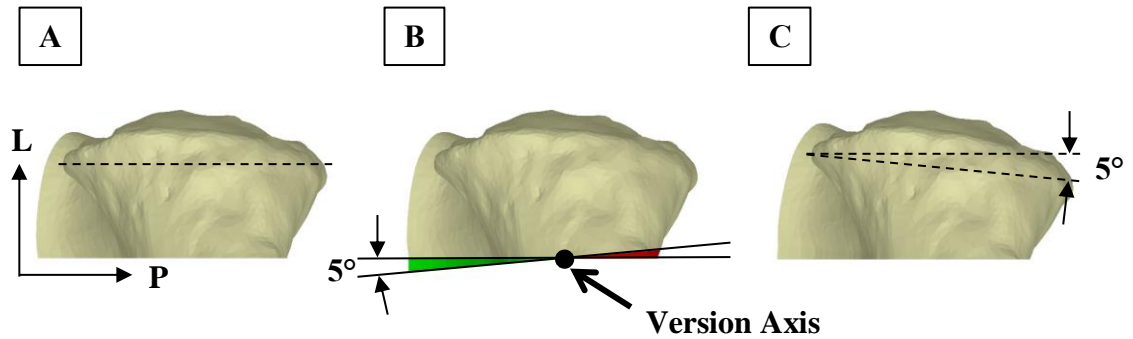


Figure 4.3: Glenoid Version Alteration

[A] Shows the native glenoid geometry. The native glenoid had a near neutral glenoid version (0.4 degrees anteversion). Axes show the posterior (P) and lateral (L) direction [B] A wedge of material was added anterior to the version axis (green) and a wedge of material was removed posterior to the version axis (red). This image shows the glenoid orientation being altered by 5 degrees. [C] The altered glenoid is 5 degrees more retroverted than the native glenoid.

The 3D modified scapula model was exported from SOLIDWORKS as an STL file and imported into Geomagic software. Within Geomagic, a smoothing tool was used to smooth the joining edges between the scapula and the modified glenoid.

The final modified scapula was imported back into Mimics and aligned with the image coordinate system by aligning the imported altered scapula 3D model with the native 3D scapula model that was previously generated from the native scapula mask. Once aligned, the altered scapula model was sliced to create a mask that was overlaid onto the CT image slices (sample shown in Figure 4.4). The position of each voxel overlaid by the altered scapula mask was exported from Mimics. This position data defined the location and orientation of the altered scapula within each CT slice.

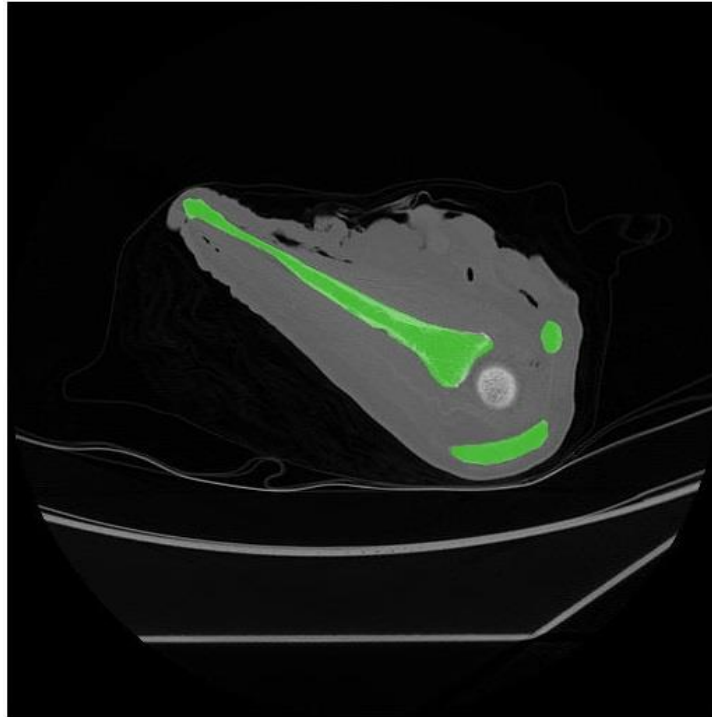


Figure 4.4: Altered Scapular Mask Overlaid onto CT Slices

This figure shows a CT slice overlaid by a mask generated from the 3D model of the altered scapula (green).

To replace the native scapula in the CT image with the modified scapula, the DICOM stack and the voxel position information from the altered and native scapular masks were imported into MATLAB. The modified scapula mask was reconstructed and overlaid onto the CT slices. As shown in Figure 4.5, the native scapula was removed by dilating the modified scapula mask and assigning a minimum brightness value of -1024 Hounsfield units (HU) (minimum determined by the smallest value output by a typical 12-bit scanner) to the voxels overlaid by the dilated mask.

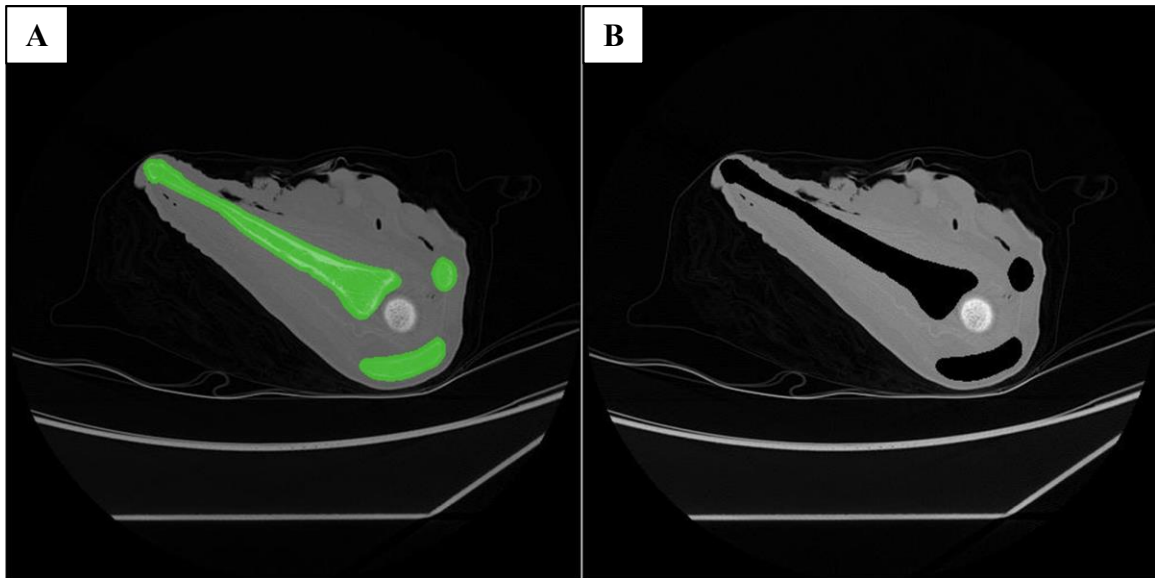


Figure 4.5: DICOM Native Scapula Removal

[A] The altered scapula mask was dilated to ensure that the native scapula was completely covered by the mask (mask shown in green). [B] The voxels overlaid by the mask were assigned a minimum brightness value of -1024 HU.

Using a dilated mask to remove the native scapula resulted in negative space forming around the modified scapula geometry (shown in Figure 4.6) To remove this, the negative space was assigned brightness values consistent with the surrounding soft tissue (shown in Figure 4.6). Noise was added to the simulated soft tissue voxels to introduce variability that was consistent with the surrounding native soft tissue.

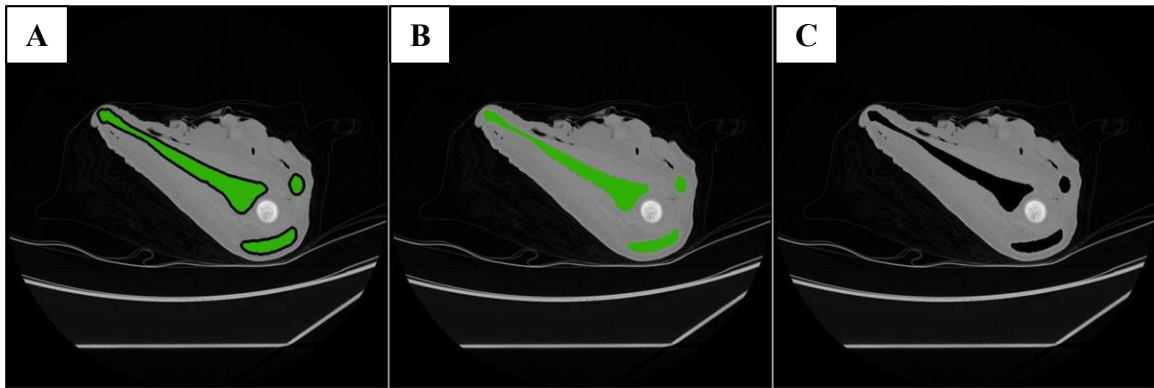


Figure 4.6: DICOM Soft Tissue Fill

[A] The scapula removal resulted in a negative space in the soft tissue surrounding the altered scapula mask (mask shown in green). [B] The negative space was filled using the brightness values of the surrounding soft tissue. [C] The altered scapula geometry outline appeared in the image once the mask was removed.

The final stage was to construct the trabecular bone and cortical boundary for the modified scapular geometry. To construct the trabecular bone, the trabecular bone from the native scapula was segmented from the original DICOM image by eroding the native scapula mask until the cortical bone was exposed. Brightness values of -1024 HU were assigned to the voxels not overlaid by the mask (sample slice shown in Figure 4.7).

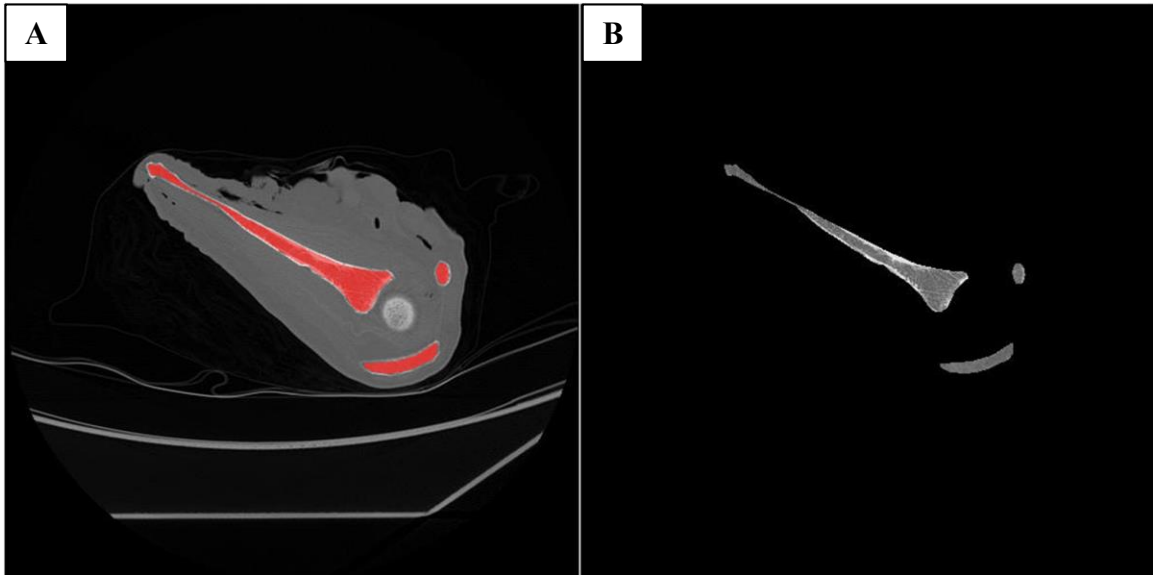


Figure 4.7: DICOM Trabecular Bone Segmentation

[A] The native scapula mask was eroded to expose the cortical bone layer of the scapula on each slice (mask shown in red). [B] The portion of the image not covered by the mask was removed. The majority of what remained was the trabecular bone.

Lastly, a simulated cortical boundary was added to the image and the extracted trabecular bone was inserted (shown in Figure 4.8). In each slice, the scapula was lightly blurred to blend the boundary between the cortical bone and the trabecular bone.

Simulated multi-slice CT images were made using the described procedure for the native glenoid geometry (0.4 degrees anteversion) and for glenoid geometries that were 2.5, 5.0, and 7.5 degrees more retroverted than the native geometry.

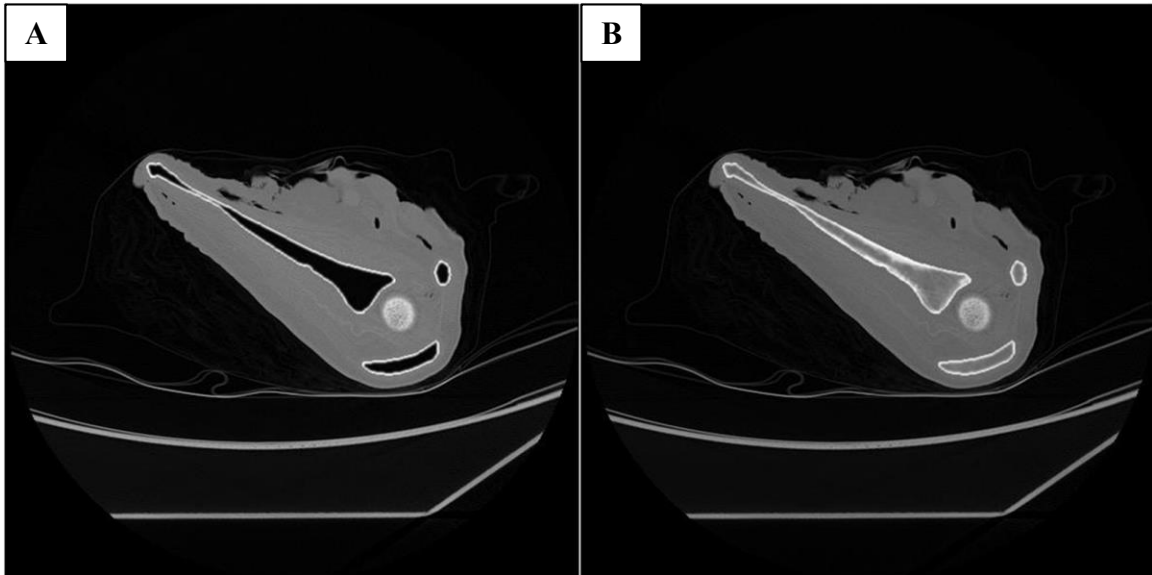


Figure 4.8: Final Altered DICOM Image

[A] A cortical boundary was added to the image in each slice. [B] The extracted trabecular bone was added to the image and the scapula was lightly blurred to blend the interface between the trabecular bone and cortical bone.

4.2 Modular Shoulder Model Design

To accurately reproduce the scapular anatomy from the simulated CT images, a modular shoulder model was designed and mounted to the simulator. This model consisted of a scapular component, a glenoid component and a soft tissue component. In the DICOM images, the scapula geometry was identical between cases except for the glenoid geometry. Therefore, a scapula model was designed with a modular glenoid component that could be changed to easily replicate the different glenoid geometries found in the CT images.

To make the scapular component, a 3D model of the scapula was segmented from the native scapula CT image. The glenoid was sectioned from the scapula using the neutral cut plane described in section 1.1. The medial side of the scapula was truncated, and a volume was extruded on the medial side to allow the model to be mounted to the simulator base plate and interface with a soft tissue component (as shown in Figure 4.9).

The base plate mount was oriented such that the face was parallel to the neutral plane of the scapula. Slots were added to serve as guides for the alignment fins added to the glenoid component (described later). Holes were cut into the model to incorporate standard fasteners that fixed the glenoid component to the scapular component.

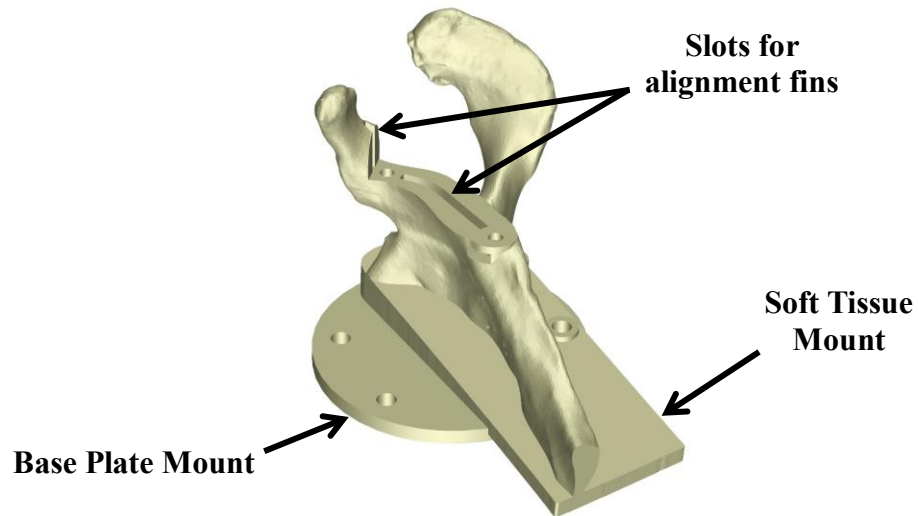


Figure 4.9: Shoulder Model Scapular Component

A scapular component was 3D printed and mounted to the front of the simulator as part of the modular scapula model.

The glenoid component was made by adding a pilot hole for the reamer and relevant holes for fasteners to the sectioned glenoid. Fins were added to allow for easy alignment with the scapula component (shown in Figure 4.10). A glenoid component was made for each version angle studied.

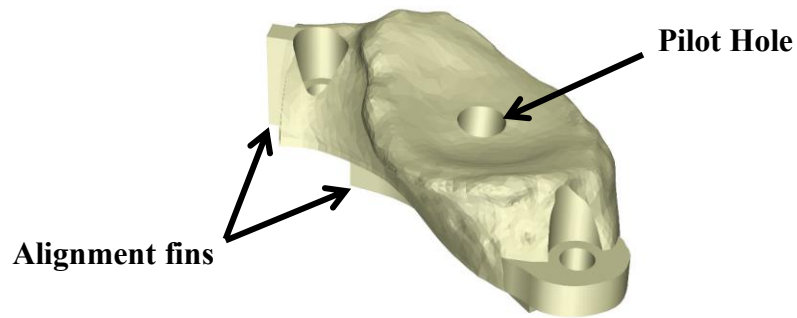


Figure 4.10: Shoulder Model Glenoid Component

A glenoid component was 3D printed and mounted onto the scapular component as part of the modular scapula model.

Both the scapular component and the glenoid component were 3D printed and mounted to the base plate of the simulator. The 3D printed assembly is shown in Figure 4.11.

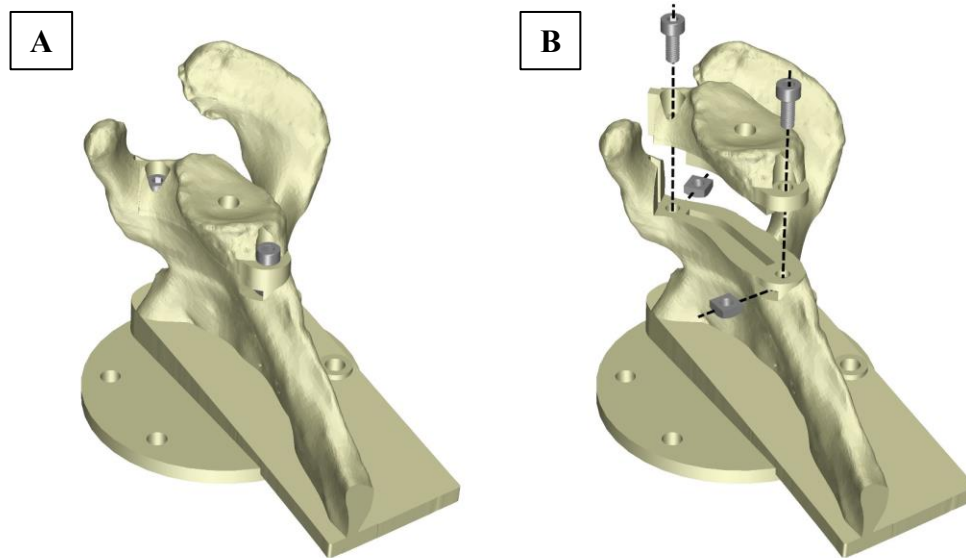


Figure 4.11: Shoulder Model 3D Printed Component Assembly

[A] Shows the scapula and glenoid 3D printed components assembly with included fasteners [B] Shows an exploded view of the assembly.

A soft shoulder model with an anterior approach incision was mounted onto the 3D printed components. Two surgical retractors were used to retract the soft tissue and allow access to the glenoid (shown in Figure 4.12).

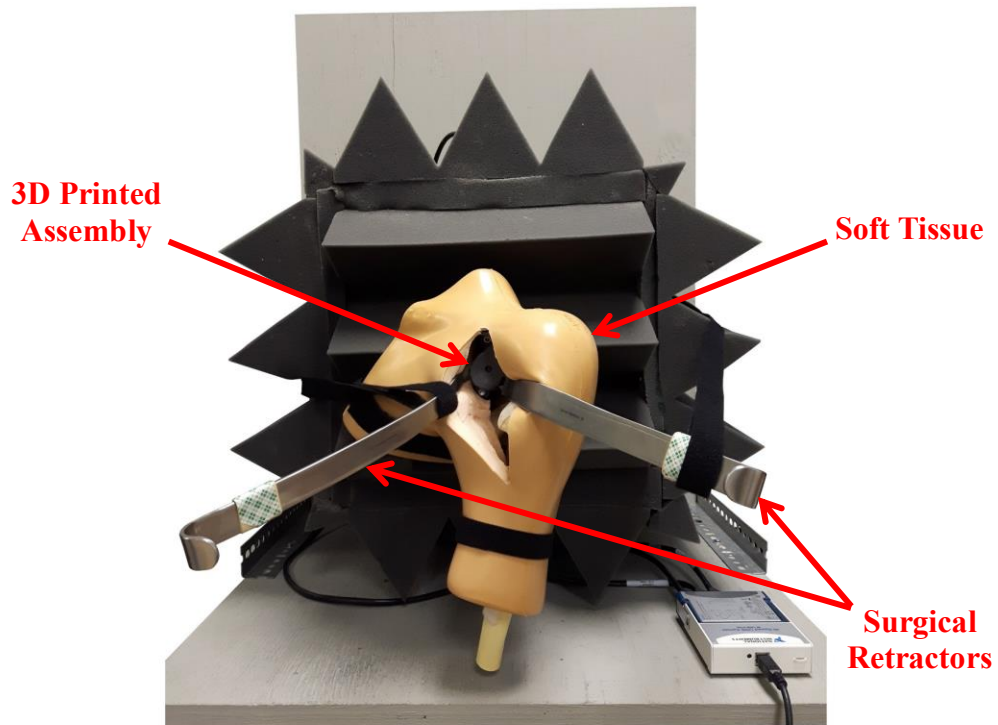


Figure 4.12: Reaming Simulator 3D Printed Glenoid and Soft Shoulder Model

A 3D printed glenoid and soft shoulder model was mounted to the glenoid reaming simulator. An anterior incision was made in the soft shoulder model and two surgical retractors were used to provide access to the glenoid.

4.3 Study Protocol

In this study, each surgeon used the system's pneumatic reamer to interact with the modular shoulder model mounted to the simulator. A graphical interface was shown to each subject that communicated necessary information to the subject for each reaming stage of the protocol.

Prior to assessment, each surgeon was given three minutes to familiarize themselves with the simulator by reaming on the native glenoid orientation 3D printed component. As the subject reamed, a looped vibration sequence consisting of subchondral and cancellous bone was played. The vibration sequence used was randomly selected for each subject from the simulator's available vibration profiles. By default, the sequence would repeat continuously as the subject reamed; however, upon the subject's request the sequence could be restarted at any point within the three-minute timeframe. While reaming, a progression bar indicated the layer being reamed and the relative depth of ream within the layer (shown in Figure 4.13). The graphical interface also showed the current time spent familiarizing with the system and a red/green light indicated when to begin and stop reaming.

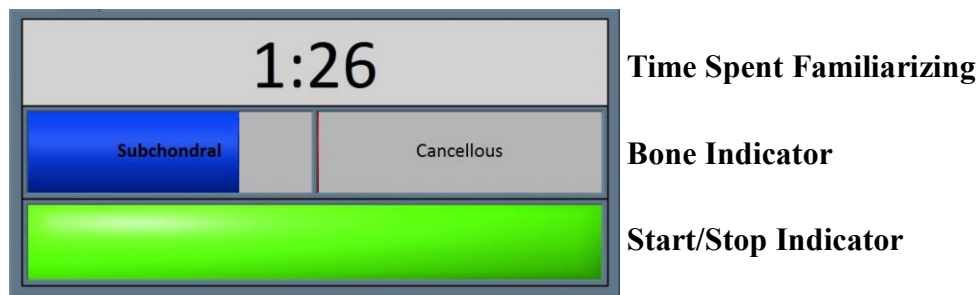


Figure 4.13: Familiarization Stage Graphical Indicator

For the familiarization stage each subject was given a graphical interface. The interface showed the time spent familiarizing with the simulator (top) and the bone layer being reamed with the relative depth of ream (middle). A start/stop indicator was shown to indicate when to start and stop reaming (bottom, green to start reaming and red to stop reaming).

In the second stage of the protocol, the subjects were asked to create a template for a glenoid reaming retroversion correction procedure. The subjects were shown the four simulated multi-slice CT images that were developed in section 4.1. and were asked to measure the glenoid retroversion using RadiAnt DICOM Viewer. From the measured glenoid retroversion, each subject determined a target correction angle to achieve an ideal

glenoid orientation. Within RadiAnt DICOM Viewer, participants were free to measure retroversion using the 2D slice they preferred. Each surgeon was blinded to the actual retroversion angle of each glenoid and the order that each glenoid was presented to the subjects was randomized.

Once templating was complete, the subjects were asked to ream four virtual glenoids on the reaming simulator according to his/her four pre-operative plans developed in the previous stage. For each ream, the glenoid component that matched the geometry of the DICOM used to develop the pre-operative plan was mounted to the simulator. While the subject reamed, a random vibration sequence consisting of subchondral and cancellous bone was played. Each subject was told that the ideal stop point was within subchondral bone and that he/she was to stop reaming when he/she felt that the glenoid had been adequately prepared. While reaming, each subject was shown a green/red indicator to communicate when they could begin reaming (shown in Figure 4.14). For each templated ream, the reamer vector measurement system measured the net force applied and the reamer angle of approach. The measured reamer angle of approach was used to determine and compare the intended version correction angle to the actual version correction angle reamed and compare the ideal to the “post-operative” glenoid orientation.

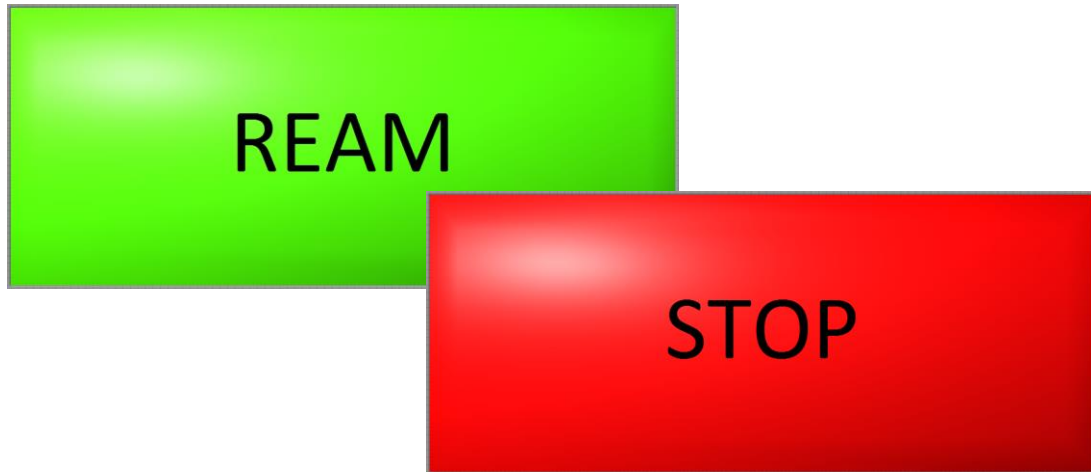


Figure 4.14: Glenoid Reaming Assessment Stage Graphical Indicator

For the glenoid reaming assessment stage each subject was given a graphical interface that had a single start/stop indicator to communicate when the participant could begin reaming (green to indicate the system was ready to begin reaming (top left), red to indicate that the system was not ready to begin reaming (bottom right)).

4.4 Results

4.4.1 Pre-Operative Templating Results

Each surgeon was asked to measure glenoid retroversion of four glenoids from simulated multi-slice CT images. The version angle of the native scapula geometry was measured for comparison using a 3D technique. The scapular plane, neutral inclination axis and neutral plane were defined as described in section 2.1.1 and section 4.2. A line segment (AP segment) was drawn between points on the anterior and posterior rim of the glenoid. The version angle was measured as the angle between the AP segment and the neutral plane and was found to be 0.4 degrees of anteversion. The other three glenoids were retroverted at known increments of 2.5 degrees so the version angle of the remaining three glenoid were, 2.1, 4.6, and 7.1 degrees of retroversion. The results from the surgeon CT glenoid version measurements are shown in Table 4.1. Glenoid retroversion angles of -0.4, 2.1, 4.6 and 7.1 correspond to specimens A, B, C and D, respectively.

Table 4.1: Glenoid Retroversion Measurements from the Generated CT Images

		<i>Specimen</i>				<i>Mean Step Size (°)</i>	
		<i>A</i>	<i>B</i>	<i>C</i>	<i>D</i>		
<i>Glenoid Retroversion (°)</i>	<i>Actual</i>	-0.4	2.1	4.6	7.1	2.50	
	<i>Surgeon</i>	<i>1</i>	0.5	5.1	8.7	11.7	3.7 ± 0.8
		<i>2</i>	2.0	4.0	7.0	9.0	2.3 ± 1.1
		<i>3</i>	3.0	6.0	7.1	10.0	2.3 ± 1.2
		<i>4</i>	4.0	6.0	9.0	12.0	2.7 ± 0.6
	<i>Surgeon Mean</i>	2.4 ± 1.5	5.3 ± 1.0	8.0 ± 1.0	10.7 ± 1.4	2.7 ± 0.9	

In every case, the surgeon measured a greater amount of retroversion than the actual glenoid retroversion. The difference ranged from 0.9 to 4.9 degrees more retroversion with an average step size between specimens of 2.7 ± 0.9 degrees compared to the actual step size of 2.5 degrees.

This increase in glenoid retroversion measured by the surgeons was the result of measuring glenoid version using a 2D technique, whereas the reference measurement was made using a 3D technique. Studies have shown that the accuracy of glenoid measurements made using 2D slices is lower than using a 3D model and that using 2D measurements results in overestimating glenoid retroversion [68], [72]. Overall, the errors between the two measuring techniques was consistent with previous studies [73].

From the glenoid retroversion measurements, each surgeon determined a desired correction angle and indicated the ideal post-operative glenoid orientation. These are summarized in Table 4.2 and Table 4.3.

Table 4.2: Intended Angle of Retroversion Correction

		<i>Specimen</i>			
		<i>A</i>	<i>B</i>	<i>C</i>	<i>D</i>
<i>Retroversion Correction Angle (°)</i>	<i>Surgeon</i>				
	<i>1</i>	0.0	5.0	9.0	12.0
	<i>2</i>	2.0	4.0	7.0	9.0
	<i>3</i>	3.0	6.0	7.0	5.0
	<i>4</i>	0.0	1.0	4.0	7.0
	<i>Surgeon Mean</i>	1.3 ± 1.5	4.0 ± 2.2	6.8 ± 2.1	8.3 ± 3.0

Table 4.3: Ideal Post-Operative Glenoid Orientation

		<i>Specimen</i>			
		<i>A</i>	<i>B</i>	<i>C</i>	<i>D</i>
<i>Ideal Post-Operative Retroversion Angle (°)</i>	<i>Surgeon</i>				
	<i>1</i>	0.0	0.0	0.0	0.0
	<i>2</i>	0.0	0.0	0.0	0.0
	<i>3</i>	0.0	0.0	0.0	5.0
	<i>4</i>	4.0	5.0	5.0	5.0
	<i>Surgeon Mean</i>	1.3 ± 1.5	4.0 ± 2.2	6.8 ± 2.1	8.3 ± 3.0

4.4.2 Reaming Performance Results

While each subject reamed on the simulator, the reamer vector measurement system measured the user's net force applied and the reamer version and inclination angles of approach. The subjects were assessed based on their ability to accurately change glenoid retroversion by a desired angle and to correct the glenoid orientation to the ideal

orientation. For each ream, the measured version and inclination angles of approach and net force applied were averaged over the duration of the ream.

4.4.2.1 Version Angle of Approach Results

Each subject's retroversion correction angles were compared to their intended corrections. The difference between the intended and actual correction was calculated and is summarized in Table 4.4. Positive values indicate that there was an over-correction of glenoid retroversion and negative values indicate that there was an under-correction.

Table 4.4: Difference Between Intended and Actual Retroversion Correction Angle

		<i>Specimen</i>				<i>Surgeon Average</i>	
		A	B	C	D		
<i>Retroversion Correction Angle (°)</i>	<i>Surgeon</i>	1	2.8	-4.4	-1.9	-4.7	-2.1 ± 3.5
		2	-5.8	-6.6	-1.3	-2.4	-4.0 ± 2.6
		3	-9.9	-7.8	-7.2	-2.2	-6.8 ± 3.3
		4	-0.8	0.2	-0.6	-1.6	-0.7 ± 0.7
	<i>Surgeon Mean</i>		-3.4 ± 5.6	-4.6 ± 3.5	-2.7 ± 3.0	-2.7 ± 1.4	-3.4 ± 3.4

Table 4.4 shows that on average, participants under-corrected glenoid retroversion by 3.4 ± 3.4 degrees compared what was intended. In the templating stage of the protocol, the subjects measured a larger amount of glenoid retroversion than the actual retroversion angle. In all cases, the surgeon determined the required amount of version correction by observing the difference in the pre-operative glenoid retroversion and their desired post-operative retroversion angle. The results presented in Table 4.4 indicates whether or not the subjects were able to change the glenoid version by the target amount, but it is important to investigate if the actual post-operative glenoid orientation matched the subjects ideal post-operative orientation. Table 4.5 shows the difference between the

ideal and actual post-operative glenoid orientations. Final glenoid orientations were determined with respect to the actual glenoid retroversion measured using a 3D technique. Positive values indicate the glenoid was more anteverted than intended and negative values indicate that the glenoid was more retroverted than intended.

Table 4.5: Difference Between Intended and Final Glenoid Version Orientation

		<i>Specimen</i>				<i>Surgeon Average</i>	
		<i>A</i>	<i>B</i>	<i>C</i>	<i>D</i>		
<i>Post-operative Glenoid Version Orientation (°)</i>	<i>Surgeon</i>	<i>1</i>	3.3	-1.8	1.8	-0.5	0.7 ± 2.3
		<i>2</i>	-3.8	-5.1	0.7	-0.9	-2.3 ± 2.6
		<i>3</i>	-6.9	-4.3	-5.1	0.3	-4.0 ± 3.1
		<i>4</i>	4.2	2.7	3.4	2.9	3.3 ± 0.7
	<i>Surgeon Mean</i>	-0.8 ± 5.4	-2.1 ± 3.5	0.2 ± 3.7	0.4 ± 1.7	-0.6 ± 3.5	

Iannotti et al. reported that in cases with glenoid retroversion of less than 10 degrees, the glenoid version was corrected within 5 degrees of the ideal angle in 67% of cases and within 10 degrees in 100% of cases [74]. In this study, glenoid retroversion was corrected within 5 degrees of the target orientation in 81% of cases and within 10 degrees in 100% of cases.

A paired t-test was conducted to compare the means of the difference between the intended and actual glenoid retroversion change and the difference between the ideal and actual post-operative glenoid orientation. On average, the difference between the ideal and actual post-operative glenoid orientations was 0.6 ± 3.5 degrees of retroversion and was significantly less ($P < 0.01$) than the difference between the intended correction angle and the actual correction angle which was 3.4 ± 3.4 degrees of retroversion. A one-sample t-test showed that the mean difference between the intended and actual post-

operative glenoid orientations was not statistically different from a perfect correction of 0 degrees difference ($P=0.538$).

In the templating stage, the surgeons over-estimated glenoid retroversion for every case as would be expected using a 2D measurement technique. Moving to the reaming stage of the protocol it would be expected for the surgeons to over correct the glenoid retroversion if reaming was performed purely based on the desired change in glenoid retroversion determined pre-operatively. However, it was been shown that on average there was no statistical difference between the intended post-operative glenoid orientation and actual post-operative glenoid orientation. This suggests that the surgeons didn't solely rely on their pre-operative plan to perform glenoid reaming but adjusted their reamer angle of approach based on the physical anatomy of the shoulder model mounted to the simulator to achieve a desired post-operative glenoid orientation. This emphasizes the importance of accurately simulating the physical anatomy in surgical simulation and particularly in glenoid reaming simulation as it may influence the accuracy of glenoid retroversion correction reaming.

Interestingly, surgeon 4 showed much less variability in the correction errors and showed much higher accuracy in correcting glenoid retroversion by the desired angle (-0.7 ± 0.7 degrees) than the other surgeons. This led to an over-correction of glenoid retroversion because of the initial over-estimation of glenoid retroversion from the 2D CT angle measurement technique. Surgeon 4 is the most experienced surgeon of the cohort and doesn't seem to follow the trends of the group. This difference may be the result of increased experience; however, given the current small sample size, further study needs to be done with additional surgeons with higher levels of experience to confirm or deny this finding.

Previous studies have shown that surgeon handedness can influence implant placement and surgical outcomes in arthroplasty procedures [75], [76]. In the cohort presented, all surgeons were right-hand dominant except for surgeon 2 who was left-hand dominant. The average difference between the intended and actual change in glenoid retroversion correction angle was -3.2 ± 3.7 degrees for right-handed surgeons and -4.0 ± 2.6 degrees

for the left-handed surgeon. The average difference between the intended and actual final glenoid retroversion angle was 0.0 ± 3.8 degrees for right-handed surgeons and -2.3 ± 2.6 degrees for the left-handed surgeon. For this cohort, the left-handed surgeon was less accurate in correcting the glenoid version according to the target angle and was less accurate in achieving the desired ideal final glenoid orientation compared to the right-handed surgeons. This difference may be the result of hand dominance; however, given the current small sample size and that all the specimens reamed in this study were left shoulders, further study needs to be done to assess the effect of handedness on glenoid reaming accuracy.

Finally, a repeated measures analysis of variance (ANOVA) test was performed to determine the effect of specimen glenoid orientation on the ability of the surgeons tested to achieve the desired glenoid orientation after reaming. There was no significant effect of initial specimen glenoid retroversion ($P=0.441$).

4.4.2.2 Inclination Angle of Approach Results

Each glenoid had an inclination angle of -2.7 degrees (glenoid was rotated 2.7 degrees inferiorly). This was measured from the 3D model by finding the angle between a line segment drawn between the superior and inferior points of the glenoid and the neutral plane. None of the subjects were given instruction about altering the glenoid inclination angle so it was of interest to know if the participants altered the inclination angle of the glenoid while attempting to correct glenoid retroversion. The final glenoid inclination angle was calculated for each ream using the inclination angle of approach measurements. The inclination angle results are summarized in Table 4.6. Positive results indicate that the glenoid was superiorly rotated and negative values indicate that the glenoid was inferiorly rotated.

Table 4.6: Final Glenoid Inclination Angle Summary

		<i>Specimen</i>				<i>Surgeon Average</i>
		<i>A</i>	<i>B</i>	<i>C</i>	<i>D</i>	
<i>Post-operative Glenoid Inclination Orientation (°)</i>	<i>1</i>	8.9	4.2	5.9	4.3	5.8 ± 2.2
	<i>2</i>	0.4	4.0	4.9	6.9	4.1 ± 2.7
	<i>3</i>	-1.1	2.3	0.7	5.4	1.8 ± 2.8
	<i>4</i>	0.7	2.0	5.7	-0.2	2.1 ± 2.6
	<i>Surgeon Mean</i>	2.2 ± 4.5	3.1 ± 1.1	4.3 ± 2.5	4.1 ± 3.1	3.4 ± 2.8

The average post-operative glenoid inclination angle was determined to be 3.4 ± 2.8 degrees; this was a 6.1 ± 2.8 degree change from the native state. A repeated measures ANOVA indicated that there was no effect of glenoid retroversion on final glenoid inclination angle ($P=0.703$).

4.4.2.3 Net Force Magnitude Results

The average net force applied by the subjects was measured for each ream. The net force results are summarized in Table 4.7.

Table 4.7: Net Force Magnitude Performance Summary

		<i>Specimen</i>				<i>Surgeon Average</i>	
		<i>A</i>	<i>B</i>	<i>C</i>	<i>D</i>		
<i>Final Glenoid Inclination Orientation (°)</i>	<i>Participant</i>	<i>1</i>	111	81.7	99.4	98.6	97.7 ± 12.1
		<i>2</i>	141.8	131.2	126.8	118.1	129.5 ± 9.9
		<i>3</i>	63.7	90.7	81.6	74.5	77.6 ± 11.4
		<i>4</i>	58.7	54.3	63.6	91.2	67.0 ± 16.6
	<i>Surgeon Mean</i>		93.8 ± 39.7	89.5 ± 31.8	92.8 ± 26.9	95.6 ± 18.1	92.9 ± 27.1

The average force applied by the subjects was 92.9 ± 27.1 N. A repeated measures ANOVA showed that there was no effect of glenoid orientation on net force applied during reaming ($P= 0.941$).

4.5 Summary

This chapter presented a study that was conducted to assess an expert surgeons' ability to accurately correct glenoid retroversion according to a pre-operative plan. To study this with a repeated measures approach, simulated CT images and a modular shoulder model were created.

In this study, surgeons were asked to measure glenoid retroversion from simulated CT images and develop a pre-operative plan to correct glenoid retroversion. Once planned, each surgeon reamed on a modular scapula model mounted to the simulator and the reamer vector measurement system was used to measure the reamer's angle of approach and the net force applied to determine the post-operative glenoid orientation.

The results from version measurements showed that there was an increased amount of retroversion measured when using 2D image slices compared to a 3D measurement technique which has been previously noted in literature. Results from reaming show that the subjects were effectively able to correct glenoid retroversion. Interestingly, when participants measured greater glenoid retroversion during pre-operative planning; however, this did not result in over-correction of glenoid retroversion, like what might be expected, but the final glenoid orientation was not statistically different from the intended glenoid orientation.

The results of this study were consistent with what has been previously reported. Findings in this study show that both pre-operative planning and accurate simulation of anatomy are important in glenoid reaming procedures and critical to the accuracy of glenoid reaming simulation.

Chapter 5

5 Discussion and Conclusions

Overview: This chapter reviews the objectives and hypotheses outlined in Chapter 1 and presents a summary of the design and calibration of a force-based reamer vector measurement system. The findings from a study conducted using the reamer vector measurement system to test the glenoid retroversion correction accuracy of expert surgeons are summarized. The strengths and limitations of this research are discussed, and future work is proposed.

5.1 Summary

Surgical training programs are changing because of the introduction of reduced work hours for trainees and an increased public concern for patient safety [30]. There is an increased emphasis on the need for competency-based training programs that can objectively measure resident proficiency [29]. Surgical simulation is a training modality that can objectively measure trainee performance and distance the trainee from patients while they learn the required skills. In orthopaedic surgery, several simulators have been developed that teach trainees skills for a variety of procedures; but none exist for total shoulder arthroplasty. At our institution, a vibration haptic simulator is being developed to be used as training tool to teach trainees the complex psychomotor skill of glenoid reaming [61]. Glenoid reaming is a typical step in total shoulder arthroplasty that is used to prepare the glenoid to receive the glenoid implant and is critical to the performance and lifespan of the prosthesis [20], [21]. The glenoid reaming simulator was initially equipped with a uniaxial load cell that measured the force applied perpendicular to the glenoid. However, many surgical cases require the surgeon to ream off-axis or eccentrically to correct the glenoid orientation due to uneven wear of the glenoid. To simulate these cases, a measurement system capable of measuring the net force applied by the reamer and the reamer angle of approach was needed.

The first objective of this research was to design and calibrate a force-based reamer vector measurement system that could measure the net force applied to the glenoid face and calculate the reamer's version and inclination angle of approach without the common line-of-sight or signal interference hindrances that occur with other tracking modalities. The developed system used the forces measured by three cantilever-load cells mounted to the back of the simulator to calculate the net force applied by the user and the reamer angle of approach. To calibrate the system, a KUKA 7 axes robot was actuated using position control to apply loads to a load cell mounted to the simulator. The initial calibration equations showed significant errors due to large deflections and the instability of the reamer vector measurement system configuration. To compensate for these errors, multiple stages of error prediction were incorporated to estimate the expected error based on measured parameters. Following error compensation, the error of the system was greatly reduced, and the system was demonstrated to be repeatable. The mean absolute errors were 0.2 ± 0.2 degrees, 0.2 ± 0.2 degrees, and 0.4 ± 0.3 N for version angle, inclination angle and net force magnitude, respectively.

To assess the error of the force measurement system using a more clinically relevant method of loading, the KUKA robot was actuated in force-control to apply a target load at specific reamer orientations. The reamer vector measurement system force measurements were compared to a load cell and the reamer angle of approach measurements were compared to a load cell and a Certus Optotrak system. Using the robot in force-control introduced two errors into the system. The first error resulted from the robot's limited capability of minimizing the transverse load applied at the reamer tip. This introduced measurement errors into the system because it violated the assumption that the net force vector and reamer shaft were collinear. Secondly, the reamer tip impinged in the pilot hole at larger angles of approach. This induced a moment at the tool tip which increased measurement errors. Overall, the mean absolute errors of the system when measuring under force control and adjusting for the sources of error ranged from 0.1 ± 0.1 to 0.2 ± 0.1 degrees for version angle, 0.3 ± 0.2 to 0.5 ± 0.2 degrees for inclination angle and 0.2 ± 0.1 to 0.7 ± 0.3 N for net force magnitude. The errors

observed when actuating the robot under position-control and under force-control satisfy the first objective and confirm *Hypothesis 1* mentioned in Chapter 1.

Once the reamer vector force measurement system was calibrated and its performance was validated it was used to study surgeons' ability to correct glenoid retroversion according to a pre-operative plan. Surgeons were asked to measure glenoid retroversion from four simulated CT images and determine the desired retroversion correction angle and the ideal post-operative glenoid orientation. Given their pre-operative plan, each surgeon reamed four virtual glenoids on the glenoid reaming simulator that corresponded to the four simulated CT images. The surgeons used a modified surgical reamer to ream on a modular scapula model mounted to the front of the simulator. The reamer vector measurement system was used to calculate the change between the pre-operative and post-operative glenoid orientations and compare what the surgeon intended to what was actually performed.

The results from glenoid retroversion measurements showed that in every case the surgeons overestimated glenoid retroversion. This was caused by using a 2D measuring technique instead of a 3D technique [68], [72]. The glenoid reaming results showed that on average the surgeons did not adjust glenoid retroversion by as much as they had planned (-3.4 ± 3.4 degrees less retroversion change than what was desired), but interestingly, the post-operative glenoid orientations were not significantly different from the ideal orientations (actual post-operative orientation was 0.6 ± 3.5 degrees more retroverted than the ideal orientation).

The second hypothesis in Chapter 1 stated that the average difference between a surgeon's correction target and the actual correction angle will be less than 5 degrees. This hypothesis was confirmed. Secondly, it was hypothesized that the correction error would increase as initial glenoid retroversion angle increased, but this was not the case as there was no significant effect of initial glenoid orientation on correction accuracy.

Initially, the surgeons over-estimated glenoid retroversion but this error was corrected when the surgeons performed the ream. The reason for this was attributed to the influence of the geometry of the 3D scapula mounted to the front of the simulator. When presented

with a physical 3D model, the surgeons adjusted their angle of approach to achieve the ideal post-operative glenoid orientation that could be visualized on the 3D model as they reamed. This emphasized the importance of accurately replicating anatomy in surgical simulation and particularly in glenoid reaming.

The surgeons were not given instruction on how to change inclination angle but there was an average increase in glenoid inclination angle of 6.1 ± 2.8 degrees resulting in a final glenoid inclination angle of 3.4 ± 2.8 degrees. The average glenoid reaming force was 95.6 ± 18.1 N. Finally, there was no significance of initial glenoid retroversion angle on glenoid retroversion change, post-operative glenoid retroversion, final inclination angle or force applied during reaming.

This work presents the successful design and calibration of a single measurement system that can measure both the force applied by the reamer and the reamer angle of approach during a simulated glenoid reaming procedure. The reamer vector measurement system was successfully implemented into an existing haptic vibration glenoid reaming simulator and was utilized to study retroversion correction glenoid reaming in the context of reaming simulation. This system broadens the capabilities of the glenoid reaming simulator and allows for the simulation of more complex reaming techniques in the future.

5.2 Strengths

This work presented a novel method for measuring net force magnitude and reamer orientation during glenoid reaming simulation using a single measurement system. The designed system used multi-stage calibration and error reduction to measure the desired parameters and was not hindered by line-of-sight issues or prone to signal interference. The developed system did not involve adding extra hardware to the surgical reamer as would be needed for serial linkages, optical tracking and electromagnetic tracking. The System allowed the user to have complete freedom and maneuverability with the surgical reamer. Additionally, the reamer vector measurement system was made of three

inexpensive cantilever load cells that are less expensive than equivalent commercial load cells.

The per-operative planning for the glenoid retroversion study used clinically relevant techniques and produced results consistent with what is found in literature. With the use of simulated CT images, glenoid retroversion was able to be isolated and allowed for a repeated measures study approach. Using a modular 3D printed scapula model increased the fidelity of the simulator and accurately replicated the bony anatomy used for the development of the pre-operative plans.

5.3 Limitations

This system was calibrated with the assumption that the force applied during reaming is collinear with the reamer shaft. Currently, the validity of this assumption is not fully known. Secondly, the reamer vector measurement system cannot differentiate between an axial load and a moment applied at the tool-glenoid interface. This limitation increases measurement error for angles of approach that deviate significantly from a neutral orientation. However, the conducted reaming study focused on cases with small degrees of retroversion, so this error was reduced.

In chapter 4, retroversion correction glenoid reaming was studied in the context of reaming simulation and not in a clinical setting. Unlike a clinical situation, the surgeons were not given feedback such as the physical removal of bone that would assist the surgeons in achieving the desired glenoid orientation correction. Additionally, the vibration profiles currently available with the simulator only allowed small retroversion correction angles to be studied; however, it is common for surgeons to encounter cases with larger degrees of retroversion. Finally, the results presented in chapter 4 were based on a small sample size which limited the conclusions that could be made.

5.4 Future Work

More participants will be recruited for the glenoid reaming retroversion correction study to increase the power of the results. In addition, the study will be expanded to study the effect of surgeon handedness on reaming accuracy for reaming both left and right

shoulders. Once more expert data has been collected, novice surgeons will be recruited to assess their ability to ream at a target angle of approach so that the accuracies of novice surgeons can be compared to the accuracies of expert surgeons. Finally, anticipating a significant difference between novice and expert surgeons, a training regimen will be designed to study whether the glenoid reaming simulator can improve novice surgeon's reaming capabilities to approach the accuracies of expert surgeons.

Secondly, preliminary results from the retroversion correction study suggest both pre-operative planning and visual cues during a glenoid reaming procedure influence the outcome of the procedure. More research will be done to explore and understand the influence and interaction between these two factors.

Glenoid reaming forces will be further studied to test the assumption of the collinearity used to calibrate the reamer vector measurement system. This study will examine the validity of this assumption for multiple reaming procedures (i.e. concentric reaming, low angle correction eccentric reaming and high angle correction eccentric reaming).

Finally, with the introduction of eccentric reaming simulation capabilities, reaming vibrations for eccentric reaming will be collected and analyzed to populate the simulator with eccentric reaming case vibrations. This will allow for the study of reaming accuracy using larger retroversion correction angles.

References

- [1] G. I. Bain, E. Itoi, G. di Giacomo, and H. Sugaya, *Normal and pathological anatomy of the shoulder*. 2015.
- [2] C. M. Lewandowski, *Atlas of Functional Shoulder Anatomy*, vol. 1. 2015.
- [3] M. T. Provencher and A. A. Romeo, *Shoulder Instability: A Comprehensive Approach*. Philadelphia, PA: Saunders Elsevier, 2012.
- [4] R. Kadi, A. Milants, and M. Shahabpour, "Shoulder Anatomy and Normal Variants," *J. Belgian Soc. Radiol.*, vol. 101, no. S2, p. 3, 2018.
- [5] M. B. Zlatkin, *MRI of the Shoulder*, 2nd ed. London, Philadelphia: Lippincott Williams & Wilkins, 2003.
- [6] H. P. Von Schroeder, S. D. Kuiper, and M. J. Botte, "Osseous anatomy of the scapula," *Clin. Orthop. Relat. Res.*, no. 383, pp. 131–139, 2001.
- [7] A. D. Woolf and B. Pfleger, "Burden of major musculoskeletal conditions," *Bull. World Health Organ.*, vol. 81, no. 9, pp. 646–657, Sep. 2003.
- [8] M. Brault, J. Hootman, C. Helmick, and K. Theis, "Morbidity and Mortality Weekly Report Update: Prevalence and Most Common Causes of Disability Among Adults — department of health and human services," 2009.
- [9] R. C. Lawrence *et al.*, "Estimates of the Prevalence of Arthritis and Other Rheumatic Conditions in the United States Part II," *ARTHRITIS Rheum.*, vol. 58, no. 1, pp. 26–35, 2008.
- [10] G. Walch, R. Babet, A. Boulahia, and A. Khoury, "Morphologic Study of the Glenoid in Primary Glenohumeral Osteoarthritis," 1999.
- [11] E. M. Padedgimas, M. Maltenfort, M. D. Lazarus, M. L. Ramsey, G. R. Williams, and S. Namdari, "Future Patient Demand for Shoulder Arthroplasty by Younger Patients: National Projections," *Clin. Orthop. Relat. Res.*, vol. 473, no. 6, pp. 1860–1867, 2015.
- [12] M. J. Carter, T. R. Mikuls, S. Nayak, E. V. Fehring, and K. Michaud, "Impact of total shoulder arthroplasty on generic and shoulder-specific health-related quality-of-life measures: A systematic literature review and meta-analysis," *J. Bone Jt. Surg. - Ser. A*, vol. 94, no. 17, p. e127(1), 2012.
- [13] S. H. Kim, B. L. Wise, Y. Zhang, and R. M. Szabo, "Increasing Incidence of Shoulder Arthroplasty in the United States," *J. Bone Jt. Surgery-American Vol.*, vol. 93, no. 24, pp. 2249–2254, Dec. 2011.
- [14] M. Wiater and M. Fabing, "Shoulder Arthroplasty: Prosthetic Options and Indications," *Am. Acad. Orthop. Surg.*, vol. 17, no. 7, pp. 415–425, 2009.
- [15] F. A. Matsen, B. Campbell, K. L. Smith, R. Kapil, J. M. Leith, and S. S. Hasan, "Characteristics of unsatisfactory shoulder arthroplasties," *J. Shoulder Elb. Surg.*, vol. 11, no. 5, pp. 431–441, 2003.
- [16] K. I. Bohsali, A. J. Bois, and M. A. Wirth, "Complications of Shoulder

- Arthroplasty,” *J. Bone Jt. Surg.*, vol. 99, no. 3, pp. 256–269, 2017.
- [17] Bohsali KI; Wirth MA; Rockwood CA, “Complications of Total Shoulder Arthroplasty,” *J. Bone Jt. Surg.*, vol. 88, no. 10, pp. 45–49, Oct. 2006.
- [18] P. Y. K. Chin, J. W. Sperling, R. H. Cofield, and C. Schleck, “Complications of total shoulder arthroplasty: Are they fewer or different?,” *J. Shoulder Elb. Surg.*, vol. 15, no. 1, pp. 19–22, 2006.
- [19] A. Farron, A. Terrier, and P. Büchler, “Risks of loosening of a prosthetic glenoid implanted in retroversion,” *J. Shoulder Elb. Surg.*, vol. 15, no. 4, pp. 521–526, 2006.
- [20] M. A. Wirth and C. Rockwood, “Current Concepts Review - Complications of Total Shoulder-Replacement Arthroplasty,” *J. Bone Jt. Surg.*, vol. 78, no. 4, pp. 603–616, 1996.
- [21] X. Chen *et al.*, “Version Correction via Eccentric Reaming Compromises Remaining Bone Quality in B2 Glenoids: A Computational Study,” *Clin. Orthop. Relat. Res.*, vol. 475, no. 12, pp. 3090–3099, Dec. 2017.
- [22] P. J. Denard and G. Walch, “Current concepts in the surgical management of primary glenohumeral arthritis with a biconcave glenoid,” *J. Shoulder Elb. Surg.*, vol. 22, no. 11, pp. 1589–1598, Nov. 2013.
- [23] T. A. Shapiro, M. H. McGarry, R. Gupta, Y. S. Lee, T. Q. Lee, and L. Beach, “Biomechanical effects of glenoid retroversion in total shoulder arthroplasty,” *J. Shoulder Elb. Surg.*, vol. 16, no. 3, 2007.
- [24] J. C. Ho, V. J. Sabesan, and J. P. Iannotti, “Glenoid Component Retroversion Is Associated with Osteolysis,” *J. Bone Jt. Surgery-American Vol.*, vol. 95, no. 12, pp. e82-1–8, Jun. 2013.
- [25] P. Clavert, P. J. Millett, and J. J. P. Warner, “Glenoid resurfacing: What are the limits to asymmetric reaming for posterior erosion?”
- [26] D. D. Nowak *et al.*, “Simulation of surgical glenoid resurfacing using three-dimensional computed tomography of the arthritic glenohumeral joint: The amount of glenoid retroversion that can be corrected,” *J. shoulder Elb. Surg.*, vol. 18, no. 5, pp. 680–688, 2009.
- [27] A. D. Kersten, C. Flores-Hernandez, H. R. Hoenecke, and D. D. D’lima, “Posterior augmented glenoid designs preserve more bone in biconcave glenoids,” *J. Shoulder Elb. Surg.*, vol. 24, no. 7, pp. 1135–1141, 2015.
- [28] D. Nguyen *et al.*, “Improved accuracy of computer assisted glenoid implantation in total shoulder arthroplasty: an in-vitro randomized controlled trial,” *J. shoulder Elb. Surg.*, vol. 18, no. 6, pp. 907–914, 2009.
- [29] P. Singh and A. Darzi, “Surgical training,” *Br. J. Surg.*, vol. 100, no. 3, pp. 307–309, 2013.
- [30] R. Steinbrook, “Health policy report,” *N. Engl. J. Med.*, vol. 347, no. 16, pp. 1296–1302, 2010.

- [31] I. Philibert, P. Friedmann, W. T. Williams, and for the members of the A. W. G. on R. D. Hours, "New Requirements for Resident Duty Hours," *JAMA*, vol. 288, no. 9, p. 1112, Sep. 2002.
- [32] K. Akhtar, K. Sugand, M. Sperrin, J. Cobb, N. Standfield, and C. Gupte, "Training safer orthopedic surgeons: Construct validation of a virtual-reality simulator for hip fracture surgery," *Acta Orthop.*, vol. 86, no. 5, pp. 616–621, 2015.
- [33] P. J. Fabri and J. L. Zayas-Castro, "Human error, not communication and systems, underlies surgical complications," *Surgery*, vol. 144, no. 4, pp. 557–565, 2008.
- [34] et al Birkmeyer JD, Siewers AE, "Hospital volume and surgical mortality in the United States," *N. Engl. J. Med.*, vol. 346, no. 15, pp. 1128–1137, 2002.
- [35] S. E. Regenbogen, C. C. Greenberg, D. M. Studdert, S. R. Lipsitz, M. J. Zinner, and A. A. Gawande, "Patterns of technical error among surgical malpractice claims: An analysis of strategies to prevent injury to surgical patients," *Ann. Surg.*, vol. 246, no. 5, pp. 705–711, Nov. 2007.
- [36] S. O. Rogers *et al.*, "Analysis of surgical errors in closed malpractice claims at 4 liability insurers," 2006.
- [37] A. A. Gawande, M. J. Zinner, D. M. Studdert, and T. A. Brennan, "Analysis of errors reported by surgeons at three teaching hospitals," 2003.
- [38] H. Sanfey, "Assessment of surgical training," *Surg. J. R. Coll. Surg. Edinburgh Irel.*, vol. 12, no. 6, pp. 350–356, 2014.
- [39] J. M. Rosen, S. A. Long, D. M. McGrath, and S. E. Greer, "Simulation in Plastic Surgery Training and Education: The Path Forward," *Plast. Reconstr. Surg.*, vol. 123, no. 2, pp. 729–738, Feb. 2009.
- [40] A. DeMaria, "Medicine, Aviation, and Simulation," *J. Am. Coll. Cardiol.*, 2011.
- [41] I. Badash, K. Burt, C. A. Solorzano, and J. N. Carey, "Innovations in surgery simulation: a review of past, current and future techniques," *Ann. Transl. Med.*, vol. 4, no. 23, pp. 453–453, Dec. 2016.
- [42] R. Aggarwal, T. Grantcharov, K. Moorthy, T. Milland, and A. Darzi, "Toward Feasible, Valid, and Reliable Video-Based Assessments of Technical Surgical Skills in the Operating Room," *Ann. Surg.*, vol. 247, no. 2, pp. 372–379, Feb. 2008.
- [43] P. G. Gauger *et al.*, "Association for Surgical Education Laparoscopic simulation training with proficiency targets improves practice and performance of novice surgeons," *Am. J. Surg.*, vol. 199, no. 1, pp. 72–80, 2010.
- [44] N. E. Seymour, "VR to OR: A Review of the Evidence that Virtual Reality Simulation Improves Operating Room Performance," *World J. Surg.*, vol. 32, no. 2, pp. 182–188, Feb. 2008.
- [45] E. Yiannakopoulou, N. Nikiteas, D. Perrea, and C. Tsigris, "Virtual reality simulators and training in laparoscopic surgery," *Int. J. Surg.*, vol. 13, pp. 60–64, 2015.

- [46] A. Parra-Blanco, N. González, R. González, J. Ortiz-Fernández-Sordo, and C. Ordieres, “Animal models for endoscopic training: do we really need them?,” *Endoscopy*, vol. 45, no. 6, pp. 478–484, 2013.
- [47] J. N. Carey *et al.*, “Simulation of plastic surgery and microvascular procedures using perfused fresh human cadavers,” *J. Plast. Reconstr. Aesthetic Surg.*, vol. 67, no. 2, pp. e42–e48, 2014.
- [48] S. de Montbrun and H. MacRae, “Simulation in Surgical Education,” *Clin. Colon Rectal Surg.*, vol. 25, no. 3, pp. 156–165, Sep. 2012.
- [49] R. M. Satava, “Historical Review of Surgical Simulation-A Personal Perspective,” *World J. Surg.*, vol. 32, no. 2, pp. 141–148, 2008.
- [50] S. M. B. I. Botden, A. E. Jack, and J. Jakimowicz, “What is going on in augmented reality simulation in laparoscopic surgery?,” *Surg. Endosc.*, vol. 23, no. 8, pp. 1693–1700, 2009.
- [51] “ARTHRO Mentor | Simbionix,” 2017. .
- [52] “Validation Studies-Abstracts TM ARTHRO Mentor,” 2012.
- [53] “OSSimTech - Creators of VR open surgery training simulators in orthopedics - Sim-Ortho,” 2019. .
- [54] “VirtaMed | ArthroS™ simulator for knee, shoulder, hip and ankle arthroscopy training,” 2019. .
- [55] “TraumaVision - medical orthopedic simulator | Simulation,” 2018. .
- [56] P. Pedersen, H. Palm, C. Ringsted, and L. Konge, “Virtual-reality simulation to assess performance in hip fracture surgery,” *Acta Orthop.*, vol. 85, no. 4, pp. 403–407, 2014.
- [57] “ArthroVision – medical arthroscopy simulator | Simulation,” 2018. .
- [58] “Precision OS - The Most Advanced Orthopaedic Surgery Simulation,” 2019. .
- [59] “Precision OS Virtual Reality Kit Opportunity | mysite.” .
- [60] “Osso VR: The Leading, virtual reality surgical training & assessment platform.” .
- [61] J. R. Kusins, J. A. Strelzow, M.-E. LeBel, and L. M. Ferreira, “Development of a vibration haptic simulator for shoulder arthroplasty,” *Int. J. Comput. Assist. Radiol. Surg.*, Mar. 2018.
- [62] A. D. Milne, D. G. Chess, J. A. Johnson, and G. King, “Accuracy of an electromagnetic tracking device: A study of the optimal operating range and metal interference,” *J. Biomech.*, vol. 29, no. 6, pp. 791–793, 1996.
- [63] F.-C. Poulin and L.-P. Amiot, “Interference during the use of an electromagnetic tracking system under OR conditions,” 2002.
- [64] M. Maybody, C. Stevenson, and S. B. Solomon, “Overview of Navigation Systems in Image-Guided Interventions,” *Tech. Vasc. Interv. Radiol.*, vol. 16, no. 3, pp. 136–143, 2013.

- [65] S. Allin, Y. Matsuoka, and R. Klatzky, “Measuring just noticeable differences for haptic force feedback: implications for rehabilitation,” in *Proceedings 10th Symposium on Haptic Interfaces for Virtual Environment and Teleoperator Systems. HAPTICS 2002*, pp. 299–302.
- [66] N. Gurari, A. M. Okamura, and K. J. Kuchenbecker, “Perception of force and stiffness in the presence of low-frequency haptic noise,” *PLoS One*, vol. 12, no. 6, p. e0178605, Jun. 2017.
- [67] L. Schmidt, L. Depper, and G. Kerkhoff, “Effects of age, sex and arm on the precision of arm position sense—left-arm superiority in healthy right-handers,” *Front. Hum. Neurosci.*, vol. 7, no. December, pp. 1–11, 2013.
- [68] F. van de Bunt *et al.*, “Glenoid version by CT scan : an analysis of clinical measurement error and introduction of a protocol to reduce variability,” *Skeletal Radiol.*, vol. 44, no. 11, pp. 1627–1635, 2015.
- [69] J. R. Kusins, R. Willing, G. J. King, and L. M. Ferreira, “Development of a Computational Elbow Model with Experimental Validation of Kinematics and Muscle Forces,” *J. Appl. Biomech.*, vol. 32, no. 4, pp. 407–414, Aug. 2016.
- [70] D. T. Axford, “Development of a Force Measurement System for a Surgical Simulator,” Western University, 2017.
- [71] T. K. Koo and M. Y. Li, “A Guideline of Selecting and Reporting Intraclass Correlation Coefficients for Reliability Research,” *J. Chiropr. Med.*, vol. 15, no. 2, pp. 155–163, 2016.
- [72] C. L. Zale, G. I. Pace, G. S. Lewis, J. Chan, and H. M. Kim, “Interdepartmental imaging protocol for clinically based three-dimensional computed tomography can provide accurate measurement of glenoid version,” *J. Shoulder Elb. Surg.*, vol. 27, no. 7, pp. 1297–1305, 2018.
- [73] H. R. H. Jr, J. C. Hermida, C. Flores-hernandez, and D. D. D. Lima, “Accuracy of CT-based measurements of glenoid version for total shoulder arthroplasty,” *J. Shoulder Elb. Surg.*, vol. 19, no. 2, pp. 166–171, 2010.
- [74] J. P. Iannotti, C. Greeson, D. Downing, V. Sabesan, and J. A. Bryan, “Effect of glenoid deformity on glenoid component placement in primary shoulder arthroplasty,” 2012.
- [75] N. Pennington, A. Redmond, T. Stewart, and M. Stone, “The impact of surgeon handedness in total hip replacement,” *Ann. R. Coll. Surg. Engl.*, vol. 96, no. 6, pp. 437–441, Sep. 2014.
- [76] X. Song *et al.*, “Is the cup orientation different in bilateral total hip arthroplasty with right-handed surgeons using posterolateral approach?,” *J. Orthop. Surg. Res.*, vol. 13, no. 1, p. 123, Dec. 2018.

Appendix A: Repeatability of Reamer Vector Measurement System Error Presented in Chapter 2

The following tables are the error results for each measurand and each trail used to determine the system repeatability. The mean error is determined for each angle of approach bin described in section 2.5. SPSS was used to calculate the intraclass correlation coefficient (ICC) for version angle error, inclination angle error and net force magnitude error across all five trials with a two-way mixed model with absolute agreement. When using a single measure, the ICCs were 0.655, 0.786 and 0.593 for version angle error, inclination angle error and net force magnitude error, respectively. Using average measures, the resulting ICCs were 0.905, 0.948 and 0.879 for version angle error, inclination angle error and net force magnitude error, respectively.

Version Angle of Approach Error

Table A.1: Average Version Angle of Approach Error (°) - Trial 1

		Version Angle (°)												
		-15	-12.5	-10	-7.5	-5	-2.5	0	2.5	5	7.5	10	12.5	15
Inclination Angle (°)	15	-0.0193	-0.0273	0.0208	0.0806	0.1166	0.1398	0.0916	0.1004	0.0647	0.0204	-0.0137	-0.0895	-0.0910
	12.5	-0.0320	-0.0027	0.0454	0.0319	0.0738	0.0665	0.0541	0.0218	0.0273	-0.0064	-0.0468	-0.0319	-0.0535
	10	0.0244	-0.0005	0.0146	0.0166	0.0387	0.0381	0.0452	0.0282	0.0031	0.0152	0.0109	-0.0375	0.0206
	7.5	0.0378	0.0276	0.0495	0.0382	0.0275	0.0025	0.0084	-0.0107	-0.0108	-0.0189	-0.0619	-0.0620	-0.0132
	5	0.0376	0.0345	0.0255	-0.0004	0.0011	-0.0103	-0.0036	-0.0073	-0.0047	-0.0171	-0.0234	-0.0304	-0.0106
	2.5	0.0345	0.0357	0.0118	-0.0217	-0.0202	-0.0120	-0.0313	-0.0137	-0.0269	-0.0245	-0.0117	-0.0058	0.0244
	0	-0.0233	-0.0310	-0.0416	-0.0465	-0.0358	-0.0364	-0.0216	-0.0160	0.0004	0.0263	0.0290	0.0094	0.0506
	-2.5	0.0017	-0.0061	-0.0356	-0.0389	-0.0189	-0.0394	-0.0207	0.0018	0.0022	0.0252	0.0427	0.0374	0.1120
	-5	-0.0320	-0.0183	-0.0451	-0.0514	-0.0689	-0.0473	-0.0205	0.0009	0.0044	0.0250	0.0369	0.0425	0.0871
	-7.5	-0.0471	-0.0037	-0.0485	-0.0507	-0.0327	-0.0308	0.0068	0.0016	0.0265	0.0602	0.0659	0.0352	0.1518
	-10	-0.0645	-0.0219	-0.0771	-0.0727	-0.0264	-0.0259	0.0117	0.0282	0.0622	0.0686	0.0875	0.0500	0.1319
	-12.5	-0.0800	-0.0062	-0.0467	-0.0383	-0.0371	-0.0121	0.0483	0.0738	0.1086	0.0817	0.0904	0.0247	0.1538
	-15	-0.0862	-0.0785	-0.1396	-0.0829	-0.0139	-0.0358	0.0146	0.0498	0.0827	0.1322	0.1444	0.1402	0.1558

Table A.2: Average Version Angle of Approach Error (°) - Trial 2

		Version Angle (°)												
		-15	-12.5	-10	-7.5	-5	-2.5	0	2.5	5	7.5	10	12.5	15
Inclination Angle (°)	15	0.0180	0.0451	0.0840	0.1255	0.1569	0.1774	0.0970	0.1037	0.0709	0.0395	-0.0108	-0.1085	-0.0896
	12.5	0.0228	0.0683	0.1025	0.0980	0.1032	0.0977	0.0629	0.0298	0.0134	0.0028	-0.0306	-0.0797	-0.0243
	10	0.0594	0.0512	0.0582	0.0531	0.0864	0.0866	0.0295	0.0286	0.0214	0.0233	-0.0135	-0.0403	-0.0421
	7.5	0.0779	0.0756	0.0575	0.0586	0.0527	0.0308	0.0075	-0.0086	-0.0388	-0.0543	-0.0561	-0.0361	-0.0112
	5	0.0744	0.0775	0.0609	0.0554	0.0571	0.0252	-0.0050	-0.0122	-0.0061	-0.0073	-0.0068	-0.0181	-0.0271
	2.5	0.0557	0.0334	0.0273	0.0239	0.0191	-0.0449	-0.0078	-0.0338	-0.0288	0.0032	-0.0183	-0.0300	0.0223
	0	0.0074	0.0136	-0.0190	-0.0072	-0.0077	-0.0343	-0.0262	-0.0226	0.0012	0.0150	0.0400	-0.0057	0.0496
	-2.5	0.0275	0.0433	-0.0044	0.0129	-0.0022	-0.0371	0.0199	0.0199	0.0169	0.0534	0.0550	-0.0037	0.0753
	-5	-0.0410	-0.0109	-0.0557	-0.0375	-0.0105	-0.0160	-0.0141	0.0117	0.0259	0.0299	0.0153	0.0547	0.0850
	-7.5	-0.0172	0.0239	-0.0239	-0.0064	-0.0209	-0.0152	-0.0167	-0.0132	0.0187	0.0366	0.0514	0.0423	0.0959
	-10	-0.0531	-0.0158	-0.0659	-0.0523	-0.0195	-0.0016	-0.0065	0.0112	0.0602	0.0493	0.0531	0.0530	0.0241
	-12.5	-0.0381	0.0151	-0.0183	-0.0043	-0.0360	-0.0280	0.0321	0.0802	0.1052	0.0566	0.0353	0.0188	0.1564
	-15	-0.0515	-0.0660	-0.1003	-0.0380	0.0204	0.0083	-0.0256	0.0283	0.0985	0.0984	0.1599	0.1185	0.1417

Table A.3: Average Version Angle of Approach Error (°) - Trial 3

		Version Angle (°)														
		-15	-12.5	-10	-7.5	-5	-2.5	0	2.5	5	7.5	10	12.5	15		
Inclination Angle (°)	15	0.0154	0.0293	0.0854	0.1060	0.1056	0.1363	0.0771	0.0364	0.0098	-0.0163	-0.0543	-0.1296	-0.1810		
	12.5	0.0149	0.0450	0.0685	0.0741	0.0922	0.0449	0.0365	0.0192	-0.0014	-0.0479	-0.0850	-0.1188	-0.1206		
	10	0.0282	0.0389	0.0457	0.0573	0.0655	0.0385	0.0039	-0.0080	-0.0368	-0.0487	-0.0490	-0.0654	-0.0288		
	7.5	0.0414	0.0459	0.0572	0.0468	0.0386	-0.0128	-0.0193	-0.0244	-0.0377	-0.0596	-0.0797	-0.0863	-0.0823		
	5	0.0389	0.0726	0.0193	0.0254	-0.0012	-0.0275	-0.0319	-0.0362	-0.0342	-0.0370	-0.0717	-0.0919	-0.0551		
	2.5	0.0512	0.0648	0.0267	0.0252	0.0076	-0.0510	-0.0458	-0.0415	-0.0475	-0.0412	-0.0633	-0.0819	-0.0493		
	0	0.0161	0.0162	-0.0180	-0.0111	-0.0158	-0.0529	-0.0422	-0.0289	-0.0122	-0.0063	-0.0123	-0.0181	0.0019		
	-2.5	0.0217	0.0119	-0.0134	-0.0182	-0.0374	-0.0943	-0.0358	-0.0247	-0.0125	-0.0074	0.0008	-0.0004	-0.0128		
	-5	-0.0099	0.0091	-0.0252	-0.0155	-0.0304	-0.0566	-0.0579	-0.0193	-0.0339	-0.0351	-0.0166	-0.0033	0.0238		
	-7.5	-0.0384	-0.0249	-0.0511	-0.0642	-0.0642	-0.0586	-0.0570	-0.0257	0.0047	0.0004	0.0139	-0.0025	0.0696		
	-10	-0.0158	-0.0193	-0.0568	-0.0332	-0.0459	-0.0641	-0.0515	-0.0080	0.0107	0.0228	0.0056	-0.0340	0.0039		
	-12.5	-0.0469	0.0477	-0.0340	-0.0646	-0.0777	-0.0756	-0.0112	0.0223	0.0492	0.0227	0.0448	0.0386	0.0384		
	-15	-0.0668	-0.1013	-0.0882	-0.0375	-0.0056	-0.0151	-0.0258	-0.0064	-0.0048	0.0323	0.0304	0.0586	0.1129		

Table A.4: Average Version Angle of Approach Error (°) - Trial 4

		Version Angle (°)														
		-15	-12.5	-10	-7.5	-5	-2.5	0	2.5	5	7.5	10	12.5	15		
Inclination Angle (°)	15	0.0437	0.0613	0.0801	0.1113	0.1254	0.1100	0.0518	0.0553	0.0190	-0.0246	-0.0851	-0.1627	-0.2101		
	12.5	0.0337	0.0551	0.0689	0.0703	0.0934	0.0418	0.0168	0.0025	-0.0114	-0.0490	-0.1063	-0.1494	-0.1795		
	10	0.0593	0.0453	0.0426	0.0599	0.0251	-0.0090	-0.0098	-0.0135	-0.0450	-0.0527	-0.0822	-0.1298	-0.0553		
	7.5	0.0574	0.0584	0.0613	0.0397	0.0185	-0.0070	-0.0313	-0.0376	-0.0522	-0.0765	-0.1129	-0.1378	-0.0923		
	5	0.0666	0.0537	0.0344	0.0277	0.0054	-0.0201	-0.0510	-0.0635	-0.0675	-0.0801	-0.1270	-0.1412	-0.0974		
	2.5	0.0559	0.0411	0.0248	0.0030	-0.0053	-0.0452	-0.0616	-0.0547	-0.0647	-0.0740	-0.0781	-0.1274	-0.0703		
	0	0.0229	0.0118	-0.0126	-0.0142	-0.0322	-0.0622	-0.0549	-0.0393	-0.0316	-0.0325	-0.0528	-0.0604	-0.0659		
	-2.5	0.0334	0.0042	-0.0275	-0.0370	-0.0350	-0.0745	-0.0390	-0.0252	-0.0167	-0.0414	-0.0155	-0.0279	-0.0247		
	-5	0.0051	0.0092	-0.0424	-0.0333	-0.0582	-0.0744	-0.0792	-0.0356	-0.0606	-0.0611	-0.0485	-0.0434	-0.0361		
	-7.5	-0.0102	0.0034	-0.0472	-0.0380	-0.0380	-0.0755	-0.0686	-0.0406	0.0001	-0.0334	-0.0202	-0.0461	0.0078		
	-10	-0.0357	-0.0097	-0.0664	-0.0824	-0.0755	-0.0539	-0.0654	-0.0088	0.0092	-0.0259	0.0244	-0.0005	0.0269		
	-12.5	-0.0406	0.0038	-0.0437	-0.0274	-0.0506	-0.0720	-0.0479	-0.0017	0.0649	0.0476	0.0141	-0.0534	-0.0021		
	-15	-0.0097	-0.0503	-0.0766	-0.0818	-0.0519	0.0033	-0.0805	0.0044	0.0271	0.0311	0.0580	-0.0050	0.0742		

Table A.5: Average Version Angle of Approach Error (°) - Trial 5

		Version Angle (°)												
		-15	-12.5	-10	-7.5	-5	-2.5	0	2.5	5	7.5	10	12.5	15
Inclination Angle (°)	15	0.0605	0.0647	0.0777	0.1196	0.1313	0.1786	0.0440	0.0159	-0.0039	-0.0378	-0.0884	-0.1731	-0.2042
	12.5	0.0284	0.0347	0.0514	0.0682	0.0502	0.0125	-0.0100	-0.0357	-0.0516	-0.0942	-0.1055	-0.1469	-0.1147
	10	0.0404	0.0224	0.0250	0.0533	0.0466	-0.0016	-0.0301	-0.0457	-0.0553	-0.0620	-0.0712	-0.1657	-0.1355
	7.5	0.0547	0.0428	0.0437	0.0362	0.0130	-0.0391	-0.0625	-0.0541	-0.0831	-0.0785	-0.1031	-0.0954	-0.1279
	5	0.0658	0.0497	0.0252	0.0172	-0.0005	-0.0384	-0.0702	-0.0862	-0.0816	-0.1054	-0.1434	-0.1450	-0.1306
	2.5	0.0421	0.0402	0.0127	-0.0084	-0.0135	-0.0636	-0.0730	-0.0881	-0.0660	-0.0588	-0.0826	-0.1359	-0.0746
	0	-0.0033	0.0243	-0.0185	-0.0174	-0.0268	-0.0645	-0.0698	-0.0573	-0.0605	-0.0437	-0.0370	-0.0823	-0.0571
	-2.5	0.0075	0.0083	-0.0324	-0.0311	-0.0302	-0.1072	-0.0640	-0.0509	-0.0547	-0.0454	-0.0768	-0.0671	-0.0473
	-5	-0.0263	-0.0161	-0.0476	-0.0648	-0.0672	-0.0657	-0.1104	-0.0530	-0.0575	-0.0473	-0.0257	-0.0585	-0.0308
	-7.5	-0.0260	-0.0348	-0.0444	-0.0429	-0.0661	-0.1129	-0.1038	-0.0667	-0.0451	-0.0645	-0.0190	-0.0325	-0.0023
	-10	-0.0461	-0.0360	-0.0974	-0.0782	-0.0933	-0.1012	-0.0855	-0.0280	-0.0289	0.0147	0.0130	-0.0882	-0.1022
	-12.5	-0.0552	-0.0009	-0.0436	-0.0542	-0.0507	-0.1186	-0.0815	-0.0166	-0.0066	0.0165	-0.0598	-0.0193	0.0361
	-15	-0.0585	-0.0388	-0.0908	-0.0579	-0.0458	-0.1264	-0.1038	-0.0295	-0.0148	0.0261	0.0362	0.0269	0.0356

Inclination Angle of Approach Error

Table A.6: Average Inclination Angle of Approach Error (°) - Trial 1

		Version Angle (°)														
		-15	-12.5	-10	-7.5	-5	-2.5	0	2.5	5	7.5	10	12.5	15		
Inclination Angle (°)	15	0.0132	0.0807	0.0695	0.0726	0.0829	0.0434	-0.0348	-0.0216	0.0001	0.0030	-0.0152	0.0152	-0.0273		
	12.5	-0.0630	-0.0474	-0.0692	-0.0085	-0.0546	-0.0554	-0.0558	-0.0175	-0.0109	-0.0048	0.0040	0.0781	0.0261		
	10	-0.0704	-0.0541	-0.0565	-0.0325	-0.0305	-0.0093	-0.0265	0.0201	0.0362	0.0567	0.0420	0.0506	0.0849		
	7.5	-0.0237	-0.0272	-0.0224	-0.0040	-0.0236	-0.0068	0.0066	0.0254	0.0072	0.0301	0.0156	0.0682	0.0835		
	5	-0.0097	-0.0282	-0.0127	0.0093	0.0137	0.0184	0.0445	0.0443	0.0549	0.0619	0.0590	0.0226	0.1404		
	2.5	0.0021	-0.0140	0.0262	0.0233	0.0582	0.0613	0.0661	0.0962	0.0673	0.0569	0.0767	0.0633	0.1159		
	0	-0.0021	0.0037	0.0148	0.0127	0.0211	0.0398	0.0843	0.0564	0.0365	0.0409	0.0351	0.0278	0.0358		
	-2.5	-0.0078	-0.0076	0.0217	0.0321	0.0328	0.0382	0.0533	0.0537	0.0313	0.0019	0.0521	-0.0047	0.0939		
	-5	0.0074	0.0030	0.0561	0.0318	0.0449	0.0516	0.0964	0.0558	0.0430	0.0525	0.0667	0.0159	0.1634		
	-7.5	0.0160	0.0280	0.0876	0.0865	0.1088	0.1213	0.1626	0.0679	0.0523	0.0867	0.0885	0.0378	0.2047		
	-10	0.0488	0.0634	0.0780	0.0713	0.1017	0.0939	0.2048	0.0644	0.0771	0.0990	0.0748	0.0267	0.1679		
	-12.5	0.2158	0.1804	0.1968	0.2036	0.2314	0.2230	0.2971	0.1544	0.1320	0.1581	0.1204	0.0954	0.2140		
	-15	-0.0808	-0.0465	0.0002	0.0214	0.0652	0.1742	0.3321	0.2817	0.2387	0.2431	0.2291	0.1733	0.2837		

Table A.7: Average Inclination Angle of Approach Error (°) - Trial 2

		Version Angle (°)													
		-15	-12.5	-10	-7.5	-5	-2.5	0	2.5	5	7.5	10	12.5	15	
Inclination Angle (°)	15	0.0367	0.0159	0.0369	0.0544	-0.0057	-0.0224	-0.0064	-0.0212	-0.0173	0.0107	-0.0049	0.0001	0.0116	
	12.5	-0.0739	-0.0787	-0.0674	-0.0454	-0.0621	-0.0787	-0.0320	-0.0342	-0.0166	-0.0253	-0.0414	-0.0164	0.0593	
	10	-0.0340	-0.0557	-0.0477	-0.0360	-0.0564	-0.0514	0.0241	0.0144	0.0276	0.0338	0.0393	0.0433	0.0954	
	7.5	-0.0278	-0.0166	-0.0054	0.0008	0.0100	0.0151	0.0406	0.0260	0.0187	0.0251	0.0306	0.0233	0.1389	
	5	-0.0116	-0.0031	0.0105	0.0240	0.0206	0.0400	0.0795	0.0573	0.0407	0.0521	0.0540	0.0532	0.0855	
	2.5	0.0187	0.0152	0.0378	0.0290	0.0397	0.0454	0.1058	0.0747	0.0603	0.1106	0.0557	0.0589	0.1010	
	0	-0.0048	0.0021	0.0227	0.0229	0.0312	0.0505	0.0860	0.0691	0.0672	0.0557	0.0570	0.0300	0.0555	
	-2.5	-0.0038	-0.0097	0.0447	0.0390	0.0298	0.0345	0.0653	0.0437	0.0480	0.0085	0.0320	-0.0073	0.0803	
	-5	0.0567	0.0204	0.0704	0.0563	0.0894	0.1194	0.1126	0.0727	0.0663	0.0682	0.0325	0.0268	0.1128	
	-7.5	0.0333	0.0024	0.0749	0.0622	0.0920	0.1334	0.1392	0.0861	0.0630	0.0713	0.0658	0.0174	0.2052	
	-10	0.0890	0.0618	0.0976	0.1048	0.1039	0.1038	0.1826	0.1021	0.1254	0.1014	0.0832	0.0676	0.2340	
	-12.5	0.2556	0.1415	0.1605	0.1539	0.1916	0.1994	0.2751	0.2042	0.1590	0.1510	0.0930	0.1381	0.2040	
	-15	-0.0351	-0.0111	-0.0006	0.0823	0.1170	0.1229	0.3334	0.2204	0.2610	0.2497	0.2087	0.2279	0.3100	

Table A.8: Average Inclination Angle of Approach Error (°) - Trial 3

		Version Angle (°)													
		-15	-12.5	-10	-7.5	-5	-2.5	0	2.5	5	7.5	10	12.5	15	
Inclination Angle (°)	15	0.0220	0.0222	0.0228	0.0039	-0.0171	-0.0250	-0.0043	-0.0003	0.0009	-0.0146	0.0003	-0.0022	0.0110	
	12.5	-0.0819	-0.0540	-0.0525	-0.0492	-0.0711	-0.0282	-0.0125	0.0016	-0.0027	-0.0092	0.0270	-0.0107	0.0770	
	10	-0.0609	-0.0394	-0.0226	-0.0178	-0.0149	-0.0215	0.0500	0.0257	0.0157	0.0418	0.0249	0.0664	0.1115	
	7.5	-0.0137	-0.0070	-0.0009	0.0062	0.0064	0.0362	0.0773	0.0321	0.0152	0.0455	0.0395	0.0468	0.0840	
	5	0.0135	0.0062	0.0256	0.0369	0.0292	0.0595	0.0937	0.0631	0.0714	0.0688	0.0408	0.0741	0.1581	
	2.5	0.0357	0.0207	0.0387	0.0422	0.0545	0.1020	0.1180	0.0863	0.0672	0.0775	0.0431	0.0700	0.1237	
	0	0.0135	0.0084	0.0325	0.0341	0.0519	0.0516	0.1155	0.0792	0.0609	0.0670	0.0464	0.0245	0.0856	
	-2.5	0.0651	0.0278	0.0576	0.0650	0.0746	0.1006	0.1249	0.1029	0.0836	0.0923	0.0481	0.0368	0.0937	
	-5	0.0822	0.0134	0.0824	0.0664	0.0901	0.1203	0.1594	0.1047	0.1153	0.0824	0.0656	0.0660	0.1611	
	-7.5	0.1189	0.0441	0.0909	0.0775	0.1182	0.1419	0.1822	0.1307	0.1591	0.1346	0.0639	0.0788	0.1763	
	-10	0.1663	0.1141	0.1691	0.1805	0.2034	0.2169	0.2401	0.1815	0.1664	0.1757	0.1171	0.1382	0.1632	
	-12.5	0.1369	0.1699	0.1825	0.2051	0.2856	0.2307	0.3384	0.2019	0.2113	0.1840	0.1207	0.1585	0.2189	
	-15	-0.0998	-0.0391	-0.0174	0.0556	0.1161	0.2030	0.3504	0.3118	0.3653	0.3529	0.2362	0.2400	0.3154	

Table A.9: Average Inclination Angle of Approach Error (°) - Trial 4

		Version Angle (°)												
		-15	-12.5	-10	-7.5	-5	-2.5	0	2.5	5	7.5	10	12.5	15
Inclination Angle (°)	15	0.0376	0.0436	0.0628	0.0911	0.0284	0.0243	0.0044	-0.0050	0.0147	0.0426	0.0315	0.0122	0.0359
	12.5	-0.0701	-0.0476	-0.0428	-0.0131	-0.0511	-0.0127	0.0264	0.0033	0.0335	0.0500	0.0232	0.0494	0.0664
	10	-0.0348	-0.0247	-0.0019	0.0229	0.0120	0.0207	0.0531	0.0312	0.0456	0.0664	0.0770	0.0971	0.1393
	7.5	-0.0027	0.0083	0.0245	0.0324	0.0280	0.0227	0.0680	0.0521	0.0608	0.0848	0.0651	0.0672	0.1507
	5	0.0273	0.0359	0.0544	0.0509	0.0732	0.0726	0.1173	0.0894	0.1112	0.0942	0.0918	0.0891	0.1918
	2.5	0.0649	0.0572	0.0688	0.0735	0.0892	0.1015	0.1515	0.1071	0.1093	0.1301	0.1384	0.1459	0.2294
	0	0.0765	0.0720	0.0911	0.0941	0.1147	0.1221	0.1550	0.1467	0.1392	0.1359	0.1154	0.1254	0.1340
	-2.5	0.1029	0.0646	0.0946	0.1086	0.1299	0.1391	0.1581	0.1475	0.1196	0.1209	0.1177	0.0798	0.3047
	-5	0.1623	0.0668	0.1177	0.1467	0.1732	0.1771	0.1924	0.1521	0.1365	0.1553	0.1180	0.1253	0.2781
	-7.5	0.1494	0.1199	0.1760	0.1792	0.2056	0.2153	0.2437	0.1909	0.1776	0.1621	0.1677	0.1437	0.2988
	-10	0.1697	0.1435	0.1673	0.1929	0.1960	0.2012	0.2980	0.2359	0.2116	0.1606	0.2120	0.1526	0.2901
	-12.5	0.2852	0.2851	0.2913	0.3094	0.3350	0.3163	0.3946	0.3145	0.2871	0.1960	0.2296	0.2500	0.3237
	-15	0.0809	0.0907	0.1858	0.1724	0.2351	0.3056	0.3977	0.3855	0.3986	0.4028	0.3294	0.3751	0.4631

Table A.10: Average Inclination Angle of Approach Error (°) - Trial 5

		Version Angle (°)												
		-15	-12.5	-10	-7.5	-5	-2.5	0	2.5	5	7.5	10	12.5	15
Inclination Angle (°)	15	0.0144	0.0142	0.0159	0.0414	0.0193	-0.0204	0.0059	0.0005	0.0048	0.0212	-0.0028	0.0233	0.0133
	12.5	-0.0940	-0.0368	-0.0199	-0.0236	-0.0129	-0.0423	0.0206	-0.0050	0.0194	-0.0066	0.0252	0.0301	0.0974
	10	-0.0338	-0.0172	-0.0125	0.0032	0.0064	0.0207	0.0502	0.0338	0.0395	0.0676	0.0531	0.0901	0.1783
	7.5	0.0053	0.0251	0.0305	0.0308	0.0236	0.0574	0.0715	0.0717	0.0542	0.0874	0.0710	0.0975	0.1713
	5	0.0217	0.0420	0.0446	0.0426	0.0486	0.0694	0.1101	0.0782	0.0865	0.0884	0.0896	0.0959	0.1856
	2.5	0.0577	0.0520	0.0837	0.0836	0.0818	0.0977	0.1436	0.1281	0.1356	0.1166	0.1160	0.0915	0.2005
	0	0.0508	0.0528	0.0767	0.0846	0.1007	0.1155	0.1601	0.1203	0.1361	0.1249	0.1100	0.1183	0.1619
	-2.5	0.1176	0.0552	0.1025	0.1111	0.1228	0.1298	0.1681	0.1460	0.1269	0.1055	0.1367	0.0969	0.1830
	-5	0.1367	0.0673	0.1299	0.1387	0.1503	0.1547	0.2016	0.1836	0.1371	0.1224	0.1504	0.0970	0.2066
	-7.5	0.1748	0.0946	0.1559	0.1521	0.1842	0.2119	0.2588	0.2071	0.1665	0.1739	0.1894	0.1129	0.2815
	-10	0.1847	0.1629	0.2066	0.2143	0.2360	0.2596	0.2979	0.2252	0.2184	0.1994	0.2026	0.1382	0.2976
	-12.5	0.3427	0.2486	0.2995	0.3152	0.3315	0.3826	0.3848	0.2782	0.2693	0.2831	0.2382	0.2071	0.3102
	-15	0.0899	0.0962	0.1304	0.1536	0.2551	0.3445	0.4676	0.3872	0.3762	0.3873	0.3244	0.3806	0.4163

Net Force Magnitude Error

Table A.11: Average Net Force Magnitude Error (N) - Trial 1

		Version Angle (°)													
		-15	-12.5	-10	-7.5	-5	-2.5	0	2.5	5	7.5	10	12.5	15	
Inclination Angle (°)	15	0.0642	-0.0100	-0.0717	-0.1262	-0.2267	-0.2446	-0.3212	-0.2285	-0.2644	-0.3018	-0.3708	-0.3496	-0.4616	
	12.5	-0.1253	-0.1427	-0.2413	-0.2141	-0.2580	-0.2065	-0.3104	-0.2343	-0.2446	-0.2767	-0.2782	-0.2844	-0.3876	
	10	-0.0745	-0.0846	-0.1667	-0.1825	-0.2570	-0.2508	-0.2305	-0.1825	-0.1790	-0.2056	-0.2697	-0.2630	-0.3061	
	7.5	-0.0207	-0.0438	-0.1049	-0.1474	-0.1855	-0.1973	-0.2342	-0.1466	-0.2209	-0.1774	-0.1781	-0.1606	-0.1590	
	5	0.0128	0.0498	-0.1147	-0.1286	-0.1981	-0.1639	-0.1994	-0.1078	-0.1429	-0.1725	-0.1659	-0.1246	-0.1161	
	2.5	0.0825	0.0597	-0.0413	-0.0883	-0.1127	-0.1419	-0.2065	-0.1104	-0.1127	-0.1098	-0.1155	-0.1147	-0.0962	
	0	0.0684	0.0544	-0.0793	-0.1039	-0.1435	-0.1684	-0.0902	-0.0664	-0.0785	-0.1072	-0.1109	-0.0772	-0.0851	
	-2.5	0.1152	0.1044	-0.0262	-0.0911	-0.1596	-0.1596	-0.1850	-0.1885	-0.1634	-0.1572	-0.1840	-0.0505	-0.1876	
	-5	0.0267	0.0821	0.0161	-0.0279	-0.0584	-0.0441	0.0243	-0.0692	-0.0716	-0.0357	-0.0988	-0.0761	-0.1459	
	-7.5	0.1083	0.1596	0.0787	0.0192	-0.0134	0.0224	0.1030	0.0037	0.0211	-0.0219	-0.0453	-0.0105	-0.2294	
	-10	0.1226	0.2055	0.1196	0.0799	0.0621	0.0264	0.1691	0.0530	0.0717	0.0624	0.0117	-0.0365	-0.1860	
	-12.5	0.3343	0.3366	0.2915	0.2441	0.2565	0.2674	0.2759	0.1450	0.0810	0.0542	0.0042	-0.0859	-0.1923	
	-15	-0.1210	0.0157	-0.1744	-0.0853	-0.0951	0.0574	0.2695	0.1956	0.1639	0.0974	0.0282	-0.1833	-0.1405	

Table A.12: Average Net Force Magnitude Error (N) - Trial 2

		Version Angle (°)												
		-15	-12.5	-10	-7.5	-5	-2.5	0	2.5	5	7.5	10	12.5	15
Inclination Angle (°)	15	0.1122	0.0124	-0.0318	-0.1809	-0.0628	-0.1187	-0.2586	-0.1696	-0.1772	-0.2462	-0.2874	-0.2796	-0.4272
	12.5	-0.0491	-0.0228	-0.1268	-0.1080	-0.1623	-0.1402	-0.1420	-0.0790	-0.1253	-0.0901	-0.1750	-0.2104	-0.3666
	10	0.0489	0.0297	-0.0507	-0.0758	-0.0868	-0.0926	-0.1448	-0.0927	-0.1376	-0.1556	-0.1647	-0.1800	-0.1645
	7.5	0.0768	0.0755	-0.0469	-0.0965	-0.1329	-0.0793	-0.1329	-0.0630	-0.0645	-0.0355	-0.0762	-0.1235	-0.1297
	5	0.0996	0.0903	-0.0127	-0.0612	-0.0856	-0.1270	-0.1052	-0.0862	-0.0845	-0.0678	-0.1235	-0.0825	-0.0605
	2.5	0.1151	0.1052	0.0321	-0.0374	-0.0820	-0.1178	-0.0522	-0.0717	-0.0246	-0.0855	-0.0581	-0.0280	-0.0628
	0	0.1365	0.0965	-0.0015	-0.0573	-0.0868	-0.1553	-0.0734	-0.0382	-0.0380	-0.0237	-0.0615	-0.0091	-0.0059
	-2.5	0.1161	0.0967	-0.0064	-0.0555	-0.0599	-0.1914	-0.0487	-0.0749	-0.1117	-0.0013	-0.1250	-0.0066	-0.1327
	-5	0.1555	0.1148	0.0429	-0.0328	-0.0292	-0.0502	-0.0222	-0.0409	0.0040	-0.0347	0.0388	-0.0531	-0.0401
	-7.5	0.1147	0.1519	0.1111	0.0395	0.0267	0.0319	0.0833	0.0016	0.0174	0.0492	0.0549	0.0298	0.0063
	-10	0.1707	0.2318	0.1847	0.0911	0.0837	0.0172	0.1372	0.0567	0.0684	0.0243	0.0631	-0.0255	-0.1847
	-12.5	0.3033	0.2163	0.1857	0.1548	0.1233	0.1623	0.2210	0.1482	0.0960	0.1032	0.0728	-0.0770	-0.1520
	-15	0.0225	-0.0046	-0.0284	-0.0901	-0.0018	-0.0328	0.2227	0.1023	0.1185	0.0705	-0.0139	-0.1093	-0.1209

Table A.13: Average Net Force Magnitude Error (N) - Trial 3

		Version Angle (°)													
		-15	-12.5	-10	-7.5	-5	-2.5	0	2.5	5	7.5	10	12.5	15	
Inclination Angle (°)	15	0.1165	0.0119	-0.0208	-0.0566	-0.0334	-0.0421	-0.1681	-0.1111	-0.1444	-0.1640	-0.1646	-0.2159	-0.2832	
	12.5	0.0732	0.0943	0.0207	-0.0148	-0.0053	-0.0580	-0.0772	-0.0737	-0.0320	-0.0676	-0.1587	-0.1884	-0.1676	
	10	0.1357	0.1300	0.0412	0.0122	0.0116	-0.0403	-0.0528	-0.0174	-0.0221	-0.0478	-0.0947	-0.1527	-0.1249	
	7.5	0.1186	0.1566	0.0844	0.0180	-0.0061	-0.0366	-0.0192	-0.0230	-0.0353	-0.0186	-0.0892	-0.0515	0.0024	
	5	0.1521	0.1924	0.0716	0.0335	0.0072	-0.0217	-0.0498	-0.0062	-0.0536	-0.0222	-0.0127	-0.0050	0.0439	
	2.5	0.1680	0.2229	0.1135	0.0488	-0.0009	0.0207	-0.0265	-0.0042	0.0071	-0.0057	-0.0391	0.0573	0.1176	
	0	0.2181	0.1824	0.0528	0.0119	-0.0250	-0.0482	0.0174	-0.0026	0.0292	0.0364	0.0030	0.0316	0.0243	
	-2.5	0.2169	0.2234	0.1385	0.0498	-0.0287	-0.1072	-0.0245	-0.0517	-0.0620	-0.0614	0.0060	0.0206	0.0194	
	-5	0.1707	0.2202	0.1510	0.1484	0.0922	0.0809	0.1241	0.0537	0.0212	0.0797	0.0129	0.0699	-0.0242	
	-7.5	0.2347	0.2392	0.1870	0.1315	0.0978	0.1463	0.1726	0.0423	0.0934	0.1200	0.1002	0.0543	-0.0136	
	-10	0.3493	0.3309	0.2370	0.2109	0.1833	0.1834	0.2274	0.1532	0.1146	0.1444	0.1061	0.1106	-0.0209	
	-12.5	0.1973	0.4084	0.2402	0.2831	0.2862	0.2307	0.2627	0.1870	0.1611	0.1642	0.0500	0.0645	-0.0371	
	-15	-0.0240	-0.0287	-0.0317	-0.0541	-0.0107	0.0905	0.3116	0.2104	0.2034	0.1522	0.0571	-0.0441	-0.0258	

Table A.14: Net Force Magnitude Error (N) - Trial 4

		Version Angle (°)												
		-15	-12.5	-10	-7.5	-5	-2.5	0	2.5	5	7.5	10	12.5	15
Inclination Angle (°)	15	0.3160	0.2717	0.1997	0.1198	0.0948	-0.0063	-0.0677	-0.0254	-0.0547	-0.1157	-0.1297	-0.0834	-0.2043
	12.5	0.1916	0.1221	0.0846	0.0371	0.0471	-0.0332	-0.0326	-0.0144	-0.0360	-0.0049	-0.0743	-0.0168	-0.0687
	10	0.2479	0.1801	0.1089	0.0931	0.0404	0.0338	-0.0112	0.0330	0.0251	-0.0059	-0.0502	-0.0259	-0.0223
	7.5	0.2568	0.2076	0.1163	0.0536	0.0092	0.0319	-0.0327	0.0342	-0.0172	0.0589	0.0047	0.0943	0.1214
	5	0.2747	0.2326	0.1636	0.1365	0.0743	0.0192	0.0521	0.0494	0.0615	0.0392	0.0721	0.1143	0.1277
	2.5	0.2934	0.2462	0.1728	0.0950	0.0445	0.0379	0.0272	0.0545	0.0544	0.1193	0.1222	0.1907	0.1612
	0	0.3406	0.2620	0.1589	0.1317	0.1170	0.0933	0.1047	0.1715	0.1727	0.1625	0.1566	0.1932	0.1535
	-2.5	0.3061	0.2730	0.1614	0.0924	0.0443	-0.0024	-0.0179	-0.0263	0.0392	0.0828	0.0634	0.1825	0.0595
	-5	0.3036	0.3357	0.1894	0.1876	0.1422	0.1840	0.1407	0.0982	0.1671	0.1070	0.1656	0.1501	0.0045
	-7.5	0.2896	0.3658	0.2595	0.2082	0.1958	0.2160	0.1596	0.1936	0.1819	0.1660	0.2265	0.2106	0.1202
	-10	0.3398	0.3773	0.3108	0.2529	0.1912	0.2388	0.2434	0.2323	0.2922	0.3018	0.3048	0.1659	-0.0205
	-12.5	0.3518	0.4792	0.3476	0.3434	0.3112	0.2834	0.3042	0.2856	0.2775	0.2346	0.2372	0.0841	-0.0287
	-15	0.1455	0.2556	0.1399	0.0584	0.0987	0.2241	0.2983	0.2264	0.2882	0.2014	0.1584	0.0502	0.0142

Table A.15: Net Force Magnitude Error (N) - Trial 5

		Version Angle (°)												
		-15	-12.5	-10	-7.5	-5	-2.5	0	2.5	5	7.5	10	12.5	15
Inclination Angle (°)	15	0.2505	0.2114	0.1432	0.0528	0.0385	-0.0598	-0.0833	0.0089	-0.0128	-0.0792	-0.1389	-0.0951	-0.2430
	12.5	0.1541	0.1136	0.0820	0.0879	0.0558	-0.0046	-0.0361	0.0081	0.0102	0.0039	-0.1400	-0.0679	-0.1456
	10	0.2066	0.1950	0.1198	0.0888	0.0888	-0.0648	-0.0225	0.0658	0.0507	-0.0320	-0.0728	-0.0226	-0.0833
	7.5	0.2213	0.2257	0.1116	0.0691	0.0340	-0.0104	-0.0263	0.0357	0.0346	-0.0136	-0.0133	-0.0055	-0.0090
	5	0.2576	0.2387	0.1542	0.1308	0.0543	0.0101	0.0237	0.0354	0.0927	0.0874	0.0900	0.0455	0.1415
	2.5	0.2981	0.2986	0.1542	0.0951	0.0735	0.0620	0.0545	0.0509	0.0626	0.0175	0.0436	0.1115	0.1263
	0	0.2716	0.2720	0.1675	0.1280	0.0886	0.0708	0.0900	0.1112	0.1234	0.0854	0.1041	0.1288	0.1020
	-2.5	0.2849	0.2954	0.1906	0.1313	0.0890	-0.0190	0.0521	0.0077	0.0211	0.0047	0.1550	0.1428	0.1569
	-5	0.2399	0.3022	0.2375	0.1740	0.1231	0.0831	0.1344	0.0679	0.0927	0.1044	0.1319	0.1533	0.0445
	-7.5	0.3000	0.2928	0.2672	0.2358	0.1854	0.1380	0.2203	0.1472	0.2023	0.2250	0.2090	0.2302	0.0716
	-10	0.3460	0.3950	0.3145	0.2630	0.2528	0.2574	0.2519	0.1869	0.2489	0.1947	0.1590	0.1347	-0.0822
	-12.5	0.4502	0.4076	0.3651	0.3501	0.3210	0.3401	0.3225	0.2083	0.2259	0.1638	0.2211	0.1614	0.1158
	-15	0.0979	0.1781	0.1130	0.0615	0.1335	0.2589	0.3450	0.2338	0.2702	0.2325	0.1085	0.0792	0.0241

Appendix B: Reamer Vector Measurement System Error Data Averaged Over Five Trials for Results Presented in Chapter 2

The following tables are the error results for each measurand and each trail used to determine the system repeatability. The error is determined for each angle of approach bin described in section 2.5. The mean absolute errors were 0.2 ± 0.2 degrees, 0.2 ± 0.2 degrees and 0.4 ± 0.3 N for version angle of approach, inclination angle of approach and net force magnitude, respectively.

Version Angle of Approach Error

Table B.1: Average Version Angle of Approach Error (°) – All Trials

		Version Angle (°)														
		-15	-12.5	-10	-7.5	-5	-2.5	0	2.5	5	7.5	10	12.5	15		
Inclination Angle (°)	15	0.0145	0.0294	0.0682	0.1052	0.1280	0.1436	0.0735	0.0588	0.0306	-0.0040	-0.0472	-0.1300	-0.1517		
	12.5	0.0109	0.0399	0.0672	0.0666	0.0822	0.0552	0.0334	0.0077	-0.0037	-0.0389	-0.0760	-0.1063	-0.0957		
	10	0.0415	0.0306	0.0378	0.0489	0.0532	0.0299	0.0088	-0.0031	-0.0205	-0.0254	-0.0383	-0.0892	-0.0422		
	7.5	0.0546	0.0493	0.0539	0.0436	0.0302	-0.0048	-0.0177	-0.0277	-0.0454	-0.0588	-0.0835	-0.0865	-0.0704		
	5	0.0566	0.0576	0.0329	0.0252	0.0113	-0.0148	-0.0316	-0.0403	-0.0389	-0.0486	-0.0721	-0.0837	-0.0583		
	2.5	0.0475	0.0432	0.0209	0.0035	-0.0026	-0.0434	-0.0438	-0.0480	-0.0473	-0.0393	-0.0515	-0.0796	-0.0304		
	0	0.0022	0.0053	-0.0225	-0.0207	-0.0239	-0.0488	-0.0419	-0.0319	-0.0201	-0.0059	-0.0054	-0.0298	-0.0015		
	-2.5	0.0170	0.0117	-0.0231	-0.0233	-0.0250	-0.0689	-0.0272	-0.0148	-0.0123	-0.0001	0.0053	-0.0096	0.0303		
	-5	-0.0237	-0.0049	-0.0433	-0.0392	-0.0455	-0.0500	-0.0538	-0.0178	-0.0227	-0.0162	-0.0067	-0.0013	0.0295		
	-7.5	-0.0291	-0.0063	-0.0430	-0.0401	-0.0431	-0.0565	-0.0455	-0.0290	0.0011	0.0014	0.0192	0.0007	0.0580		
	-10	-0.0423	-0.0209	-0.0727	-0.0629	-0.0523	-0.0502	-0.0379	0.0002	0.0237	0.0271	0.0393	0.0049	0.0110		
	-12.5	-0.0543	0.0114	-0.0376	-0.0374	-0.0507	-0.0625	-0.0141	0.0352	0.0629	0.0446	0.0306	0.0019	0.0727		
	-15	-0.0555	-0.0672	-0.0989	-0.0628	-0.0180	-0.0329	-0.0418	0.0113	0.0420	0.0710	0.0914	0.0679	0.1051		

Inclination Angle of Approach Error

Table B.2: Average Inclination Angle of Approach Error (°) – All Trials

Inclination Angle (°)	Version Angle (°)														
	-15	-12.5	-10	-7.5	-5	-2.5	0	2.5	5	7.5	10	12.5	15		
15	0.0231	0.0392	0.0440	0.0531	0.0149	0.0035	-0.0082	-0.0087	0.0008	0.0122	0.0009	0.0095	0.0068		
12.5	-0.0760	-0.0528	-0.0498	-0.0267	-0.0498	-0.0443	-0.0119	-0.0104	0.0033	0.0008	0.0085	0.0244	0.0619		
10	-0.0478	-0.0382	-0.0284	-0.0111	-0.0159	-0.0079	0.0294	0.0252	0.0328	0.0539	0.0471	0.0701	0.1165		
7.5	-0.0138	-0.0040	0.0051	0.0128	0.0085	0.0241	0.0519	0.0422	0.0316	0.0566	0.0450	0.0615	0.1290		
5	0.0069	0.0112	0.0255	0.0334	0.0379	0.0519	0.0881	0.0661	0.0725	0.0727	0.0660	0.0661	0.1475		
2.5	0.0337	0.0260	0.0499	0.0499	0.0646	0.0811	0.1175	0.1000	0.0902	0.0997	0.0893	0.0893	0.1537		
0	0.0214	0.0263	0.0466	0.0473	0.0615	0.0731	0.1183	0.0914	0.0857	0.0822	0.0717	0.0650	0.0909		
-2.5	0.0501	0.0260	0.0642	0.0703	0.0763	0.0862	0.1108	0.0962	0.0787	0.0621	0.0738	0.0367	0.1332		
-5	0.0786	0.0335	0.0903	0.0843	0.1062	0.1197	0.1492	0.1115	0.0976	0.0951	0.0846	0.0656	0.1807		
-7.5	0.0921	0.0557	0.1163	0.1110	0.1394	0.1628	0.1956	0.1367	0.1226	0.1242	0.1139	0.0764	0.2345		
-10	0.1301	0.1080	0.1429	0.1510	0.1687	0.1759	0.2428	0.1566	0.1586	0.1452	0.1343	0.0980	0.2345		
-12.5	0.2464	0.2075	0.2257	0.2368	0.2741	0.2749	0.3396	0.2262	0.2120	0.1945	0.1568	0.1685	0.2556		
-15	-0.0148	0.0143	0.0497	0.0867	0.1496	0.2232	0.3741	0.3139	0.3226	0.3144	0.2636	0.2794	0.3516		

Net Force Magnitude Error

Table B.3: Average Net Force Magnitude Error (N) – All Trials

		Version Angle (°)												
		-15	-12.5	-10	-7.5	-5	-2.5	0	2.5	5	7.5	10	12.5	15
Inclination Angle (°)	15	0.1468	0.0890	0.0326	-0.0418	-0.0373	-0.0989	-0.1860	-0.0979	-0.1227	-0.1803	-0.2291	-0.2133	-0.3315
	12.5	0.0343	0.0333	-0.0296	-0.0507	-0.0786	-0.0966	-0.1222	-0.0836	-0.0881	-0.0879	-0.1623	-0.1521	-0.2389
	10	0.1009	0.0881	0.0099	-0.0073	-0.0297	-0.0811	-0.0946	-0.0371	-0.0586	-0.0885	-0.1369	-0.1287	-0.1540
	7.5	0.1218	0.1202	0.0313	-0.0253	-0.0590	-0.0611	-0.0921	-0.0317	-0.0579	-0.0336	-0.0690	-0.0424	-0.0274
	5	0.1521	0.1631	0.0575	0.0274	-0.0239	-0.0564	-0.0585	-0.0245	-0.0252	-0.0284	-0.0327	-0.0141	0.0143
	2.5	0.1838	0.1864	0.0839	0.0201	-0.0166	-0.0291	-0.0388	-0.0127	-0.0013	-0.0098	-0.0031	0.0528	0.0517
	0	0.1880	0.1678	0.0550	0.0142	-0.0171	-0.0529	0.0048	0.0274	0.0346	0.0233	0.0149	0.0499	0.0317
	-2.5	0.2012	0.1991	0.0937	0.0235	-0.0306	-0.0992	-0.0509	-0.0703	-0.0625	-0.0284	-0.0269	0.0514	-0.0375
	-5	0.1621	0.2093	0.1244	0.0845	0.0491	0.0401	0.0755	0.0180	0.0400	0.0417	0.0484	0.0482	-0.0365
	-7.5	0.2024	0.2389	0.1771	0.1234	0.0925	0.1072	0.1459	0.0784	0.1031	0.1046	0.1069	0.0990	0.0041
	-10	0.2641	0.3058	0.2316	0.1768	0.1549	0.1448	0.2052	0.1307	0.1573	0.1399	0.1238	0.0578	-0.1100
	-12.5	0.3297	0.3746	0.2868	0.2741	0.2599	0.2598	0.2783	0.1909	0.1686	0.1456	0.1091	0.0268	-0.0561
	-15	0.0198	0.0794	-0.0044	-0.0280	0.0151	0.1112	0.2848	0.1914	0.2060	0.1442	0.0647	-0.0429	-0.0505

Appendix C: LabVIEW Calibration and Error Compensation VIs

The following figures show the LabVIEW block diagram for the reamer vector measurement system calibration and error compensation VI and the related SubVI block diagrams.

Reamer Vector Measurement System Block Diagrams

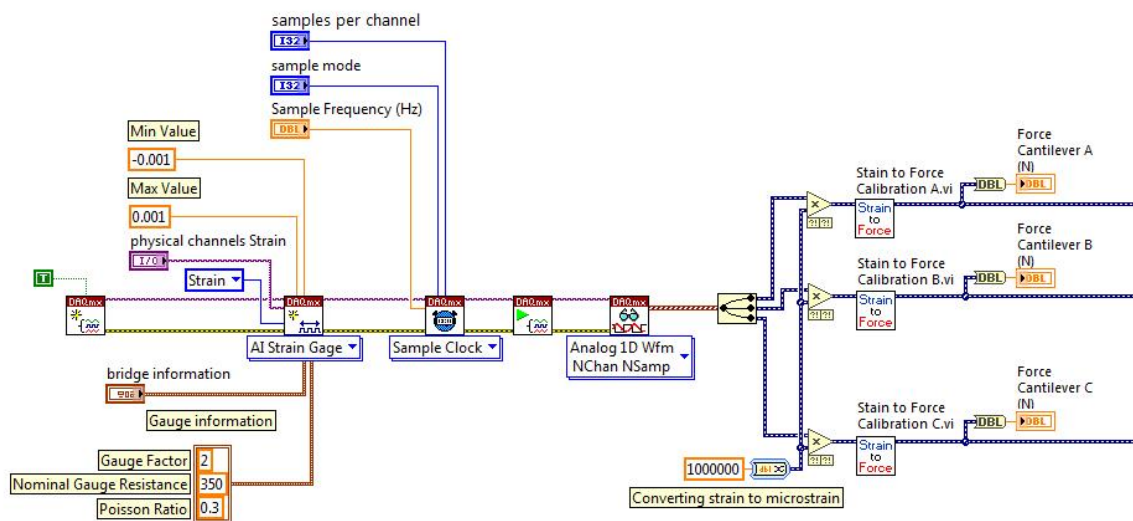


Figure C.1: Data Acquisition Block Diagram

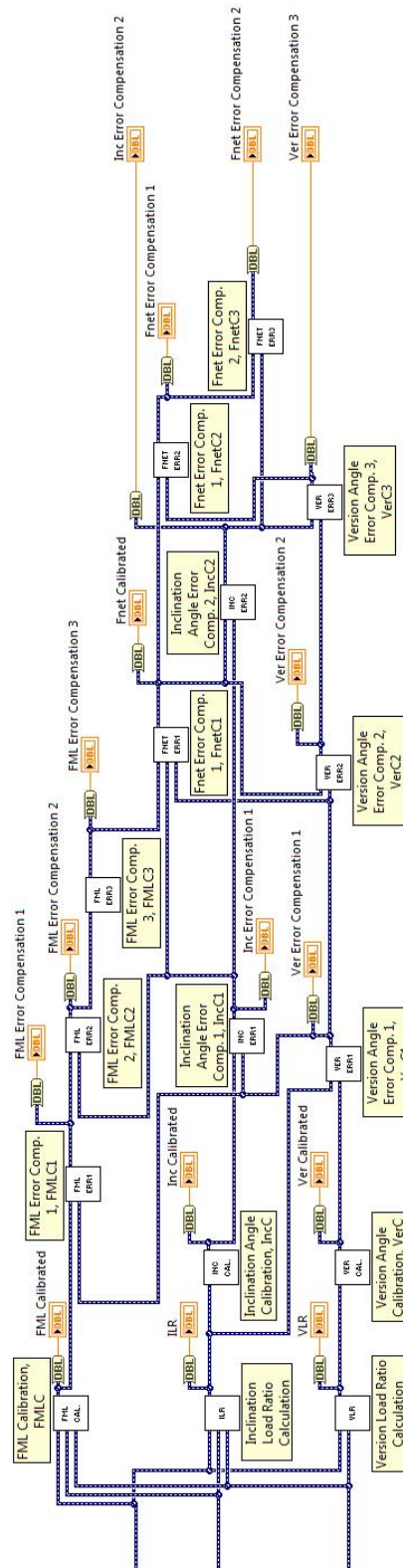


Figure C.2: Calibration and Error Compensation Block Diagram

Cantilever Strain to Force Calibration Block Diagrams

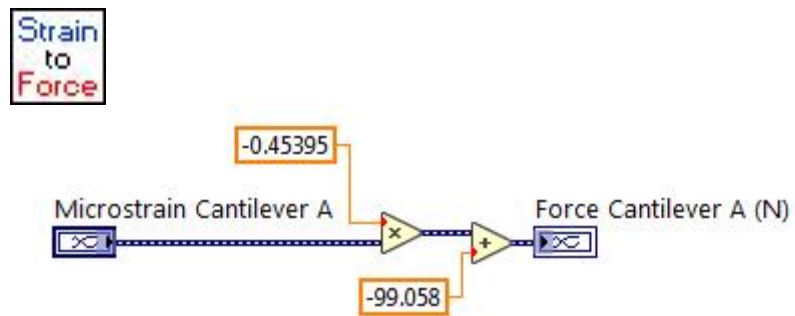


Figure C.3: Cantilever A Calibration Block Diagram

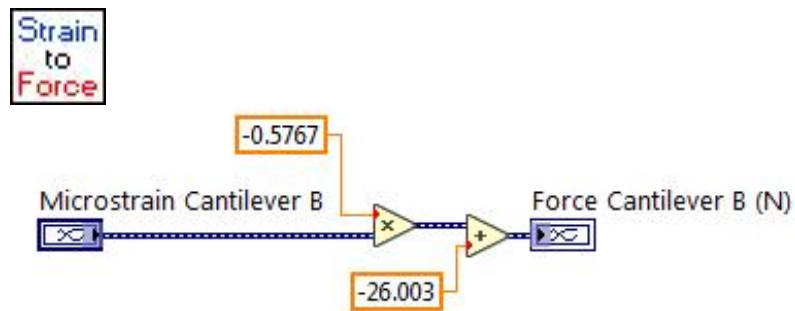


Figure C.4: Cantilever B Calibration Block Diagram

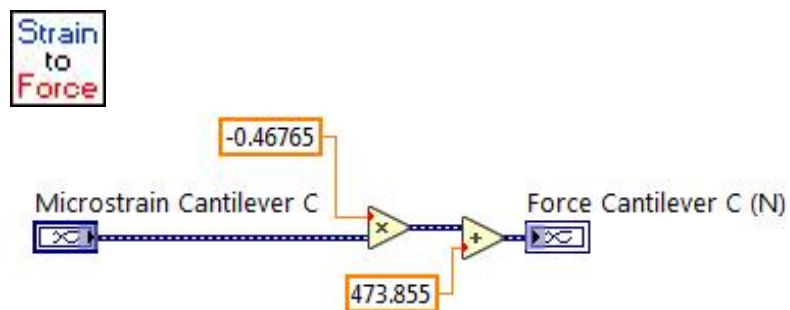


Figure C.5: Cantilever C Calibration Block Diagram

Version Angle of Approach Calibration and Error Compensation Block Diagrams

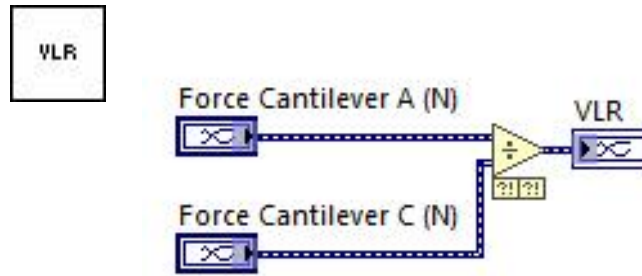


Figure C.6: Version Load Ratio Block Diagram

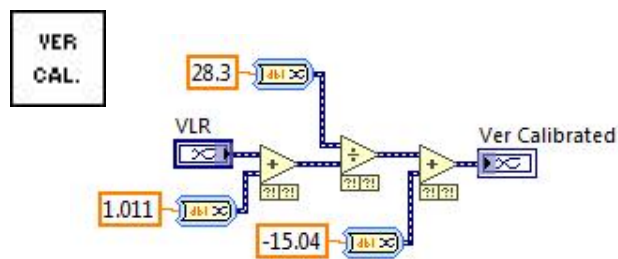


Figure C.7: Version Angle Calibration Block Diagram

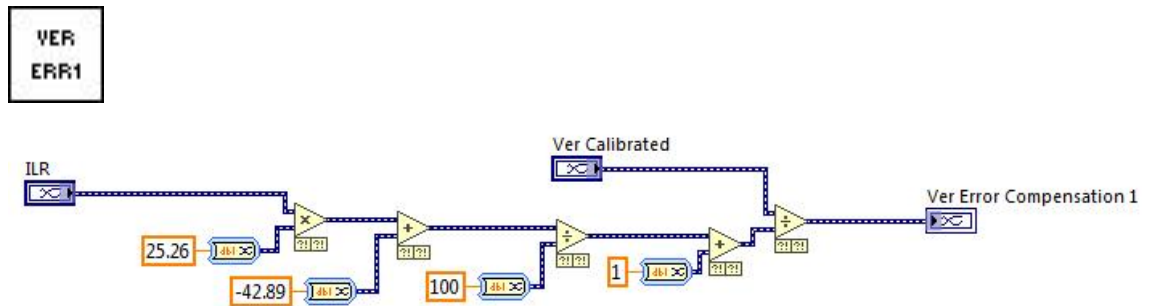


Figure C.8: Version Angle Error Compensation Stage 1 Block Diagram

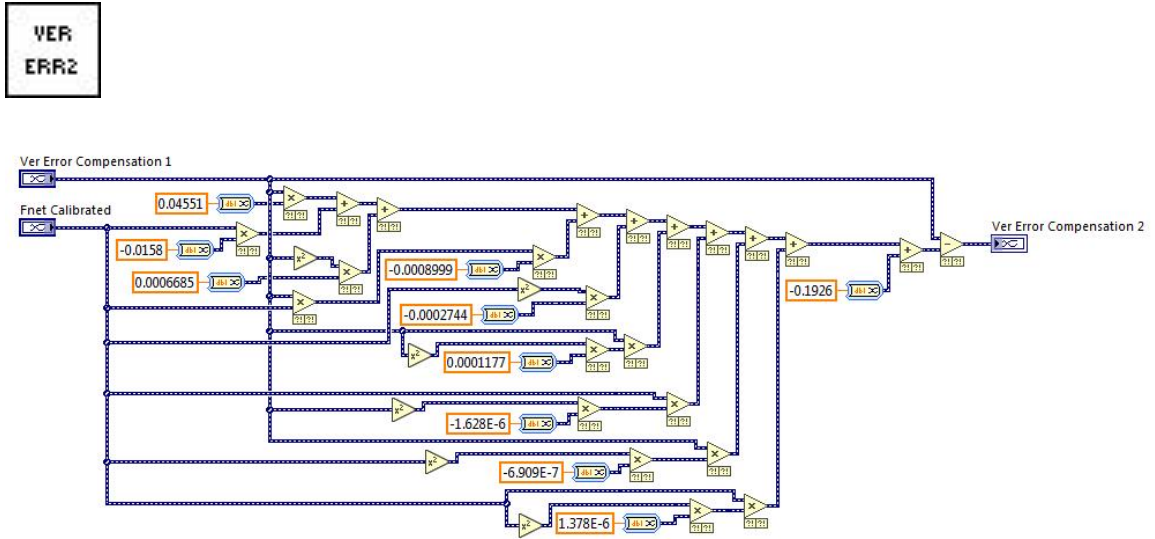


Figure C.9: Version Angle Error Compensation Stage 2 Block Diagram

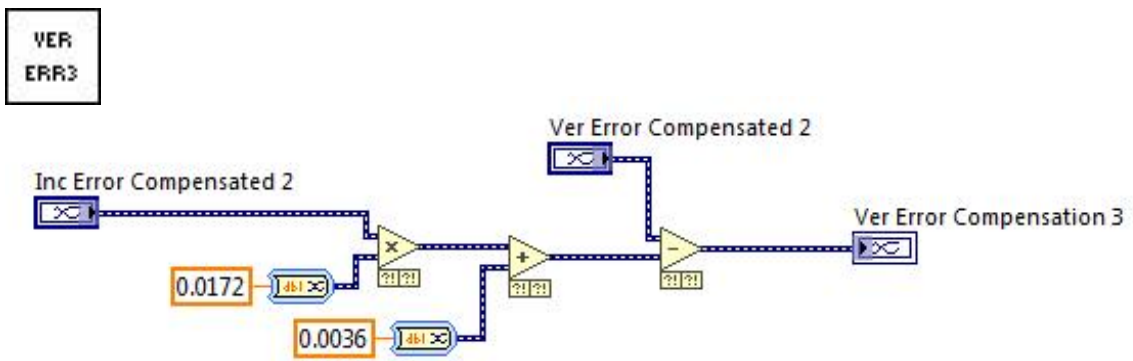


Figure C.10: Version Angle Error Compensation Stage 3 Block Diagram

Inclination Angle of Approach Calibration and Error Compensation Block Diagrams

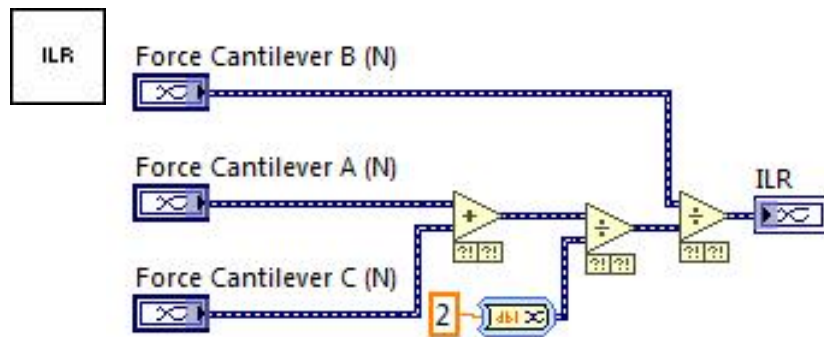


Figure C.11: Inclination Load Ratio Block Diagram

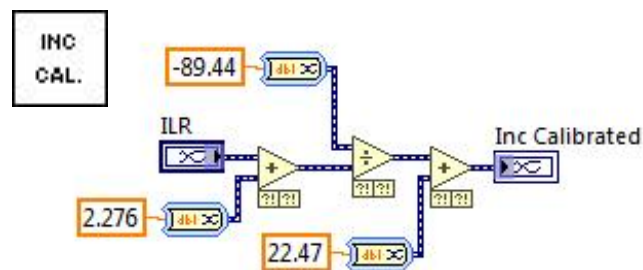


Figure C.12: Inclination Angle Calibration Block Diagram

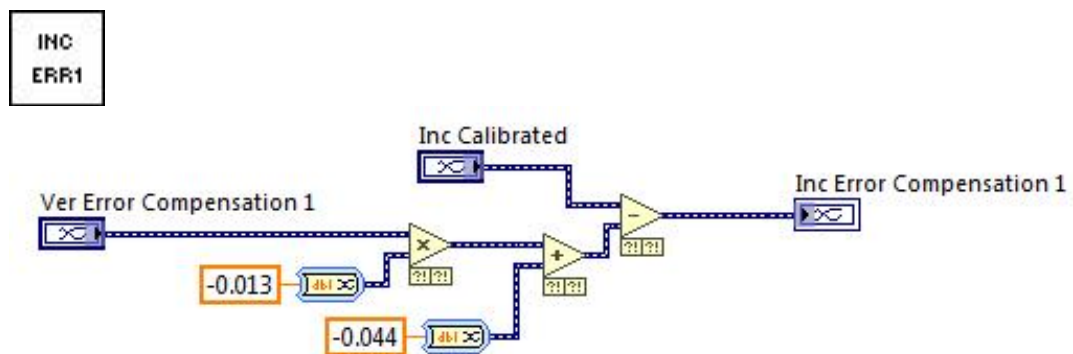


Figure C.13: Inclination Angle Error Compensation Stage 1 Block Diagram

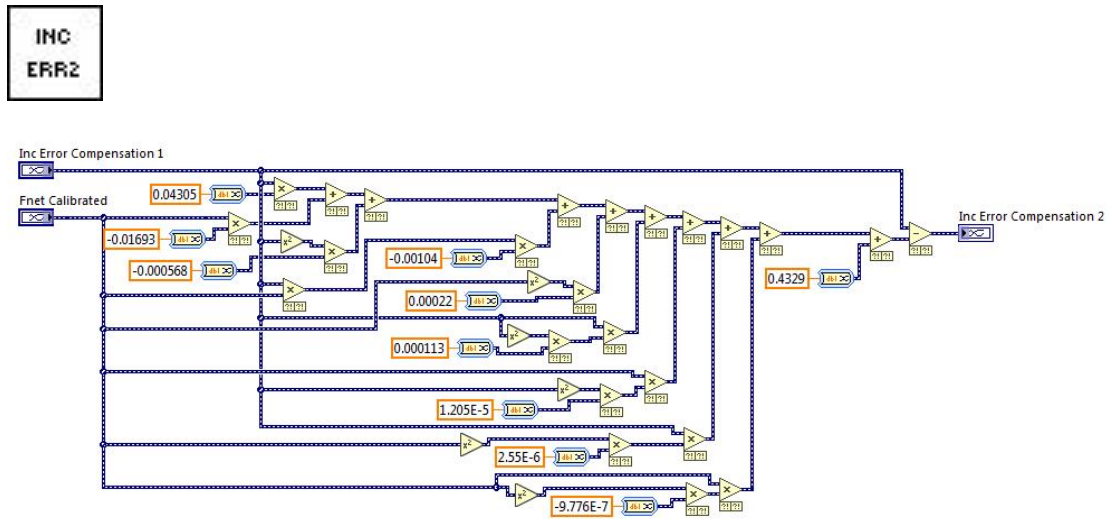


Figure C.14: Inclination Angle Error Compensation Stage 2 Block Diagram

Force Magnitude Acting Along the ML Axis Calibration and Error Compensation Block Diagrams

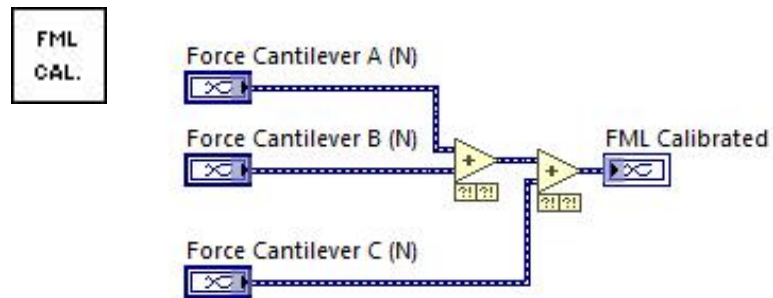


Figure C.15: F_{ML} Calibration Block Diagram

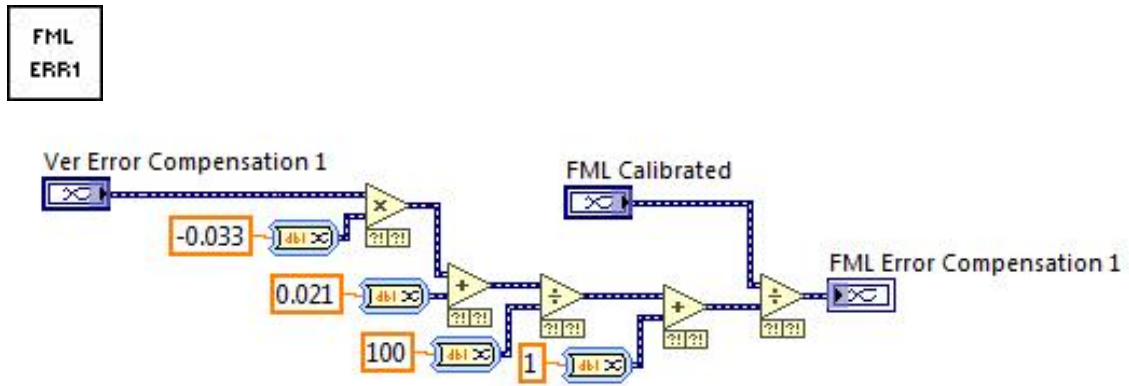


Figure C.16: FML Error Compensation Stage 1 Block Diagram

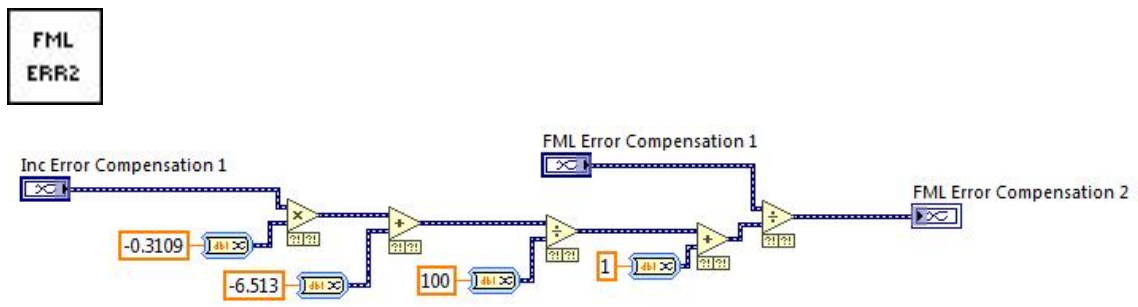


Figure C.17: FML Error Compensation Stage 2 Block Diagram

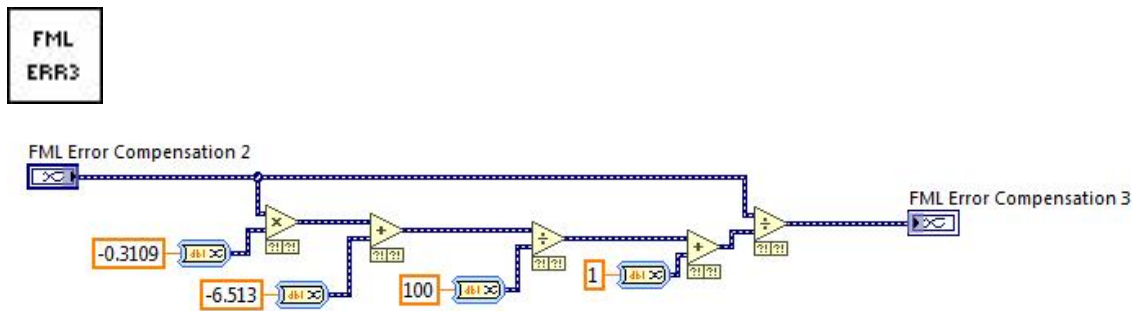


Figure C.18: FML Error Compensation Stage 3 Block Diagram

Net Force Magnitude Calibration and Error Compensation Block Diagrams

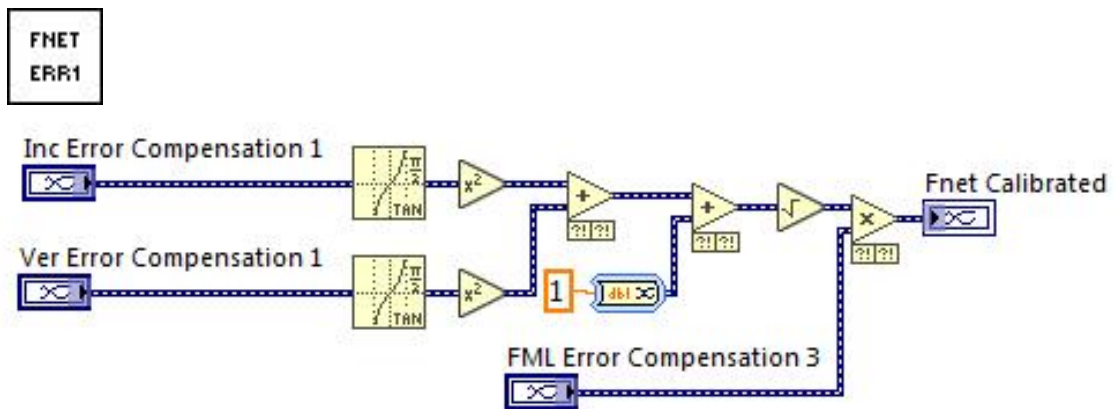


Figure C.19: F_{net} Error Compensation Stage 1 Block Diagram

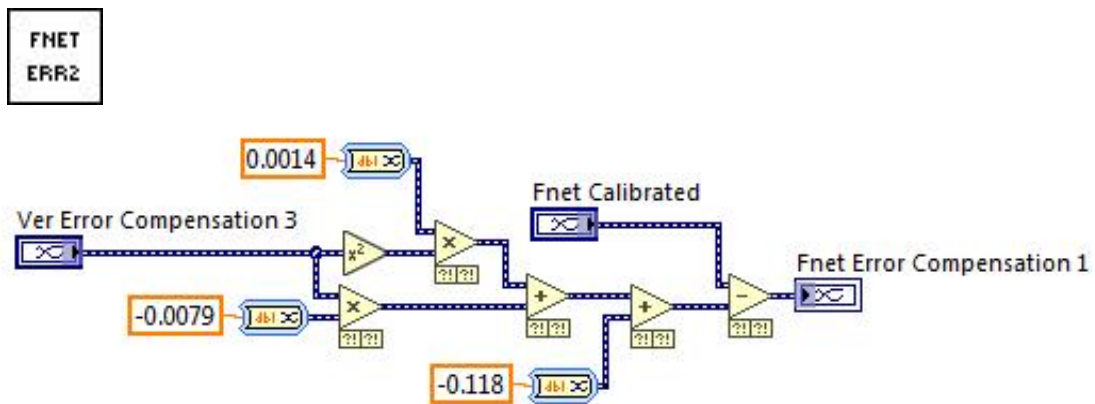


Figure C.20: F_{net} Error Compensation Stage 2 Block Diagram

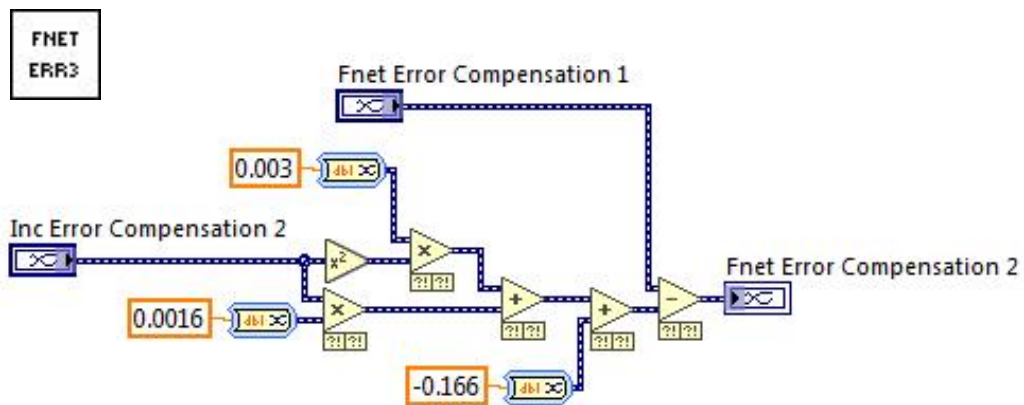


Figure C.21: F_{net} Error Compensation Stage 3 Block Diagram

Appendix D: Simulated CT Generation MATLAB Code

The following MATLAB code was used to generate the simulated CT images:

```
fprintf('Loading DICOM\n');
[I,info,A]=ReadDicomStack('C:\Cadaver CTs\Final Dicoms\Native
(unmodified) DICOMS');
%%
%Importing Mimics mask files for the native and modified scapula and
fprintf('Importing Hounsfield values from Mimics masks\n');
ImportedHounsfieldNative = importdata(...
    'C:\Cadaver CTs\Mask Grey Values\Neutral Version_Hounsfield.txt');
ImportedHounsfieldModified = importdata(...
    'C:\Cadaver CTs\Mask Grey Values\5 Degree
Retroversion_Hounsfield.txt');

%%
%Extracting relevant DICOM metadata and mask information needed to
%modify the DICOM stack
SliceThickness = A(3,3);    %Slice thickness
PixelSpacing = - A(1,2);    %Pixel spacing

Xorigin = A(1,4);          %DICOM origin
Yorigin = A(2,4);
Zorigin = A(3,4);

%Z position of first image slice containing the scapula
FirstSlice = min(ImportedHounsfieldNative(:,3));
%Z position of the last image slice containing the scapula
LastSlice = max(ImportedHounsfieldNative(:,3));
%Number of image slices containing the scapula
NumberOfScapSlices = (LastSlice - FirstSlice)/SliceThickness + 1;
%slice number of first slice containing the scapula
FirstSliceScap = uint16((ImportedHounsfieldModified(1,3) - Zorigin)/...
    SliceThickness + 1) + 1;

%Number of voxels in the native scapula mask
HounsfieldSizeNative = size(ImportedHounsfieldNative,1);
%Number of voxels in the modified scapula mask
HounsfieldSizeModified = size(ImportedHounsfieldModified,1);

%%
%Initializing image arrays for the image manipulation
fprintf('Initializing Scapula Image Arrays\n');
%initialize 3D array for native scapula images
OriginalScap(512,512,NumberOfScapSlices) = 0;
%initialize 3D array for binary native scapula mask images
OriginalScapBinary(512,512,NumberOfScapSlices) = 0;
%initialize 3D array for modified scapula images
ModifiedScap(512,512,NumberOfScapSlices) = 0;
%initialize 3D array for binary modified scapula mask images
ModifiedScapBinary(512,512,NumberOfScapSlices) = 0;
```

```

%%
%Organize native scapula Hounsfield units from the native mask into 2D
%slices in the CT coordinate system
fprintf('Organizing Native Hounsfield units into 2D slices\n');
i = 1;
while i <= HounsfieldSizeNative
    X = uint16(512 - (ImportedHounsfieldNative(i,1) - ...
        (Xorigin - 512*PixelSpacing))/PixelSpacing + 1);
    Y = uint16(512 - (ImportedHounsfieldNative(i,2) - ...
        (Yorigin - 512*PixelSpacing))/PixelSpacing + 1);
    Z = uint16((ImportedHounsfieldNative(i,3) - Zorigin)/...
        SliceThickness + 1);

    OriginalScapBinary(Y,X,Z - uint16((ImportedHounsfieldNative...
        (1,3) - Zorigin))) = 1000;
    i = i+1;
end
%Organize Modified Hounsfield units into 2D slices in the CT coordinate
%system

%%
%Organize modified scapula Hounsfield units from the native mask into
%2D slices in the CT coordinate system
fprintf('Organizing Modified Hounsfield units into 2D slices\n');
i = 1;
while i <= HounsfieldSizeModified
    X = uint16(512 - (ImportedHounsfieldModified(i,1) - ...
        (Xorigin - 512*PixelSpacing))/PixelSpacing + 1);
    Y = uint16(512 - (ImportedHounsfieldModified(i,2) - ...
        (Yorigin - 512*PixelSpacing))/PixelSpacing + 1);
    Z = uint16((ImportedHounsfieldModified(i,3) - Zorigin)/...
        SliceThickness + 1);

    ModifiedScap(Y,X,Z - uint16((ImportedHounsfieldModified(1,3) - ...
        Zorigin)/SliceThickness + 1) + 1) = 2000;
    i = i+1;
end

%%
%Defining structuring element for eroding and dilating functions
se = strel('line',6,130);
se2 = strel('sphere',4);
se3 = strel('sphere',2);

```

```

%%
%Constructing cortical shell and trabecular bone for modified scapula
%geometry
i = 1;
fprintf('Constructing Cortical Shell and Trabecular Bone\n');
while i < NumberofScapSlices

    %Constructing cortical shell
    erodedModified = imerode(ModifiedScap(:,:,i),se3);
    erodedModified2 = imerode(erodedModified,se);
    Modified = ModifiedScap(:,:,i) - erodedModified;
    Modified2 = (erodedModified - erodedModified2);
    Cortical = Modified + rand(512,512).*...
        (erodedModified.*(1/(max(max(I(:,:,Z))) ...
        - 200))).*100;

    %Extracting cancellous bone from original image
    Cancellous = I(:,:,FirstSliceScap + i-...
        1).*(erodedModified.*(1/2000));

    %Removing the original scapula and inserting the modified
    %scapula into the original image
    I(:,:,FirstSliceScap + i - 2) = I(:,:,FirstSliceScap +...
        i - 2).*imcomplement(imdilate(ModifiedScap(:,:,i).* ...
        (1/2000),se2)) + imdilate(ModifiedScap(:,:,i).* ...
        (1/2000),se2).*(1000 + rand(512,512)*100).* ...
        imcomplement(ModifiedScap(:,:,i).(1/2000))+ ...
        imgaussfilt(Cancellous.*1.25 + Cortical + ...
        Modified,1).*ModifiedScap(:,:,i).(1/2000).*0.75;

    imshow(I(:,:,FirstSliceScap + i-2),[]);

    i = i + 1;
end

```

```

%%
%Writing the DICOM images with metadata from the original image
i = 1;
while i <= size(I,3)

    %scaling 12-bit scanner Hounsfield unit range down to 0-1 range
    I(:,:,i) = (I(:,:,i)./(64511+1023));

    imshow(I(:,:,i),[]);

    %Constructing the file name
    filenumbertemp = num2str(i-1);

    if length(filenumbertemp) == 1
        filenumber = strcat('000',filenumbertemp);
    elseif length(filenumbertemp) == 2
        filenumber = strcat('00',filenumbertemp);
    elseif length(filenumbertemp) == 3
        filenumber = strcat('0',filenumbertemp) ;
    else
        filenumber = strcat(filenumbertemp);
    end

    %filename for original image
    filenameretrieve = strcat(...
        'C:\Cadaver CTs\Final Dicoms\Native (unmodified)
DICOMS\0912052L_',filenumber, '.dcm');
    %file name for modified image
    filenameewrite = strcat(...
        'C:\Cadaver CTs\Final Dicoms\Native (modified)
DICOMS\AAAA_',filenumber, '.dcm');
    %reading metadata from original image
    metadata = dicominfo(filenameretrieve);
    %saving modified image with original image metadata
    dicomwrite(I(:,:,i),filenameewrite,metadata);
    i = i + 1;
end

```

Appendix E: KUKA Light Weight Robot Force-Control Repeatability Data Presented in Chapter 3

The following tables are the measurements from the reamer vector measurement system, the ATI Nano25 load cell and Optotrak Certus for the repeatability protocol described in section 3.3.

Version Angle of Approach Measurements

Table E.1: Version Angle of Approach Measurements from Optotrak Certus for Repeatability Analysis

Projected Angle, θ	Net Angle, γ	Trial 1	Trial 2	Trial 3	Trial 4	Trial 5
0	0	8.76	0.69	0.70	0.70	0.70
0	4	4.71	4.71	4.72	4.74	4.73
0	8	8.76	8.77	8.78	8.79	8.80
0	12	13.12	13.16	13.16	13.17	13.18
45	4	3.42	3.44	3.44	3.44	3.44
45	8	6.25	6.26	6.27	6.28	6.28
45	12	9.29	9.33	9.33	9.33	9.34
90	4	0.27	0.27	0.27	0.26	0.27
90	8	0.48	0.48	0.49	0.49	0.48
90	12	0.50	0.51	0.52	0.52	-2.40
135	4	-2.41	-2.42	-2.42	-2.42	-5.19
135	8	-5.17	-5.17	-5.17	-5.17	-8.19
135	12	-8.19	-8.18	-8.18	-8.18	-8.18
180	4	-3.68	-3.69	-3.70	-3.71	-3.71
180	8	-7.76	-7.77	-7.77	-7.77	-7.76
180	12	-12.08	-12.10	-12.12	-12.12	-12.11
225	4	-2.45	-2.46	-2.46	-2.45	-2.46
225	8	-5.27	-5.28	-5.28	-5.28	-5.29
225	12	-8.28	-8.28	-8.28	-8.29	-8.31
270	4	0.64	0.65	0.65	0.65	0.66
270	8	0.60	0.61	0.60	0.61	0.61
270	12	0.45	0.46	0.46	0.46	0.46
315	4	3.45	3.46	3.43	3.44	3.44
315	8	6.25	6.26	6.28	6.29	6.30
315	12	9.31	9.33	9.33	9.34	9.34

Table E.2: Version Angle of Approach Measurements from the ATI Nano25 Load Cell for Repeatability Analysis

Projected Angle, θ	Net Angle, γ	Trial 1	Trial 2	Trial 3	Trial 4	Trial 5
0	0	1.34	1.34	1.34	1.27	1.25
0	4	5.60	5.57	5.54	5.66	5.64
0	8	8.98	8.99	9.01	9.02	9.09
0	12	13.71	13.68	13.71	13.71	13.70
45	4	4.30	4.22	4.22	4.23	4.21
45	8	6.69	6.66	6.63	6.69	6.67
45	12	10.16	10.13	10.14	10.11	10.06
90	4	1.14	1.25	1.22	1.20	1.25
90	8	0.97	0.93	0.97	0.97	0.95
90	12	1.58	1.59	1.57	1.61	-1.40
135	4	-1.41	-1.38	-1.42	-1.36	-5.11
135	8	-5.18	-5.17	-5.16	-5.13	-7.97
135	12	-8.04	-8.08	-7.95	-8.13	-8.07
180	4	-2.75	-2.86	-2.93	-2.99	-2.99
180	8	-6.59	-6.59	-6.60	-6.65	-6.66
180	12	-10.77	-11.29	-11.31	-11.34	-11.30
225	4	-2.00	-2.15	-2.14	-2.14	-2.19
225	8	-4.72	-4.68	-4.74	-4.73	-4.75
225	12	-8.46	-8.37	-8.35	-8.38	-8.43
270	4	1.40	1.34	1.35	1.33	1.34
270	8	1.30	1.34	1.32	1.29	1.32
270	12	0.67	0.69	0.76	0.73	0.73
315	4	4.07	4.15	4.19	4.21	4.12
315	8	6.83	6.82	6.93	6.90	6.86
315	12	9.61	9.63	9.60	9.59	9.60

Table E.3: Version Angle of Approach Measurements from the Reamer Vector Measurement System for Repeatability Analysis

Projected Angle, θ	Net Angle, γ	Trial 1	Trial 2	Trial 3	Trial 4	Trial 5
0	0	1.43	1.45	1.43	1.38	1.36
0	4	5.74	5.76	5.74	5.85	5.81
0	8	9.15	9.13	9.22	9.17	9.23
0	12	13.58	13.52	13.52	13.54	13.52
45	4	4.48	4.44	4.46	4.48	4.45
45	8	6.93	6.91	6.90	6.93	6.95
45	12	10.30	10.25	10.28	10.22	10.17
90	4	1.30	1.45	1.41	1.40	1.46
90	8	1.26	1.29	1.30	1.27	1.27
90	12	2.00	2.01	1.99	2.04	-1.17
135	4	-1.20	-1.13	-1.15	-1.10	-4.83
135	8	-4.93	-4.89	-4.89	-4.87	-7.68
135	12	-7.70	-7.74	-7.60	-7.79	-7.73
180	4	-2.71	-2.80	-2.85	-2.93	-2.92
180	8	-6.62	-6.56	-6.59	-6.62	-6.63
180	12	-10.57	-11.08	-11.13	-11.15	-11.10
225	4	-2.00	-2.11	-2.11	-2.14	-2.16
225	8	-4.76	-4.68	-4.75	-4.74	-4.71
225	12	-8.55	-8.46	-8.40	-8.47	-8.48
270	4	1.41	1.35	1.38	1.36	1.33
270	8	1.28	1.34	1.29	1.29	1.30
270	12	0.49	0.56	0.62	0.60	0.61
315	4	4.25	4.31	4.28	4.30	4.24
315	8	6.92	6.91	7.00	6.95	6.90
315	12	9.47	9.49	9.44	9.43	9.43

Inclination Angle of Approach Measurements

Table E.4: Inclination Angle of Approach Measurements from Optotrak Certus for Repeatability Analysis

Projected Angle, θ	Net Angle, γ	Trial 1	Trial 2	Trial 3	Trial 4	Trial 5
0	0	-0.12	-0.10	-0.10	-0.09	-0.09
0	4	-0.15	-0.15	-0.16	-0.16	-0.16
0	8	-0.06	-0.05	-0.05	-0.05	-0.05
0	12	-0.04	-0.02	-0.02	-0.03	-0.02
45	4	3.02	3.04	3.03	3.04	3.04
45	8	6.03	6.06	6.06	6.07	6.07
45	12	9.01	9.03	9.04	9.05	9.06
90	4	4.29	4.31	4.31	4.32	4.33
90	8	8.57	8.57	8.58	8.58	8.58
90	12	12.77	12.78	12.80	12.80	3.09
135	4	3.09	3.09	3.09	3.10	6.00
135	8	6.01	6.00	6.02	6.02	8.94
135	12	8.95	8.97	8.99	8.97	8.98
180	4	-0.01	0.00	0.00	-0.01	-0.02
180	8	0.07	0.08	0.09	0.08	0.08
180	12	0.00	0.01	0.01	0.01	0.01
225	4	-3.06	-3.05	-3.05	-3.05	-3.05
225	8	-5.96	-5.96	-5.96	-5.96	-5.96
225	12	-9.12	-9.12	-9.12	-9.11	-9.12
270	4	-4.38	-4.38	-4.37	-4.37	-4.38
270	8	-8.72	-8.72	-8.73	-8.73	-8.74
270	12	-13.07	-13.07	-13.07	-13.08	-13.08
315	4	-3.13	-3.13	-3.12	-3.12	-3.12
315	8	-6.19	-6.20	-6.19	-6.20	-6.21
315	12	-9.09	-9.10	-9.11	-9.11	-9.10

Table E.5: Inclination Angle of Approach Measurements from the ATI Nano25 Load Cell for Repeatability Analysis

Projected Angle, θ	Net Angle, γ	Trial 1	Trial 2	Trial 3	Trial 4	Trial 5
0	0	4.85	4.94	4.96	4.97	4.96
0	4	4.58	4.85	4.98	4.80	4.82
0	8	4.08	4.12	4.10	4.11	4.10
0	12	4.61	4.87	4.86	4.94	4.91
45	4	7.82	7.86	7.94	7.98	8.06
45	8	10.31	10.73	10.70	10.76	10.83
45	12	13.57	13.80	13.84	13.88	13.87
90	4	8.96	9.17	9.16	9.24	9.24
90	8	13.23	13.24	13.27	13.24	13.26
90	12	17.19	17.28	17.31	17.12	7.22
135	4	7.30	7.40	7.43	7.38	10.33
135	8	10.44	10.33	10.33	10.39	13.21
135	12	13.43	13.48	13.44	13.51	13.52
180	4	4.66	4.82	4.89	4.89	4.88
180	8	4.47	4.58	4.56	4.58	4.58
180	12	4.66	4.76	4.75	4.82	4.81
225	4	1.64	1.75	1.78	1.77	1.80
225	8	-1.00	-0.88	-0.91	-0.89	-0.87
225	12	-3.58	-3.42	-3.31	-3.39	-3.33
270	4	0.26	0.32	0.38	0.33	0.27
270	8	-3.69	-3.62	-3.66	-3.58	-3.54
270	12	-7.60	-7.32	-7.25	-7.29	-7.27
315	4	1.14	1.17	1.20	1.20	1.16
315	8	-1.54	-1.48	-1.36	-1.48	-1.55
315	12	-4.21	-4.15	-4.11	-4.09	-4.02

Table E.6: Inclination Angle of Approach Measurements from the Reamer Vector Measurement System for Repeatability Analysis

Projected Angle, θ	Net Angle, γ	Trial 1	Trial 2	Trial 3	Trial 4	Trial 5
0	0	4.70	4.77	4.78	4.82	4.79
0	4	4.48	4.70	4.73	4.54	4.58
0	8	3.86	3.91	3.87	3.89	3.88
0	12	4.46	4.69	4.68	4.70	4.75
45	4	7.64	7.63	7.72	7.73	7.78
45	8	10.00	10.43	10.38	10.45	10.51
45	12	12.99	13.20	13.24	13.28	13.27
90	4	8.71	8.88	8.87	8.93	8.93
90	8	12.78	12.79	12.82	12.79	12.79
90	12	16.32	16.45	16.46	16.27	7.04
135	4	7.07	7.15	7.20	7.13	9.92
135	8	10.04	9.92	9.89	9.99	12.66
135	12	12.82	12.86	12.85	12.89	12.91
180	4	4.45	4.61	4.67	4.65	4.65
180	8	4.23	4.28	4.26	4.31	4.28
180	12	4.36	4.46	4.45	4.53	4.51
225	4	1.40	1.52	1.53	1.54	1.56
225	8	-1.18	-1.00	-1.03	-1.00	-1.00
225	12	-3.73	-3.57	-3.49	-3.54	-3.50
270	4	0.12	0.14	0.19	0.14	0.12
270	8	-3.91	-3.87	-3.92	-3.85	-3.78
270	12	-7.82	-7.55	-7.50	-7.54	-7.52
315	4	1.03	1.05	1.09	1.08	1.03
315	8	-1.78	-1.70	-1.60	-1.71	-1.78
315	12	-4.14	-4.08	-3.99	-3.97	-3.90

Net Force Magnitude Measurements

Table E.7: Net Force Magnitude Measurements from the ATI Nano25 Load Cell for Repeatability Analysis

Projected Angle, θ	Net Angle, γ	Trial 1	Trial 2	Trial 3	Trial 4	Trial 5
0	0	52.29	51.75	52.45	52.53	52.69
0	4	51.84	52.03	52.06	52.53	51.90
0	8	50.80	50.98	51.00	50.97	50.92
0	12	51.28	51.90	51.67	51.80	51.72
45	4	51.36	52.01	51.57	51.57	51.49
45	8	51.13	51.30	51.49	51.45	51.46
45	12	51.02	51.55	51.60	51.68	51.75
90	4	51.07	51.90	51.97	51.96	51.81
90	8	51.77	51.29	51.37	51.33	51.29
90	12	52.14	52.41	52.09	52.32	52.45
135	4	52.44	52.52	52.38	52.76	51.99
135	8	52.50	52.71	53.00	52.57	52.16
135	12	52.79	52.79	53.49	52.73	53.02
180	4	52.84	53.23	53.06	52.63	52.43
180	8	52.61	53.28	53.09	53.09	53.00
180	12	53.56	53.44	53.38	53.32	53.26
225	4	52.04	52.21	52.18	52.10	52.09
225	8	52.77	53.00	52.88	53.02	52.93
225	12	51.19	51.31	51.47	51.05	51.44
270	4	51.22	51.23	51.50	51.26	51.47
270	8	50.60	50.57	50.48	50.54	50.72
270	12	48.91	49.03	49.03	49.06	48.91
315	4	50.98	51.16	51.25	51.14	51.05
315	8	50.90	51.02	51.09	51.15	51.49
315	12	50.64	50.80	50.78	50.85	50.90

Table E.8: Net Force Magnitude Measurements from the Reamer Vector Measurement System for Repeatability Analysis

Projected Angle, θ	Net Angle, γ	Trial 1	Trial 2	Trial 3	Trial 4	Trial 5
0	0	51.83	51.31	52.06	52.15	52.26
0	4	51.56	51.73	51.76	52.25	51.60
0	8	50.60	50.80	50.76	50.76	50.69
0	12	51.12	51.78	51.48	51.64	51.55
45	4	51.16	51.81	51.30	51.36	51.22
45	8	51.02	51.23	51.39	51.43	51.32
45	12	51.08	51.67	51.63	51.73	51.77
90	4	50.82	51.69	51.75	51.79	51.57
90	8	51.82	51.19	51.30	51.28	51.25
90	12	52.36	52.56	52.29	52.52	52.13
135	4	52.15	52.21	52.16	52.50	51.74
135	8	52.22	52.51	52.84	52.37	51.99
135	12	52.71	52.67	53.38	52.59	52.87
180	4	52.44	52.92	52.72	52.31	52.10
180	8	52.18	52.81	52.70	52.66	52.62
180	12	53.14	53.03	52.89	52.88	52.82
225	4	51.57	51.71	51.74	51.68	51.63
225	8	52.23	52.45	52.39	52.46	52.35
225	12	50.60	50.73	50.94	50.52	50.90
270	4	50.77	50.83	51.02	50.81	51.08
270	8	50.22	50.16	50.03	50.18	50.43
270	12	48.46	48.64	48.62	48.70	48.56
315	4	50.68	50.72	50.96	50.86	50.67
315	8	50.55	50.75	50.86	50.90	51.20
315	12	50.23	50.50	50.60	50.61	50.64

Appendix F: Custom Load Cell Mount Critical Dimensions

Dimensions are in millimeters

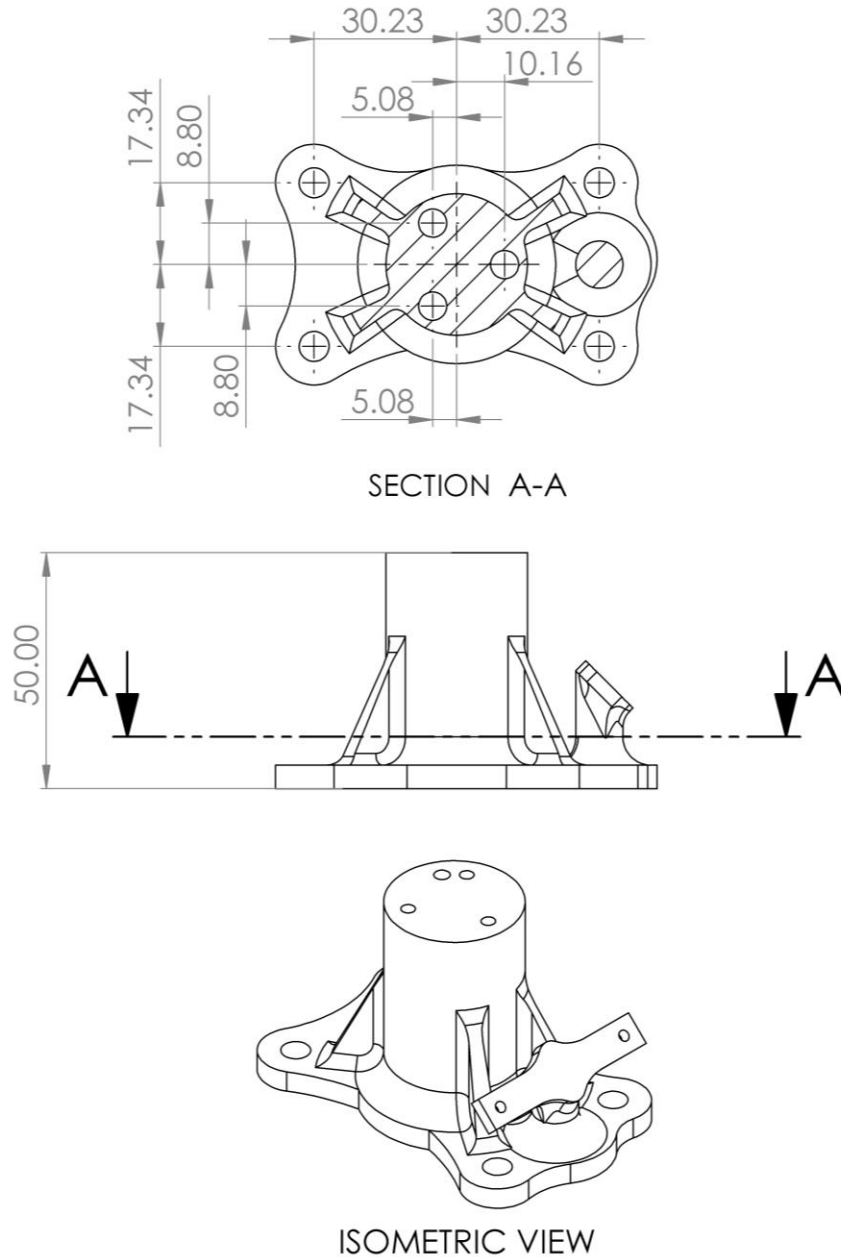


Figure F.1: Custom Load Cell Mount Critical Dimensions

Curriculum Vitae

Name:	David Axford
Post-secondary Education and Degrees:	The University of Western Ontario London, Ontario, Canada 2013-2017 BESc.
	The University of Western Ontario London, Ontario, Canada Candidate for MESC. (Expected 2019)
Honours and Awards:	Continuing Admission Scholarship, The University of Western Ontario, 2013-2016
	Dean's Honour List The University of Western Ontario, 2014-2017
	CAMBR AMBI Undergraduate Research Award The University of Western Ontario, 2015
	NSERC Undergraduate Student Research Award The University of Western Ontario, 2016
	John E. K. Foreman Gold Medal in Mechanical and Materials Engineering The University of Western Ontario, 2017
	NSERC Canadian Graduat Scholarship – Master's Program The University of Western Ontario, 2017-2018
	Ontario Graduate Scholarship The University of Western Ontario, 2018-2019
Related Work Experience	Teaching Assistant The University of Western Ontario 2017-2019
	Research Engineer The University of Western Ontario 2017-2019

Publications:

Papers Accepted to Refereed Journals

1. Badre A, **Axford DT**, Banayan S, Johnson JA, King GJW. (accepted). Role of Anconeus in the Stability of a Lateral Ligament and Common Extensor Origin Deficient Elbow: An In Vitro Biomechanical Study.

Proceedings of Refereed Conferences

1. Badre A, **Axford DT**, Banayan S, Johnson JA, King GJW. (accepted). The Effect of Torsional Moment of Forearm Weight on the Posterolateral Rotatory Instability of a Lateral Collateral Ligament Deficient Elbow. A Novel Biomechanical Modeling and In Vitro Investigation. 14th IFSSH & 11th IFSHT Triennial Congress, Berlin, Germany. (2019, podium)
2. Badre A, **Axford DT**, Banayan S, Johnson JA, King GJW. (accepted). Role of Anconeus in the Stability of a Lateral Ligament Deficient Elbow: An In Vitro Biomechanical Study. 14th IFSSH & 11th IFSHT Triennial Congress, Berlin, Germany. (2019, podium)
3. Badre A, Banayan S, **Axford DT**, Johnson JA, King GJW. (accepted). Role of an Adjustable Hinged Elbow Orthosis in the Rehabilitation of a Lateral Collateral Ligament Deficient Elbow: An In Vitro Biomechanical Study. 14th IFSSH & 11th IFSHT Triennial Congress, Berlin, Germany. (2019, podium)
4. **Axford DT**, Banayan S, Johnson JA, Badre A, King GJW. (accepted). Role of an Adjustable Hinged Elbow Orthosis in the Rehabilitation of a Lateral Collateral Ligament Deficient Elbow: An In Vitro Biomechanical Study. Ontario Biomechanics Conference, Allison, Canada. (2019, poster).
5. **Axford D**, Kusins, J, LeBel, M.-E, Ferreira, L. (2018). Development of a 3D glenoid force reaming simulator for haptic training. Canadian Orthopaedic Research Society Meeting, Victoria, BC, Canada. (2018, poster)
6. Wood, K, **Axford D**, Danby S, Strezlow J, Ferreira L, LeBel M.-E. (2017). Vibration Feedback in Simulation-based Shoulder Surgical Training. Canadian Orthopaedic Association Meeting, Ottawa, ON, Canada. (2017, poster)